

A PETROPHYSICAL EVALUATION OF CAPILLARY PRESSURE FOR A
NATURALLY FRACTURED TIGHT GAS SANDSTONE
RESERVOIR: A CASE STUDY

by

Livia J. Sivila

A thesis submitted to the Faculty and Board of Trustees of the Colorado School of Mines
in partial fulfillment of the requirements for the degree of Master of Science (Petroleum
Engineering).

Golden, Colorado

Date _____

Signed: _____
Livia J. Sivila

Signed: _____
Dr. Ramona M. Graves
Thesis Advisor

Signed: _____
Dr. Roberto Aguilera
Thesis Advisor

Golden, Colorado

Date _____

Signed: _____
Dr. Will Fleckenstein
Professor and Head
Department of Petroleum Engineering

ABSTRACT

The evaluation of capillary pressure is critical to assess and model fluid flow through porous media. The main objective of this research is to improve the understanding of capillary pressure for Field M. The field of study is a quartzitic sandstone gas condensate naturally fractured reservoir located in Bolivia. The particularity of Field M is that the pore space is composed of micro to macro scale fractures from, where the matrix porosity is mainly composed of microfractures.

Capillary pressure is a fluid-rock property that depends on interfacial tension, contact angle between fluid and solids and capillary pore throat radius. A literature review of the theory and models/correlations to estimate capillary pressure indicate that the predominant parameter to determine capillary pressure profiles is the pore throat radius. Following this theory, capillary pressure is evaluated using pore scale simulation and petrophysical evaluation at the log scale while studying the pore throat radius variation.

To investigate the validity of core capillary pressure profiles, pore scale simulation from a modified Berea sandstone network of pores and throats to resemble Field M rock conditions is used. The results from simulation show that the main property affecting capillary pressure profiles, as pointed out from literature review, is the pore throat size distribution. Comparing simulated and experimental capillary pressure curves resulted in different permeability values.

The helium core permeability compared to the permeability values from simulation is always lower. Further inspection exhibit that the core samples with higher clay content do not show great disparity between simulated and core permeability. These observations lead to the conclusion that the pore system of the less brittle core samples, samples with less presence of

microfractures, are less affected. Moreover sensitivities run in the simulator show that a variation in fracture density and pore throat size have a significant effect of one to two orders of magnitude on permeability hence capillary pressure values.

Further work included testing the feasibility of using core capillary pressure to calibrate a saturation height function to obtain a water saturation profile at the log scale. A full petrophysical evaluation is performed to obtain a water saturation profile from resistivity logs. As a quality assurance, the water saturation profile derived from capillary pressure is compared to the log derived water saturation. The water saturation profiles obtained from these two techniques are comparable to each other. To optimize the core calibrating process, a methodology founded on the hydraulic flow unit concept is proposed. The application of this methodology improves the comparison between water saturation profiles from capillary pressure and resistivity logs.

Despite the uncertainties associated with capillary pressure core measurements in this field, this research shows that these measurements integrated with other data are valuable to characterize rock properties at different scales

TABLE OF CONTENTS

| | |
|--|------|
| ABSTRACT..... | iii |
| LIST OF FIGURES | viii |
| LIST OF TABLES..... | xiii |
| ACKNOWLEDGEMENTS..... | xiv |
| CHAPTER 1 INTRODUCTION..... | 1 |
| 1.1 Objective..... | 2 |
| 1.2 Field Description..... | 3 |
| 1.2.1 Geological Setting..... | 4 |
| 1.2.2 Rock, Reservoir and Fluid Properties..... | 6 |
| 1.3 Methodology..... | 10 |
| CHAPTER 2 LITERATURE REVIEW | 12 |
| 2.1 Leverett J-Function..... | 16 |
| 2.2 Brooks and Corey..... | 17 |
| 2.3 Lambda Function..... | 18 |
| 2.4 Modified-Lambda Function (FZI- λ)..... | 19 |
| 2.5 Thomeer’s Hyperbola Model..... | 20 |
| 2.6 Wu Model (Modified Thomeer)..... | 23 |
| 2.7 Capillary Pressure Empirical Correlations..... | 25 |
| 2.8 Pore Throat Radius (r_p) Correlation..... | 27 |
| 2.9 Valvatne’s Pore Network Model..... | 29 |
| 2.10 Summary..... | 29 |
| CHAPTER 3 CAPILLARY PRESSURE EVALUATION USING PORE SCALE MODELING..... | 31 |
| 3.1 Pore Scale Model - Valvatne (2004)..... | 31 |
| 3.2 Description of Core Data and Capillary Pressure from Core Measurements..... | 34 |

| | |
|--|-----|
| 3.3 Pore Scale Modeling Matching Core Measurements..... | 41 |
| 3.4 Pore Scale Modeling and Effect of Fracture Aperture and Density..... | 47 |
| 3.5 Summary..... | 50 |
| CHAPTER 4 CAPILLARY PRESSURE EVALUATION AT THE LOG | |
| SCALE..... | 51 |
| 4.1 Formation Evaluation..... | 52 |
| 4.1.1 Volume of Shale (Vsh)..... | 53 |
| 4.1.2 Porosity..... | 56 |
| 4.1.3 Water Saturation..... | 57 |
| 4.1.4 Permeability..... | 64 |
| 4.1.5 Rock Typing – Hydraulic Flow Units Determination..... | 64 |
| 4.2 Modeled Capillary Pressure Water Saturation and Log Derived Water Saturation.... | 67 |
| 4.3 Summary..... | 70 |
| CHAPTER 5 DISCUSSION OF RESULTS..... | |
| 5.1 Results from Pore Scale Simulation..... | 71 |
| 5.2 Results from Log Analysis..... | 72 |
| 5.3 General Remarks..... | 73 |
| CHAPTER 6 CONCLUSIONS AND RECOMMENDATIONS..... | |
| 6.1 Conclusions..... | 74 |
| 6.2 Recommendations..... | 75 |
| NOMENCLATURE..... | 77 |
| REFERENCES..... | 81 |
| APPENDIX A SUPPLEMENTARY LITERATURE REVIEW..... | 87 |
| APPENDIX B CORE AND CAPILLARY PRESSURE DATA..... | 93 |
| APPENDIX C RESULTS FROM PORE SCALE SIMULATION..... | 110 |
| APPENDIX D LOG ANALYSIS RESULTS..... | 125 |

| | |
|---|-----|
| APPENDIX E PORE SCALE SIMULATION WORKFLOW | 133 |
| APPENDIX F SATURATION HEIGHT FUNCTION WORKFLOW..... | 135 |

LIST OF FIGURES

| | |
|--|----|
| Figure 1.1 Field map showing wells locations and drilling dates..... | 3 |
| Figure 1.2 3D map showing Field M structural complexity..... | 4 |
| Figure 1.3 Diagram of clastic depositional environments..... | 5 |
| Figure 1.4 Thin section from Well 3 illustrating the presence of microfractures on Formation H.7 | 7 |
| Figure 1.5 Porosity model based on storage capacity..... | 8 |
| Figure 1.6 Field M permeability model components..... | 9 |
| Figure 2.1 Experimental setup to illustrate capillary pressure theory..... | 12 |
| Figure 2.2 Capillary pressure profile relationship to pore throat distribution..... | 15 |
| Figure 2.3 Capillary pressure profile relationship to pore throat distribution and permeability for three dolomite core samples..... | 16 |
| Figure 2.4 Schematic of Thomeer’s Model Parameters..... | 21 |
| Figure 2.5 Typical petrophysical parameters based on pore geometry..... | 29 |
| Figure 3.1(a) 3D voxel image for the Berea sandstone..... | 32 |
| (b) Network of pores and throats extracted from the 3D voxel of the Berea sandstone..... | 32 |
| Figure 3.2 rp_{35} Diagnostic plot used to establish pore throat radius size range for microfractures..... | 37 |
| Figure 3.3 Available mercury injection capillary pressure curves semi-log plot used to diagnostic the dataset..... | 39 |
| Figure 3.4 Semi-log plot of incremental mercury injection capillary pressure curves used to diagnostic the dataset..... | 40 |
| Figure 3.5 Well 2 sample Ref #16 capillary pressure match of experimental data to a pore throat distribution generating using a Weibull distribution..... | 42 |
| Figure 3.6 Well Sample Ref #16 comparison of original and iterated pore throat size distribution..... | 43 |
| Figure 3.7 Data fitting to determine Weibull distribution parameters..... | 44 |

| | |
|--|-----|
| Figure 3.8 Well 2 sample Ref #16 histogram of the pore throat radius distribution..... | 44 |
| Figure 3.9 Well 2 Sample Ref #16 results of capillary pressure curves match..... | 46 |
| Figure 3.10 Well 2 Sample Ref #16 comparison between original and iterated pore throat diameter size distribution..... | 46 |
| Figure 3.11 Well 4 Sample Ref #69 simulated relative permeability curves from capillary pressure calibrated network..... | 47 |
| Figure 3.12 Summary plot showing the effect of varying pore throat size distribution and coordination number in the capillary pressure profile..... | 48 |
| Figure 3.13 Summary plot showing the effect of varying pore throat size distribution and coordination number in relative permeability curves..... | 49 |
| Figure 4.1 Average mineral composition for Field M target formation..... | 54 |
| Figure 4.2 Log plot showing the results from the multi-mineral model to estimate simplified lithology for Well 3..... | 55 |
| Figure 4.3 Log plot showing the results of Vsh estimation for Well 3..... | 55 |
| Figure 4.4 Log plot showing the results for effective porosity estimation for Well 3..... | 56 |
| Figure 4.5 Log plot used to estimate R_w in a known water wet zone Well 2..... | 59 |
| Figure 4.6 Log plot used to define predominant HFU for Well 3..... | 67 |
| Figure 4.7 Results from applying saturation height function in Well 3..... | 69 |
| Figure B-1 Well 2 mercury capillary pressure profiles..... | 102 |
| Figure B-2 Well 3 mercury capillary pressure profiles..... | 103 |
| Figure B-3 Well 4 mercury capillary pressure profiles..... | 103 |
| Figure B-5 Well 4ST mercury capillary pressure profiles..... | 104 |
| Figure B-6 Well 5 mercury capillary pressure profiles..... | 104 |
| Figure B-7 Well 3 Ref #44 pore throat radius histogram..... | 105 |
| Figure B-8 Well 4 Ref #52 pore throat radius histogram..... | 105 |
| Figure B-9 Well 4 Ref #58 pore throat radius histogram..... | 106 |
| Figure B-10 Well 4 Ref #66 pore throat radius histogram..... | 106 |

| | |
|---|-----|
| Figure B-11 Well 4 Ref #69 pore throat radius histogram..... | 107 |
| Figure B-12 Well 4ST Ref #74 pore throat radius histogram..... | 107 |
| Figure B-13 Well 4ST Ref #82 pore throat radius histogram..... | 108 |
| Figure B-14 Well 5 Ref #87 pore throat radius histogram..... | 108 |
| Figure B-15 Well 4 5 Ref #88 pore throat radius histogram..... | 109 |
| Figure C-1 Well 2 Sample Ref #16 simulated relative permeability curves from capillary pressure calibrated network..... | 111 |
| Figure C-2 Well 3 Sample Ref #44 results from capillary pressure curves match..... | 111 |
| Figure C-3 Well 3 Sample Ref #44 comparison between original and iterated pore throat size distribution..... | 112 |
| Figure C-4 Well 3 Sample Ref #44 simulated relative permeability curves from capillary pressure calibrated network..... | 112 |
| Figure C-5 Well 3 Sample Ref #52 results for capillary pressure curves match..... | 113 |
| Figure C-6 Well Sample Ref #52 comparison between original and iterated pore throat size Distribution..... | 113 |
| Figure C-7 Well 3 Sample Ref #52 simulated relative permeability curves from capillary pressure calibrated network..... | 114 |
| Figure C-8 Well 4 Sample Ref #58 results for capillary pressure curves match..... | 114 |
| Figure C-9 Well 4 Sample Ref #58 comparison between original and iterated pore throat size distribution..... | 115 |
| Figure C-10 Well 4 Sample Ref #58 simulated relative permeability curves from capillary pressure calibrated network..... | 115 |
| Figure C-11 Well 4 Sample Ref #66 results for capillary pressure curves match..... | 116 |
| Figure C-12 Well 4 Sample Ref #66 comparison between original and iterated pore throat size distribution..... | 116 |
| Figure C-13 Well 4 Sample Ref #66 simulated relative permeability curves from capillary pressure calibrated network..... | 117 |

| | |
|--|-----|
| Figure C-14 Well 4ST Sample Ref #69 results for capillary pressure curves match..... | 117 |
| Figure C-15 Well 4ST Sample Ref #69 comparison between original and iterated pore throat size distribution..... | 118 |
| Figure C-16 Well 4ST Sample Ref #69 simulated relative permeability curves from capillary pressure calibrated network..... | 118 |
| Figure C-17 Well 4ST Sample Ref #74 results for capillary pressure curves match..... | 119 |
| Figure C-18 Well 4ST Sample Ref #74 comparison between original and iterated pore throat size distribution..... | 119 |
| Figure C-19 Well 4ST Sample Ref #74 simulated relative permeability curves from capillary pressure calibrated network..... | 120 |
| Figure C-20 Well 4ST Sample Ref #82 results for capillary pressure curves match..... | 120 |
| Figure C-21 Well 4ST Sample Ref #82 comparison between original and iterated pore throat size distribution..... | 121 |
| Figure C-22 Well 4ST Sample Ref #82 simulated relative permeability curves from capillary pressure calibrated network..... | 121 |
| Figure C-23 Well 5 Sample Ref #87 results for capillary pressure curves match..... | 122 |
| Figure C-24 Well 5 Sample Ref #87 comparison between original and iterated pore throat size distribution..... | 122 |
| Figure C-25 Well 5 Sample Ref #87 simulated relative permeability curves from capillary pressure calibrated network..... | 123 |
| Figure C-26 Well 5 Sample Ref #88 results for capillary pressure curves match..... | 123 |
| Figure C-27 Well 5 Sample Ref #88 comparison between original and iterated pore throat size distribution..... | 124 |
| Figure C-28 Well 5 Sample Ref #88 simulated relative permeability curves from capillary pressure calibrated network..... | 124 |
| Figure D-1: Well 1 Log plot to summarize log derived petrophysical properties..... | 128 |
| Figure D-2: Well 3 Log plot to summarize log derived petrophysical properties..... | 129 |

Figure D-3: Well 3 Log plot to summarize log derived petrophysical properties.....130
Figure D-4: Well 4ST Log plot to summarize log derived petrophysical properties.....131
Figure D-5: Well 5 Log plot to summarize log derived petrophysical properties.....132
Figure E-1: Pore scale simulation workflow summarizing the steps taken in the evaluation.....134
Figure F-1: Saturation height function workflow summarizing the steps in the evaluation.....136

LIST OF TABLES

| | |
|--|-----|
| Table 2.1 Typical petrophysical Parameters Based on Pore Geometry..... | 28 |
| Table 3.1 Petrophysical and Composition for Rock Samples with Special Core Analysis..... | 34 |
| Table 3.2 Petrophysical Parameters Based on Pore Geometry for Field M..... | 35 |
| Table 4.1 Field M Available Log Curves..... | 52 |
| Table 4.2 Hydraulic Flow Units to Select Capillary Pressure Profiles..... | 65 |
| Table A-1 Water Saturation Models..... | 91 |
| Table A-2 Cementation Exponent Models-Correlations..... | 89 |
| Table A-3 Selected Correlation for Log Derived Porosity..... | 89 |
| Table A-4 Permeability Models/Correlations..... | 90 |
| Table A-5 Selected Flow Units Concepts..... | 92 |
| Table B-1 Core Permeability, Porosity and Grain Density..... | 94 |
| Table B-2 Capillary Pressure Data..... | 97 |
| Table D-1 XRD Data Summary..... | 126 |

ACKNOWLEDGEMENTS

The present research would not have been possible without the data provided by Repsol YPF Bolivia. Thank you for supporting this research endeavor.

I would also like to thank my mother, Irene, and my family for their continuing encouragement during the time of my studies. To my brother Franco, who inspired me to become a petroleum engineer and I consider an outstanding engineer and mentor. To my brother Cristian an upcoming engineer and my sister Melina. To Jason W. Leal who encouraged me during the last stages of this work.

A special thank you for Dr. Ramona Graves and Dr. Roberto Aguilera. They both are responsible for making my experience in graduate school one of the most fulfilling times of my life. I will always be thankful for crossing your paths.

I also want to thank the Colorado School of Mines Petroleum Engineering Department as a whole. The administrators Patti, Terri and Denise, who are amazing individuals thank you for your help and encouragement. Thank you to the professors who are always willing to share their knowledge and last but not least my colleagues and friends.

CHAPTER 1

INTRODUCTION

The evaluation of field capillary pressure is critical to assess and model fluid flow through porous media. Capillary pressure profiles are used to map fluid saturations, and to identify fluid contacts for well placement. Thus, the continued interest to investigate new methodologies to improve existing means to estimate this fluid-rock property on a field scale.

The present work is motivated by the need to improve the understanding of capillary pressure behaviour for Field M. This research presents an integrated analysis using different methodologies to evaluate the capillary pressure curves for Field M.

Field M has been classified as anaturally fractured tight matrix gas reservoir and it is located in Bolivia. The reservoir rock of Field M was deposited in a marine estuary environment resulting in a lithology progression that vertically varies on different degrees of sand shale mixtures. The field's fracture system has been originated from extreme tectonic movements in the area. The presence of highly conductive fractures and the uncertainty of their location have limited the number of wells. Four wells have been drilled on the structure of Field M one of which has watered out. The field, still in the developing stage, was discovered on 1999, but sustained production started in 2005 (Repsol, 2010). The interest to continue developing this field and to avoid early water production motivated this research.

Field M, in terms of petrophysical assessment, is considered a highly complex reservoir. This complexity derives from a combination of factors that include: the field geological structure, the departure of the reservoir rock from clastic clean conventional sandstones

(shaliness and non-intergranular porosity), the difficulty to simulate the field high pressure and temperature on core measurements, the small number of wells drilled on the structure and the limited amount of specialized data. The wide range of fracture size is another challenge for the petrophysical evaluation. The presence of fractures, varying in size length from microns to meters, make core measurements incapable to evaluate properties that include all pore types. In short, Field M possesses all the characteristics that describes a problematic reservoir for the purposes of petrophysical evaluation, (Worthington,2010). Due to the complexity of the field of study and the specific objective provided by the operator of this field, the scope of the research focuses on the evaluation of capillary pressure.

1.1 Objective

The main objective of this research is to improve the understanding of capillary pressure curve profiles in Field M using available data. The approach used in this research is to evaluate capillary pressure at different scales and then integrate the results. The two main steps of this approach are: 1) the validation of core capillary pressure curves and 2) the development of a sound methodology to model capillary pressure curves at the log scale.

During the course of this research additional contributions to the previous petrophysical evaluations have been developed. These contributions include the introduction of a new workflow to evaluate this reservoir, the establishment of flow units to evaluate capillary pressure and other petrophysical properties and identifying potential future improvements for petrophysical evaluation.

1.2 Field Description

Figure 1.1 shows the location of the study area on the southern part of Bolivia. Field M has approximately 82 BCM (2.9 TCF) of natural gas proved reserves and has been producing at sustained rates of approximately 6.4 MCMD (83 MMCFD) since 2005. To date, the field has produced close to 3.5 BCM (124 BCF) or approximately 4% of the estimated reserves. Production in this field comes from three wells, Wells 1, 3 and 4, out of four wells drilled in the area (Figure 1.1). Well 5 is drilled in another field which appears to be an extension of Field M and it is included in this research. Well 2 stopped natural gas production in 2002 due to early water encroachment. Wells 1 and 4 completion design consists of 4 1/2 inches perforated liner, whereas Wells 2 and 3 have an open-hole completion (Repsol, 2010).

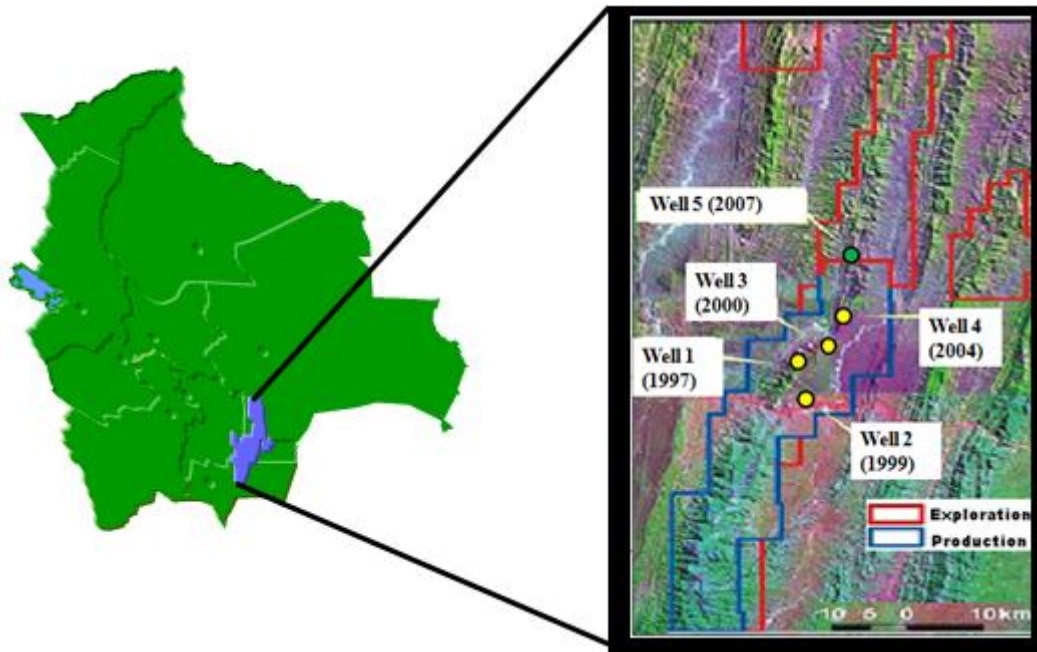


Figure 1.1:Field map showing wells locations and drilling dates. Modified from Repsol 2010.

1.2.1 Geological Setting - Summary from Various Geological Evaluations

Field M is located in the Devonian basin on the southern-south Andean structural zone of Bolivia, and it covers an area of 874 Km²(337.45 square miles). The reservoir in Field M is an asymmetric northeast-southwest elongated anticline with large structural complexity due to folding and faulting resulting from tectonic events in the area (Figure 1.2). As observed in Figure 1.2 Field M structure is placed between two regional faults, B and M. The field structure is described as an imbricate duplex thrust system. One important observation from the field's structural analysis is the hypothesis that regional fault B and M might have impacted the structure where Field M is located in different ways. Thus, the shallow structure is likely to be different from the deepest structure. This has significant impact on the fracture density (Repsol,2010).

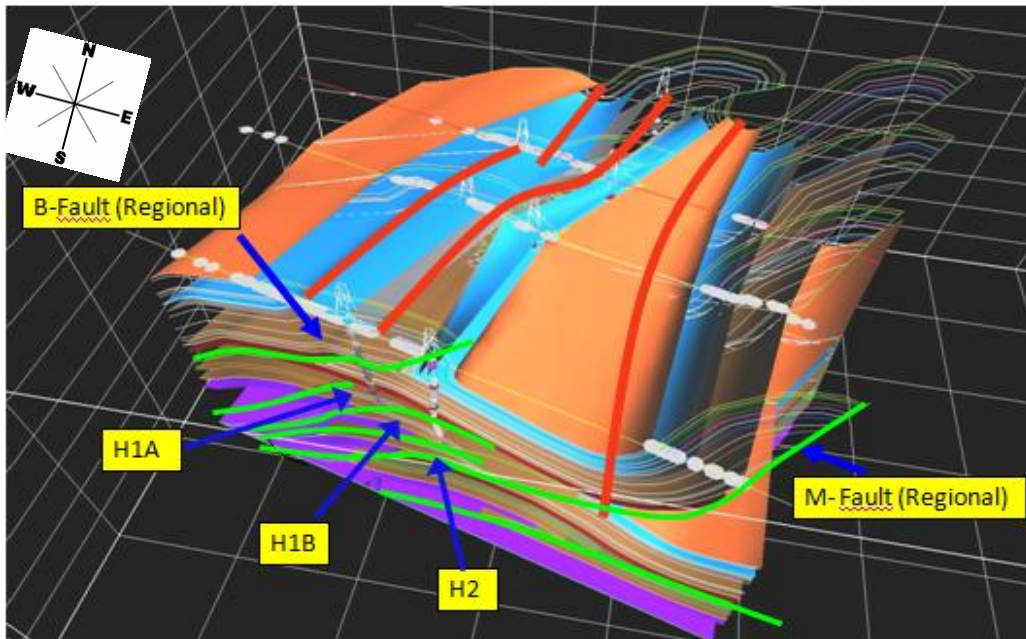


Figure 1.2: 3D map showing Field M structural complexity. Modified from Repsol (2010).

The targeted formation H is typically found between 3,000 and 4,000 meters measured depth (9,842 and 16,404 feet) and averages a thickness of 250 meters (820.21 feet). Formation H is located at the footwall of regional fault B, is subdivided by faults into layers H1a, H1b and H2 (Figure 1.2). Formation H was deposited as an estuary marine deltaic environment dominated by high energy waves. The ellipse in Figure 1.3 illustrates the general depositional environment system on which formation H was deposited. The reservoir rock was deposited on a transition region between river and marine environments and exposed to high and low depositional energy and with inflow of fresh and saline water. The lithology of H formation is mainly composed of clean tight quartzitic sandstones with occasional alternating thin shale laminations. Based on depositional parasequences Formation H has been divided from top to bottom into Layer 1, Layer 2 and Layer 3. Layers 1 and 2 are considered good reservoir rock quality unlike Layer 3 which is a shaly sandstone with poor reservoir quality.

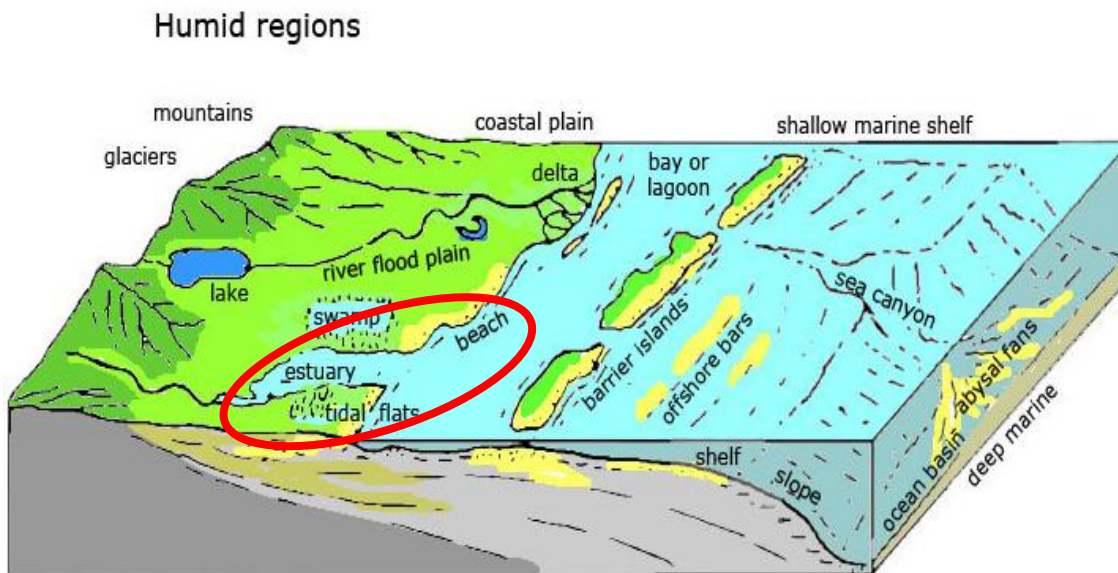


Figure 1.3: Diagram of clastic depositional environments (GeoZeum, 2012).

Further geological evaluation of the layers resulted in subdivisions consisting of four facies from bottom to top: A, B, C and D. Facies A is the bottom part of formation H and it was

deposited during the lower shoreface. The interval is a sequence of shale to sand with fine grains varying between sandstone and silt with presence of mica. Facies B is an interval deposited on the upper shoreface and is composed of sandstone with a grain size varying from fine to medium showing increasing presence of mica towards the bottom of the interval. Facies C is an interval that shows dark shale from an abrupt marine incursion with a varying thickness from 6 to 16 meters. This interval varies from shale to silt into the southeast direction while the shale increases to the north east dipping angle. Facies D is at the topmost of the Formation H. This is a sandstone with fine to medium grain sizes deposited between the upper shoreface and beach high energy environment feeding from an onshore river. This interval has the cleanest sandstone and presents an increasing upwards grain size. From the four facies, D is the cleanest sandstone and the best reservoir rock. Facies C is the worst reservoir quality rock (Repsol,2010).

The source rock, Los Monos, lays on top of Formation H. The evaluation of Formation H in an analogous field by Aguilera, et al.(2003) indicates that gas migration from the source to the reservoir rock was initiated with the dilatancy produced from fracturing and folding.

1.2.2 Rock, Reservoir and Fluid Properties

The reservoir rock in Field M is a result of complex diagenesis processes in which precipitation, cementation and compaction occluded the majority of primary porosity. The highly fractured reservoir contains fractures ranging in size from microns to swarms of fractures that can reach meters in width. These fractures constitute the source of the secondary porosity in this field. The intense fracturing makes the reservoir rock behave much like a dual porosity system with matrix and fractures, in which the matrix is composed of a large population of microfractures. Although the matrix porosity has other components like porosity from

dissolution and intergranular porosity, the bulk of the matrix porosity is made out of microfractures. Figure 1.3 is a thin section showing the tight matrix reservoir rock and the occurrence of microfractures (Repsol, 2008). Effective porosity values from core measurements range from 3% to 7% (Repsol, 2008). Other studies of Formation H on analogous fields have reported microfracture spacing ranging between 0.5 and 3.6 cm (Aguilera et al., 2003).

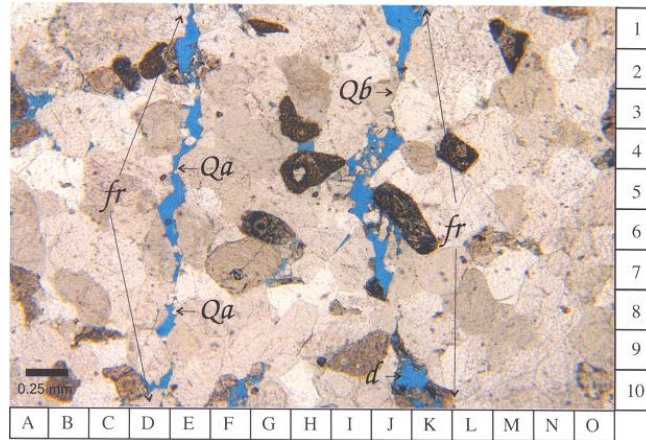


Figure 1.4: Thin section from Well 3 illustrating the presence of microfractures on Formation H. Fractures are denoted by the abbreviation fr (Repsol, 2008).

The geological evaluation of core measurements, outcrops, thin sections and structural analysis present evidence that the reservoir is made up of five different components. This leads to the porosity model shown on Figure 1.4, which is composed by macrofractures, low conductivity fractures, microfractures, fractured shale, and dispersed intergranular porosity. Previous analyzes of the field considered a fracture width a single component. However, this research divides the fracture porosity into macrofractures and low conductivity fractures. This allows to preserve the geological features in this study and to maintain consistency between the porosity and permeability models.

According to the naturally fractured reservoir type classification based on storativity provided by Aguilera (1995), reservoirs of Type A are characterized by having the bulk of the storage capacity in the matrix. Reservoirs of Type B are characterized by having approximately

half of the storage capacity in the matrix and the balance in the fractures. Reservoirs of Type C are characterized by having the majority of the storage capacity in the fractures. The reservoir in Formation H is classified as a Type C reservoir. Because the matrix in Formation H is formed by microfractures, this reservoir can also be classified as a Type A reservoir where natural gas flows from the matrix microfractures to the major fractures (Aguilera et al.,2003).

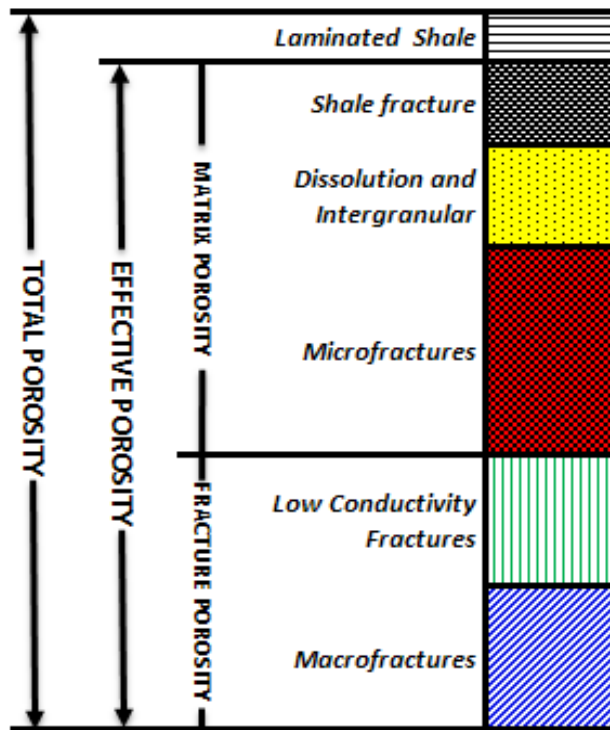


Figure 1.5:Porosity model based on storage capacity (Not to Scale). Modified from Repsol (2006).

Figure 1.5 illustrates the fluid flow model for Formation H from geological evaluation and production analysis. Due to the ample fracture scaling on the field from microns to several meters, the core measurements correspond to the evaluation of the matrix permeability. Reported core permeability are interpreted to correspond to the matrix rock. Reported core permeability ranges from 0.0003 mD to 0.2 mD (Repsol, 2008). Matrix permeability contributes little to the

production from individual wells, but it is important for the fluid flow in the reservoir rock that feeds the larger fractures (Aguilera et al., 2003). The low conductivity fractures (LCF) are the medium sized fractures that are not as well connected as the macrofractures. Analysis with numerical simulators shown that the poorly connected LCF permeability ranges from 10 mD to 18 mD. The macrofractures, fault like sized fractures, provide the productive permeability that allows the high commercial production rates on this field. The macrofractures permeability observed on well testing and numerical simulation varies from 2,000 mD to 7,000 mD (Repsol, 2010).

Additional evaluation of the fractures that were identified from image logs showed that only 23% are productive fractures. The evaluation consisted on flagging and ranking the fractures that showing productivity from results of production logging, mud losses, gas shows and analysis of perforations (Repsol, 2007).

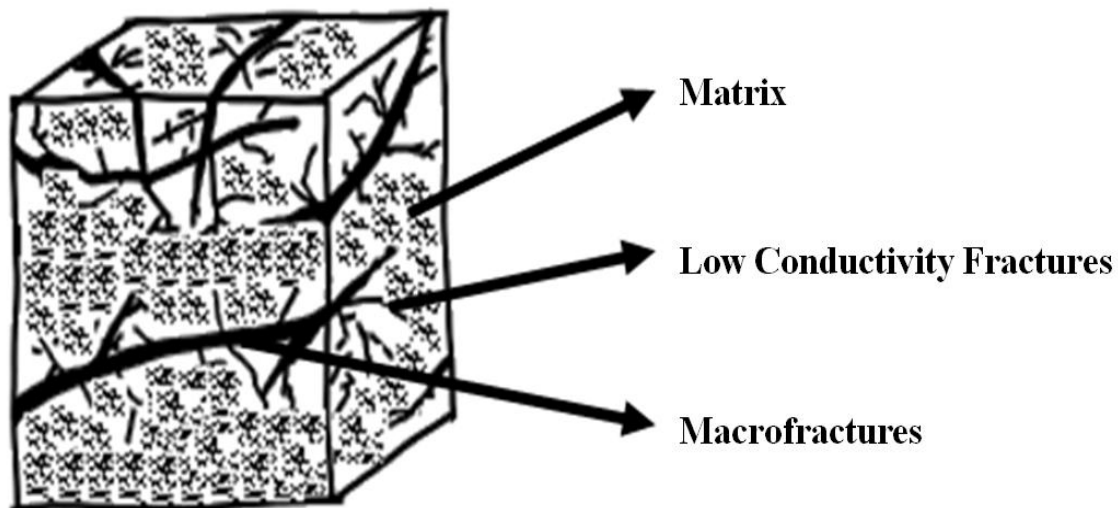


Figure 1.6:Field M permeability model components. Modified from Repsol (2010).

PVT data from the field confirmed the properties of a gas condensate reservoir with a gas-oil ratio in the order of 57 SCM/BBL (20,000 SCF/BBL). Gas in this field has a composition of 80% methane. The gas and oil specific gravity are 0.667 (density at surface conditions 0.738 to 0.804 gr/cm³) and 51.4°API respectively at surface conditions (Repsol, 2010).

Thin sections and XRD evaluations show the reservoir rock is composed mainly of quartz and clay, with a small percentage of feldspar and traces of mica. The clay type found on this area is a mix of illite and chlorite (Repsol, 2010).

1.3 Methodology

The main objective of this research is to evaluate capillary pressure at the core and log scale. The methodology adopted on this work is described next.

Chapter 2 includes a literature review of available capillary pressure methodologies along with a revision of additional concepts required to analyze the dataset.

Chapter 3 contains the results of a pore scale simulation that uses core data as the main input. The simulation is carried out to validate and understand the core capillary pressure curves and to analyze the effects of fracture aperture and density on the capillary pressure profiles. The simulation work is done using a non-commercial software developed as part of a doctoral dissertation at the Imperial College (Valvatne, 2004).

In Chapter 4 a log derived capillary pressure profile for each flow unit is generated using commercial software (Techlog). Three steps are followed: (1) Flow units are delineated from evaluating results from pore scale simulation and core data. (2) Saturation height algorithms

from fitting core capillary pressure curves are used to generate water saturation profiles at the log scale. The algorithms are derived to match core capillary pressure curves and flow units observed at the log scale using the flow unit evaluation from step 1. In this step knowledge of the free water level or fluid contact are required to apply the saturation height model. (3) The water saturation profiles derived from capillary pressure and the log derived water saturation profiles are compared for validation purposes.

Chapter 5 presents a discussion of the feasibility of integrating results from the various capillary pressure evaluations. Finally, Chapter 6 presents the final conclusions and recommendations for this research.

CHAPTER 2

LITERATURE REVIEW

Capillary pressure is a property that shows the interaction between rock and fluid properties. Figure 2.1 is a schematic of a simple experimental setup to illustrate the capillary pressure theory and the mathematical derivations for this property.

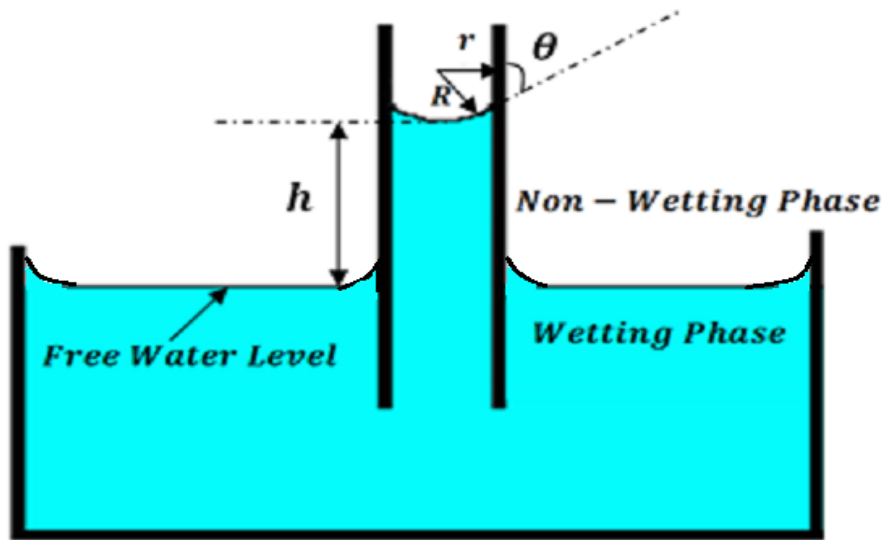


Figure 2.1: Experimental setup to illustrate capillary pressure theory.

The first formulation of capillary pressure is derived from the pressure difference between the wetting and non-wetting phase under static conditions at a height h . In Equation 2.1 this pressure difference is expressed in terms of fluids density, and height above the free water level.

$$P_c = h (\rho_w - \rho_{nw}) g \quad (2.1)$$

Where:

P_c = capillary pressure (psia),

ρ_w = wetting phase density (lbm/ft³),

ρ_{nw} = non-wetting phase density (lbm/ft³),

h = height above the free water level (ft),

g = gravitational constant

Equation 2.2 is another expression for capillary pressure based on Young-Laplace's equation (Christiansen, 2008). In this equation the wetting and non-wetting fluids pressure difference is related to the radius of curvature of the fluids interface assuming a spherical phase (R) and the interfacial tension (σ). From the schematic in Figure 2.1 it is observed that $R = r \cos \theta$. Replacing R Equation 2.3 results in a capillary pressure formulation in terms of the capillary radius (Washburn, 1921).

$$P_c = \frac{2\sigma}{R} \quad (2.2)$$

$$P_c = \frac{2\sigma \cos \theta}{r} \quad (2.3)$$

Where:

P_c = capillary pressure (psia),

σ = interfacial tension (dyn/cm),

$\cos \theta$ = contact angle (degrees),

r = pore throat radius (microns)

Equation 2.3 reveals that assuming a constant wettability and interfacial tension, the pore throat size variation controls the values of capillary pressure. Field M is a quartzitic sandstone gas

condensate reservoir with fluids and mineralogy fitting of a water-wet system. Typically analysis of the variation of interfacial tension and contact angle is a major concern in carbonate reservoirs. In the silica-clastics of Field M, however it is reasonable to assume that Field M is a homogenous water-wet system and that capillary pressure profiles are primarily dependant on the pore system.

Figure 2.2 demonstrates the capillary pressure profile variation with pore throat size distribution which is directly linked to the field pore system. A pore system is described in terms of porosity types such as intergranular, intragranular, dissolution and primary or secondary. The histogram in Figure 2.2 shows that the sample has a unimodal distribution with moderate pore throat size sorting.

Similarly Figure 2.3 illustrates the capillary pressure profiles for three dolomite samples with unimodal pore throat distribution. Comparing both figures, the three samples evidence that capillary pressure profiles shift to the upper right direction as the permeability and pore throat size sorting decreases.

Figures 2.2 and 2.3 do not show a direct relationship of capillary pressure profile to a porosity value, however the pore throat size distribution presented in these figures can be associated to pore types. Because the definition of a pore type system is field specific, discussion of this relationship for Field M is provided in Chapters 3 and 4.

It is widely accepted that petrophysical properties, capillary pressure, water saturation, porosity, and permeability, are interrelated to one another and to the pore size distribution (Archie, 1942). In this chapter, algorithms to model capillary pressure relating some or all

petrophysical properties are reviewed. Additional concepts for this evaluation are summarized on Appendix A.

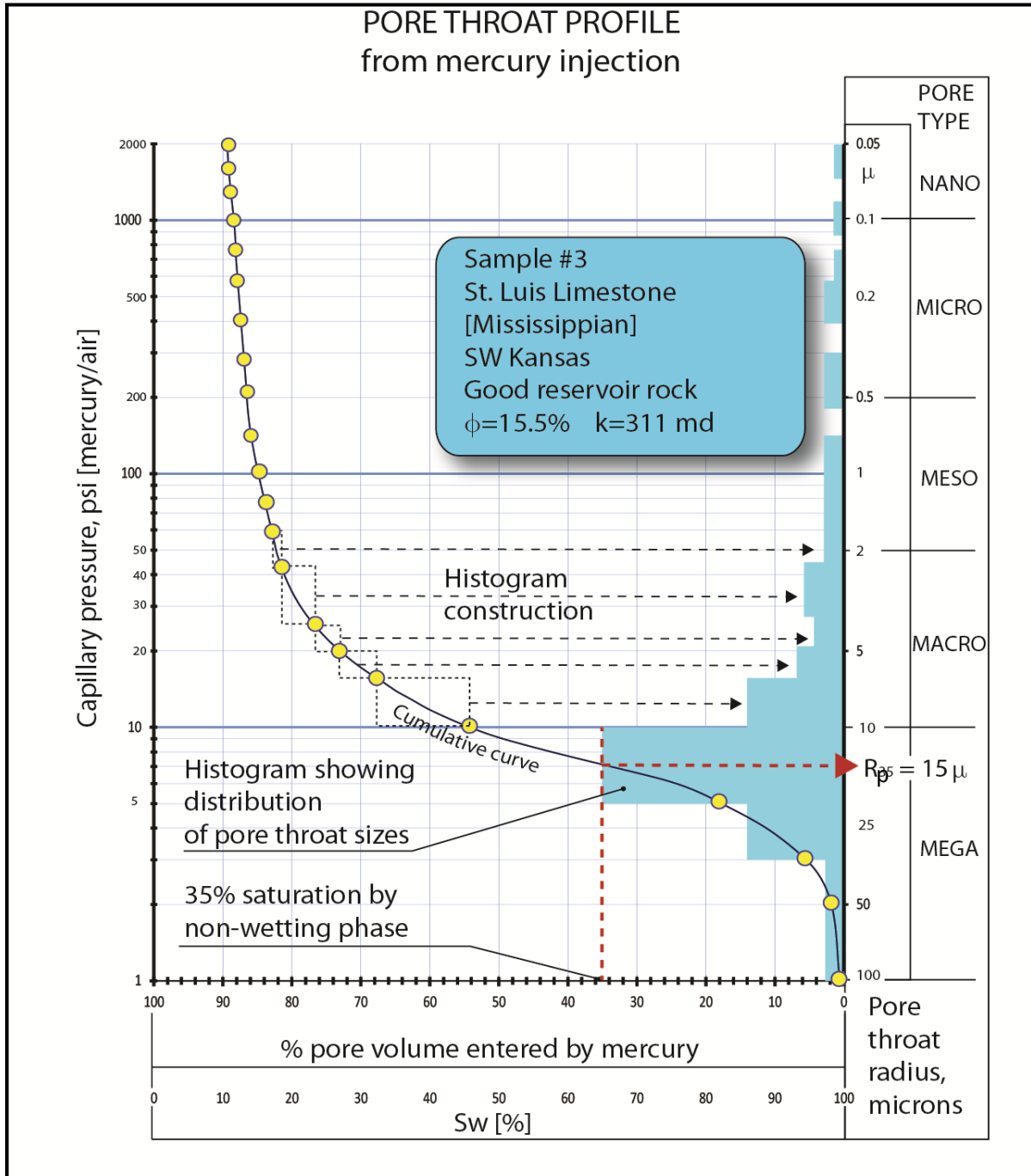


Figure 2.2: Capillary pressure profile relationship to pore throat distribution. Recreated from Beaumont and Foster, (1995).

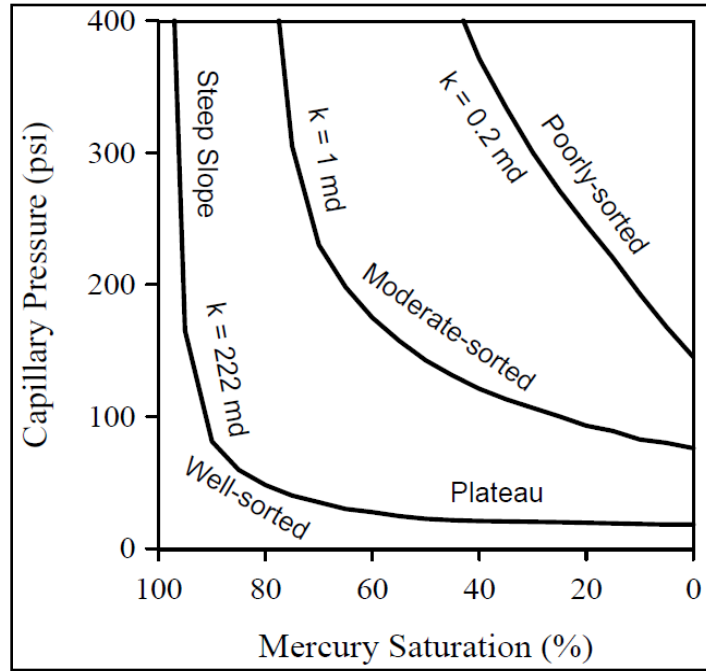


Figure 2.3: Capillary pressure profile relationship to pore throat distribution and permeability for three dolomite core samples (Wu, 2004).

2.1 Leverett J-Function

The J-function was developed in an attempt to obtain a dimensionless function to average core capillary pressure curves to obtain the most representative curve for a field (Leverett, 1939, 1941). Leverett recognized that the pore throat radius (r) in the equation developed by Washburn (1921), Equation 2.3, could be expressed in terms of porosity and permeability. From the Poiseuille's law applied to identical cylindrical tubes, Leverett derived Equation 2.4 to calculate the average pore radius.

$$r_p = \sqrt{\frac{8k}{\phi}} \quad (2.4)$$

In 1941, Leverett acknowledged that capillary pressure should depend on porosity and permeability so he developed a dimensionless expression using the average pore radius equation

(Equation 2.5). The dimensionless function is used to normalize core data and create a general plot of the J-function versus water saturation. Typically an averaged capillary pressure curve from this plot is obtained from regression analysis using a power law equation (Equation 2.6).

$$J(S_w) = \frac{P_c}{\sigma \cos \theta} \sqrt{\frac{k}{\phi}} \quad (2.5)$$

$$J = a(S_w)^b \quad (2.6)$$

Where:

J = dimensionless function,

P_c = capillary pressure (psia),

σ = interfacial tension (dyn/cm),

k = permeability (md),

ϕ = porosity (fraction),

S_w = water saturation (fraction),

a, b = fitting parameters,

σ = interfacial tension (dyn/cm)

The J-function was developed to evaluate a single rock type, but a more appropriate use is to generate a J-function for each rock type with similar pore structure (Wiltgen et al., 2003).

2.2 Brooks and Corey

Brooks and Corey (1964, 1966) developed an empirical correlation based on the concept of threshold pressure (P_d). The threshold pressure is an inflection point, on the capillary pressure profile, that indicates pressure reached a maximum value to form a continuous network across

the sample. The variable lambda (λ) describes pore size distribution on the core samples. Equation 2.7 displays this model while Equation 2.8 shows the effective saturation in terms of irreducible saturation added later.

$$S_e = \left(\frac{P_c}{P_d} \right)^{-\lambda} \quad (2.7)$$

$$S_e = \frac{S_w - S_{wir}}{1 - S_{wir}} \quad (2.8)$$

Where:

P_c = capillary pressure (psia),

P_d = threshold pressure (psia),

λ = pore size distribution (dimensionless),

S_e = effective water saturation movable water (fraction),

S_w = water saturation (fraction),

S_{wir} = irreducible water saturation (fraction)

2.3 Lambda Function

The lambda function assumes that the areal variation of effective porosity is the main predictor for water saturation (Equation 2.9). Variables a and b are regression constants obtained from porosity-permeability curve fitting analysis. Equation 2.10 relates the lambda function to a constant water saturation and height above the free water level. The assumption of a constant initial water saturation in this model might not characterize the current state of the field (Wiltgen et al., 2003).

$$\lambda = e^{a+b \ln(\frac{\phi_e}{100})} \quad (2.9)$$

$$S_w = a h^{-\lambda} \quad (2.10)$$

Where:

λ = pore size distribution (dimensionless),

ϕ_e = effective porosity (fraction),

a, b= fitting parameters,

S_w = water saturation (fraction),

h = height above the free water level (feet)

2.4 Modified-Lambda Function (FZI- λ)

There are various forms of the lambda function, one interesting formulation is proposed by Biniwale (2005). The modified-lambda function includes the hydraulic flow zone unit term to emphasize geological and petrophysical aspects (Behrenbruch and Biniwale, 2005).

The hydraulic flow zone unit (FZI), in geological terms, concept was introduced by Ebanks (1987). He pointed out that reservoir characterization is best when the reservoir is subdivided in lithofacies with common geological attributes. Later Amaefule et al.(1993) extended this concept by grouping zones with similar petrophysical properties using the Kozeny-Carman (1927, 1937, 1956) equation. He proposed a more quantitative approach to select FZI and introduced a reservoir quality index (RQI), which is equivalent to the pore throat radius average proposed by Leverett in (1939). Refer to Appendix A to see these equations.

The FZI- λ model has been successfully tested in Australian fields. Equations 2.11 and 2.12 show the model components.

$$S_w = A (h - h_d)^{-\lambda} \quad (2.11)$$

$$S_w = \frac{A_1}{FZI^{A_2}} \left(h - \frac{h_1}{FZI^{h_2}} \right)^{-\frac{\lambda_1}{FZI^{\lambda_2}}} \quad (2.12)$$

Where:

All variables with subscripts 1 and 2 are field specific constants obtained from capillary pressure core data and optimization methods.

λ = pore size distribution (dimensionless),

S_w = water saturation (fraction),

h = height above the free water level (feet),

h_d = height above the free water level at the entry pressure

2.5 Thomeer's Hyperbola Model

Thomeer (1960) used 279 capillary pressure profiles from core samples and developed a semi-empirical mathematical model. He approximated capillary pressure profiles from experimental data in a log-log plot to a hyperbolic function (Equation 2.13).

$$\frac{S_b}{S_{b\infty}} = e^{-F_g / \log\left(\frac{P_c}{P_d}\right)} \quad (2.13)$$

Where:

P_c = capillary pressure (psia),

P_d = displacement pressure, graphically equivalent to threshold pressure (psia),

F_g = pore geometric factor, which defines the shape of the capillary pressure curve (dimensionless),

S_b = bulk mercury saturation, ratio of mercury volume and bulk volume, (fraction),

$S_{b\infty}$ = bulk mercury saturation at infinite pressure assumed equal to porosity (fraction)

Low values of F_g indicate well sorted pore throats while high values indicate poorly sorted pore throats resembling Figure 2.2 where capillary pressure is associated to the pore throat distribution. In that sense, F_g can be viewed as the equivalent of the pore throat radius. Therefore low values of F_g are related to high permeability and high F_g are related to low permeability (Thomeer, 1960). Figure 2.4 shows graphically the relationship between the variables in Equation 2.5.1 and the pore geometry trends.

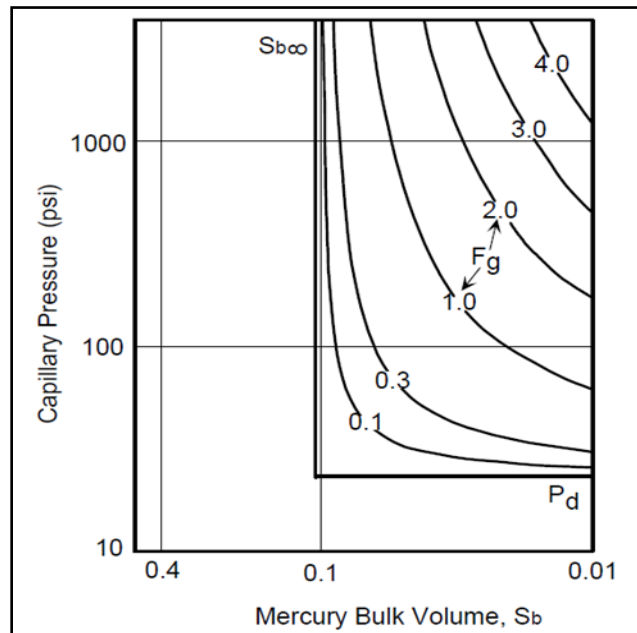


Figure 2.4: Schematic of Thomeer's Model Parameters (Wu, 2004).

Thomeer (1983) investigated core samples and developed an equation that relates permeability to $S_b, S_{b\infty}$ and F_g . The study includes a petrographic evaluation of the pore

geometrical factor and its relationship to permeability. The coordinates of the hyperbola's center are defined using a method proposed by Swanson (1981). The coordinates of this point, also known as apex, are located at a point where a 45 degree line touches the capillary pressure curve. This line has to be drawn in a capillary pressure versus mercury saturation log-log plot with identical log cycle scales in the x and y axis.

Equation 2.14 is a power law function which is the best fit to correlate these variables. The resemblance of the average pore throat radius to F_g defined by Leverett (1939) is again observed through the incorporation of permeability.

$$k = 3.8068 F_g^{-1.3334} \left(S_{b^\infty} / P_d \right)^{2.0} \quad (2.14)$$

Where:

k = permeability (mD),

F_g = pore geometric factor, defines the shape of the capillary pressure curve (dimensionless),

S_{b^∞} = bulk mercury saturation at infinite pressure assumed equal to porosity (fraction),

P_d = displacement pressure, graphically equivalent to threshold pressure (psia)

Thomeer highlights the importance of identifying and linking pore geometries to petrophysical parameters. McCreesh et al.(1991) demonstrates that describing pore type and throat size from thin section analysis has a great impact in the evaluation of capillary pressure profiles.

2.6 Wu Model (Modified Thomeer)

F_g is not always easy to estimate, because not all capillary pressure curves fit a hyperbolic profile. This is particularly true for shaly reservoirs and tight rocks with low permeability, where bimodal pore throat size distributions might occur (Wu, 2004). Equation 2.15 shows the modified Thomeer's model proposed by Wu, which introduces the shape factor β . The model was tested using 200 core samples from different lithologies resulting in β values ranging between 1 and 3. A value $\beta = 1$ for tight shaly sandstones with micropores and permeability values less than 1 mD is recommended. Wu provides an empirical correlation (Equation 2.16) to facilitate the estimation of P_d .

$$P_c = P_d + \sigma \cos \theta \sqrt{\frac{\phi}{k}} \left(\frac{\ln 1}{S_e} \right)^\beta \quad (2.15)$$

$$\ln P_d = 5.458 - 1.255 \ln \sqrt{k/\phi} + 0.08 (\ln \sqrt{k/\phi})^2 \quad (2.16)$$

Where:

P_c = capillary pressure (psia),

P_d = threshold pressure (psia),

β = shape factor (dimensionless),

σ = interfacial tension (dyn/cm),

$\cos \theta$ = contact angle (degrees),

k = permeability (md),

ϕ = porosity (fraction),

S_e = effective water saturation, movable water (fraction)

Wu (2004) also proposed a capillary pressure based permeability model based on Thomeer (1983) that includes the cementation exponent (m) (Equation 2.17). This is an analytical-empirical formulation that recognizes the relationship between Archie, Kozeny-Carman and other formulations.

$$k = CF_g^{-1.33}[\phi(1 - S_{wir})/P_d]^m \quad (2.17)$$

$$\log\left(\frac{P_c}{P_d}\right) = -\frac{F_g}{\ln(1 - S_e)} \quad (2.18)$$

Where:

k = permeability (md),

C = fitting parameter,

F_g = pore geometry, it is the negative slope of equation 2.18 (dimensionless),

∅ = porosity (fraction),

S_{wir} = irreducible water saturation (fraction),

P_d = threshold pressure (psia),

m = cementation exponent as defined by Archie,

P_c = capillary pressure (psia),

S_e = effective water saturation, movable water (fraction)

The addition of m as a pore system descriptor is proposed by Aguilera (2003a). In this work an extended Picket Plot, that includes pore throat aperture radius, capillary pressure, height above the free water level and pore throat, is presented as a graphical tool to evaluate properties for a constant capillary pressure. Other works (Deng, et al.,2011; Sivila, et al., 2011; Aguilera

and Aguilera, 2003b; Aguilera, 2003a; Al-Ghamdi et al., 2010; Hagiwara, 1986; Revil and Cathles, 1999) also evidence m as a pore type system characterization tool.

2.7 Capillary Pressure Empirical Correlations

Kwon and Pickett (1975) presented an empirical correlation to fit data in a log-log plot of permeability porosity ratio and capillary pressure. The model was developed using mercury injection capillary pressure data from 2,500 core samples. The authors defined the variable A as a function of water saturation and B as a value close to 0.45.

$$P_c = A \left(\frac{k}{100\phi} \right)^{-B} \quad (2.19)$$

To facilitate the estimation of A , the following equation is suggested (Aguilera, 2002):

$$A = 19.5 S_w^{-1.7} \quad (2.20)$$

Where:

P_c = capillary pressure (psia),

k = permeability (md),

ϕ = porosity (fraction),

S_w = water saturation (fraction)

Swanson (1981) developed another empirical correlation, Equation 2.21, using capillary pressure data to estimate permeability. The correlation aims to identify the maximum capillary pressure where well connected pore throat separate from the not so well connected pore throats.

This maximum point is known as the apex and it is determined using a 45 degree tangent line in a log-log plot of capillary pressure versus bulk mercury saturation.

$$k = 355 \left(\frac{S_b}{P_c}_{max} \right)^{2.005} \quad (2.21)$$

Wells and Amaefule (1985) proposed a modification to Swanson's model by deriving a new correlation using data from low permeability or tight gas sands in a mercury air system (Equation 2.22).

$$k = 30.5 \left(\frac{S_b}{P_c}_{Max} \right)^{1.56} \quad (2.22)$$

Where:

P_c = capillary pressure at the apex (psia),

k = permeability (mD),

S_b = bulk volume occupied by mercury (percentage)

2.8 Pore Throat Radius (r_p) Correlation

The pore throat radius correlation (r_p) is an empirical equation with theoretical foundations on the pore throat average radius concept ($r_p = \sqrt{\frac{8k}{\phi}}$) presented by Leverett (1939).

The most known r_p correlations are: Windland (Published by Kolodzie, 1980), Pittman (1992), and Aguilera (2002).

Windland developed an r_p empirical correlation using the point at 35% mercury saturation instead of the Swanson's apex. He analyzed core measurements of 56 sandstones and

25 carbonate sample and concluded that at the 35% mercury saturation had the best correlation to permeability and porosity. Similarly, Aguilera (2002) used the data of 2,500 sandstones and carbonate samples to derive an r_p correlation at the 35% mercury saturation.

Pittman (1992), developed a correlation to estimate permeability based on the apex pore throat radius. The apex concept was introduced by Swanson, (1981) and it is defined as the maximum point in a plot of S_b/P_c and S_b , where: S_b is the bulk volume occupied by mercury (percentage), and P_c is the capillary pressure (psia). Below are the equations developed by these authors.

$$r_{pWinland} = 5.395 \left(\frac{k^{0.588}}{\phi} \right)^{0.864} \quad (2.23)$$

$$r_{pPittman} = 0.0534 \left(\frac{k^{0.8439}}{\phi^{1.3729}} \right) \quad (2.24)$$

$$r_{pAguilera} = 2.665 \left(\frac{k}{\phi} \right)^{0.45} \quad (2.25)$$

Where:

r_p = pore throat radius (microns),

k = permeability (mD),

ϕ = porosity (percentage)

The r_p method has been proved to be a significant tool to characterize zones with varying petrophysical properties. Table 2.1 is a summary of the typical petrophysical properties based on pore geometry and the corresponding pore throat size derived from Winland r_{p35} . Figure 2.5 presents the expected capillary pressure profiles associated with the values on Table 2.1.

Field M pore system is composed of fractures with apertures sizes that vary from microfractures to megafractures where fracture scale is an important constituent of petrophysical characterization. The integration of pore throat size with other petrophysical properties and the expected capillary pressure profiles presented in Figure 2.5 and Table 2.1 provide a framework for the analysis of results from pore scale simulation and log analysis. In this research the adopted porosity and permeability models for Field M have been adapted to follow this framework.

Table 2.1: Typical Petrophysical Parameters Based on Pore Geometry, Adapted from Coalson et al. and White (Aguilera, 2010)

| Category | Pore Size | Windland r_{p35} (microns) | kair (md) | Immobile S_w (%) | P_c Curve |
|------------------|-----------|------------------------------------|----------------|--------------------------|-------------|
| Intergranular | Mega | >10 | Extremely high | 15 | B |
| | Macro | 2--10 | High | 20 | C |
| | Meso | 0.5--2 | Moderate | 45 | D-E |
| | Micro | <0.5 | Low | 45-90 | E,F |
| Intercrystalline | Mega | >10 | Extremely high | 15 | B |
| | Macro | 2--10 | High | 20 | C |
| | Meso | 0.5--2 | Moderate | 45 | D |
| | Micro | <0.5 | Low | 80 | E |
| Vuggy | Mega | >10 | Extremely high | 0 | B |
| | Macro | 2--10 | High | 0-10 | B-C |
| | Meso | 0.5--2 | Moderate | 10--20 | C-D |
| | Micro | <0.5 | Low | 20--60 | D |
| Fractures | Mega | >10 | Extremely high | 0 | A |
| | Macro | 2--10 | High | 0-10 | A-B |
| | Meso | 0.5--2 | Moderate | 10--20 | B-C |
| | Micro | <0.5 | Low | >20 | D-E |

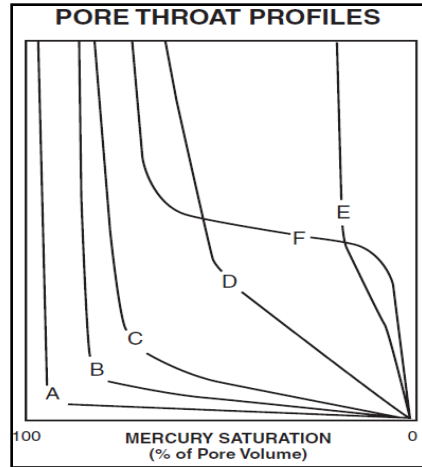


Figure 2.5: Typical petrophysical parameters based on pore geometry (Beaumont and Foster 1995).

2.9 Valvatne's Pore Network Model

In addition to the investigated capillary pressure models and correlations, pore network modeling is also researched in this thesis. Although many pore scale simulators have been suggested, the pore scale simulator developed by Valvatne (2001) is used in our study. His work consisted on network modeling at the microscopic scale where void pore space is represented by a lattice of pores connected by throats. The simulator can be used to investigate capillary pressure and relative permeability profiles at different conditions using available experimental data. The simulator takes input data obtained from thin sections and core measurements, pore size distribution, pore type, aspect ratio, in order to calibrate a single network to specific core conditions. Once the calibration is performed properties at different conditions can be evaluated.

2.10 Summary

Several methods that evaluate capillary pressure are reviewed. It is observed that all these methods regardless of their form have a root or relationship to the average pore radius, $r_p = \sqrt{\frac{8k}{\phi}}$,

derived by Leverett (1939). Closer inspection of the models evidence that the average pore radius is always included either implicitly or explicitly in the different formulations. Thomeer, Brooks and Corey and the lambda models include the average pore radius implicitly by means of variables like the geometric factor, threshold pressure and lambda. The Picket, Wells, Swanson and r_{p35} correlations contain the average pore radius in explicit form.

Another interesting observation is that the various formulations attempt to model pore systems using predictive relationships to petrophysical properties, yet none provides an explicit variable that accounts for a mixed pore system or a multimodal pore distribution.

CHAPTER 3

CAPILLARY PRESSURE EVALUATION USING PORE SCALE MODELING

Measurements to obtain capillary pressure curves to evaluate field fluid distribution are typically scarce and limited. Core measurements often times disregard the effect of pore geometry features like vugs or big scale fractures occurring at the log and field scale. This is particularly true for naturally fractured reservoirs such as Field M. The core measurements performed for Field M only test matrix properties and disregard the effect of big scale fractures. Moreover, core measurements for the field of study possess a high degree of uncertainty due to the sample brittleness and the likelihood of affecting the state of the microfractures in the matrix. The apertures of the microfractures might be enhanced due to pressure release as the samples are brought to surface or reduced when placed on core holders to perform experiments.

3.1 Pore Scale Model - Valvatne (2004)

Pore scale modeling (PSM) is an additional tool to evaluate complex petrophysical properties, capillary pressure and relative permeability for rock samples with different configurations which make core experimentation ineffective. In this study, PSM is used to investigate some of the issues previously discussed. The PSM simulator used in this study was developed as part of a doctoral dissertation at the Imperial College (Valvatne, 2004). In this simulator the void space is a network represented by a lattice of pores connected by throats (Figure 3.1). The program has been developed to simulate two-phase capillary dominated flow assuming a quasi-static condition network. This means all interfaces are kept constant, and there is a single displacement event. As the non-wetting phase pressure increases and the wetting

phase is kept constant, the network elements are filled in order of increasing capillary entry pressure. This ensures the fluid filling rank of order is the same as the pore and pore throat size distributions (Valvatne, 2004).

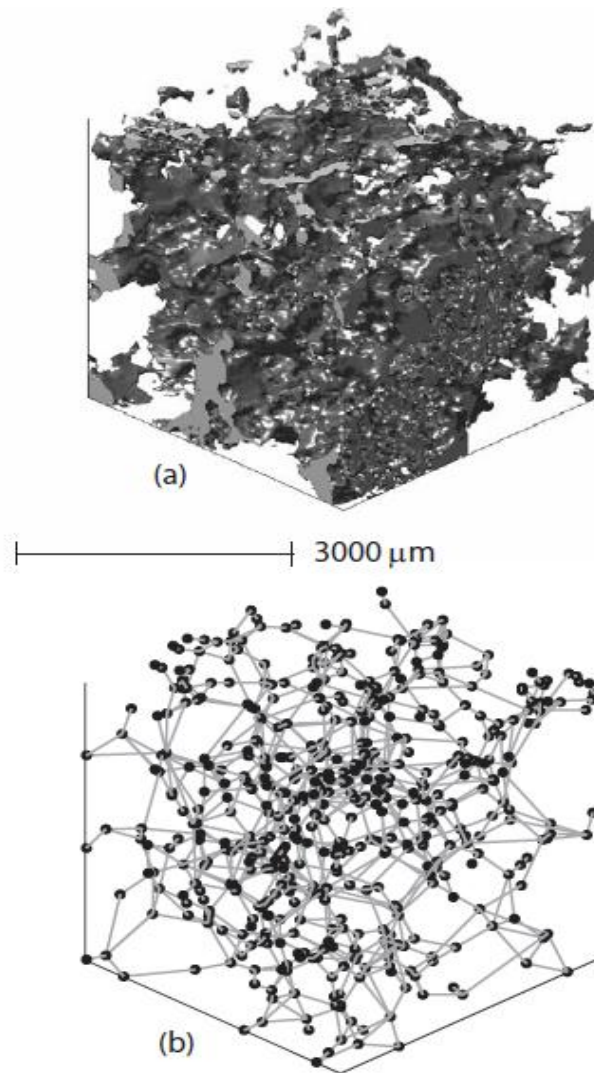


Figure 3.1: (a) 3D voxel image for the Berea sandstone (b) Network of pores and throats extracted from the 3D voxel of the Berea sandstone (Valvatne, 2004).

Networks of pores connected by throats (Figure 3.1.b) that represent the rock geometry statistics and pore space are generated using 3D images from micro CT tomography (Figure 3.1.a). A robust prediction requires a network representative of a rock sample, however

generating networks is costly and time consuming. An alternative approach is to modify an existent network to best represent a rock sample.

Valvatne (2004) investigated various rock types. The rock that is best modified for this study is the Berea sandstone network. The Berea sandstone is a very permeable rock, however the network is modified to reflect permeability values found in the rock samples for this study (Section 3.3). Field M is a condensate quarzitic sandstone that in terms of wettability is defined as a strongly water wet system. Therefore, the water wet Berea sandstone network provided by Valvatne is selected. A network generator that uses statistical numerical reconstruction was also available, however this method is not feasible for the rock of this study. Field M rock samples show a bimodal pore throat distribution. The network generator fits the data to a skewed or normal Weibull distribution. A Weibull distribution is a continuous probability distribution first applied to describe particles size distribution. This distribution is fitted to data by modeling the shale and size parameters. This matter is discussed in more detail, in this chapter.

The Berea sandstone network is composed of 26,146 throats and 12,349 pores in a volume of 33mm^3 . Effective porosity is 18.3% and absolute permeability is 2.5 Darcies. Minimum and maximum pore throat and pore size radius are 3.6 and 73.5 microns for pores and 0.9 and 56.9 microns for throats. The coordination number, number of throats connected to a pore, ranges between 1 and 19 with an average of 4.19. The shape factor, the ratio of area over perimeter, is used to describe the pore irregularity. The variation in pore irregularity can be described by three geometries, circles, squares and triangles. The shape factor with the most irregularity is represented by triangles. The Berea sandstone network shape factor is represented in its majority by triangles. Only 1.2% of the elements are circular and 6.5% are squares.

PSM in this study is used to evaluate the quality of the available capillary pressure profiles. Additionally sensitivity cases are run to evaluate the effect of fracture density, connectivity, and pore throat size distribution.

3.2 Description of Core Data and Capillary Pressure from Core Measurements

From the five wells drilled on the target formation, only wells 2, 3, 4 and 5 have special core measurements. A total of 99 routine core measurements are available (Appendix B, Table B-1). A total of 19 core samples include capillary pressure profiles derived from mercury injection experiments, and 6 samples include relative permeability curves (Table 3.1).

Table 3.1: Petrophysical and Composition for Rock Samples with Special Core Analysis

| Core Ref.N ^o | Well | Grain Density | Porosity @ STD | Porosity @ NOBP | Air Permeability | Klinkenberg Corrected Permeability | Quartz | Clay | Others (Feldspars, Dolomites, Plagioclasts) | Predominant Type of Clay |
|-------------------------|-----------|--------------------|----------------|-----------------|------------------|------------------------------------|--------|------|---|--------------------------|
| | | gr/cm ³ | % | % | mD | mD | % | % | % | |
| 16 | Well 2 | 2.67 | 4.60 | 3.6 | 0.0012 | 0.0002 | 73.6 | 13.6 | 12.8 | Illite/Chlorite |
| 21 | Well 2 | 2.66 | 4.40 | 3.1 | 0.0015 | 0.0003 | | | | |
| 32 | Well 3 | 2.64 | 3.70 | 2.7 | 0.0024 | 0.0008 | | | | |
| 44 | Well 3 | 2.65 | 3.00 | 2.3 | - | 0.0009 | | | | |
| 52 | Well 3 | 2.73 | 2.40 | 1.8 | - | 0.0001 | | | | |
| 58 | Well 4 | 2.71 | 4.91 | - | 1.2379 | 0.4952 ^E | | | | |
| 62 | Well 4 | 2.71 | 5.31 | - | 0.0355 | 0.0142 ^E | | | | |
| 63 | Well 4 | 2.72 | 4.48 | - | 0.0234 | 0.0094 ^E | 66 | 15 | 19 | Illite/Chlorite |
| 66 | Well 4 | 2.70 | 4.03 | - | 35.4947 | 14.1979 ^E | | | | |
| 69 | Well 4 | 2.68 | 3.62 | - | 0.0109 | 0.0044 ^E | 78 | 7 | 15 | Illite/Chlorite |
| 72 | Well 4 | 2.70 | 2.63 | - | 0.0262 | 0.0105 ^E | | | | |
| 74 | Well 4 ST | 2.64 | 5.32 | - | 9.2255 | 3.6902 ^E | 89 | 2 | 9 | Illite |
| 77 | Well 4 ST | 2.63 | 3.97 | - | 0.0274 | 0.0109 ^E | 87 | 2 | 11 | Illite |
| 82 | Well 4 ST | 2.65 | 4.73 | - | 0.9223 | 0.3689 ^E | 87 | 2 | 11 | Illite |
| 85 | Well 5 | 2.67 | 4.31 | 3.8091 | 0.0023 | 0.0009 ^E | | | | |
| 86 | Well 5 | 2.66 | 3.99 | 3.1192 | 0.0037 | 0.0015 ^E | | | | |
| 87 | Well 5 | 2.66 | 3.27 | 2.7790 | 0.0102 | 0.0041 ^E | 84 | 2 | 12 | Illite/Chlorite |
| 88 | Well 5 | 2.65 | 3.39 | 2.9878 | 0.0007 | 0.0003 ^E | | | | |
| 90 | Well 5 | 2.67 | 3.94 | 3.5083 | 0.0007 | 0.0003 ^E | 86 | 2 | 12 | Illite/Chlorite |

As mentioned before one of the main uncertainties associated with core measurements in tight rocks is the varying matrix microfractures apertures during rock sampling. Core reports for Field M state difficulty to discriminate induced fractures from natural fractures in core samples. In that sense, a reference scale to classify microfractures occurring in the matrix and larger fractures is established. The reference scale is based on: the pore throat radius at 35% mercury saturation (r_{p35}) values reported in Table 2.1, the values reported by Inigo (2009), and the permeability model established by Repsol. To set a framework of values facilitates to analyze the correlation between pore throat radius (r_{p35}), permeability, water saturation and capillary pressure profiles.

The permeability model established by Repsol has three components: macrofractures with high permeability and low storability, low conductivity fractures (LCF) with low permeability and low storability and matrix with low permeability and high storability. The second and third column in Table 3.2 summarizes the porosity and permeability values associated with these components. The values of r_{p35} in Table 3.2 fourth column are obtained from combining values from Table 2.1 and values reported by Inigo (2009) for microfractures apertures. In this work fracture apertures are equivalent to pore throat diameter.

Table 3.2: Petrophysical Parameters Based on Pore Geometry for Field M

| Porosity Components | Porosity | Permeability | Pore Throat Radius |
|--|----------|--------------|--------------------|
| | % | mD | Microns |
| Matrix (Microf. , Diss., Interg. and Fractured Shale) | 3--7 | 0.0003-0.2 | <6 |
| Low Conductivity Fractures (LCD) | 0.2--1 | 12.5-18 | 6--10 |
| Macrofractures | 0.2--1.6 | 2000-7000 | >10 |

Inigo (2009) analyzed a number of core samples corresponding to formation H and reported microfractures apertures up to a threshold value of 0.015 mm (15 microns or r_{p35} equal to 7.5 microns). A semi-log plot of permeability and porosity with varying curves generated with Aguilera (2002) r_{p35} correlation is used as a diagnostic plot for the core measurements. Figure 3.2 shows the core samples porosity and permeability values fall between 0.05 and 6 microns r_{p35} . The diagnostic plot confirms that in Field M permeability varies with r_{p35} and it is independent of porosity. In the diagnostic plot the squares represent the cores samples with special core measurements. Fracture r_{p35} from FMI interpretation vary from 1 to 100 microns with a mode value of 8 to 10 microns. It is arguably that medium fractures, low conductivity fractures, might be present in the matrix, but this work assumes the rock matrix contains only microfractures.

Furthermore capillary pressure values are converted to reservoir conditions and to a water-gas system using Equation 3.1:

$$P_{c(res)} = P_{c(lab)} \left[\frac{(\sigma \cos \theta)_{(res)}}{(\sigma \cos \theta)_{(lab)}} \right] \quad (3.1)$$

Where:

P_c = capillary pressure at reservoir and laboratory conditions (psia),

$\cos \theta$ = angle of contact (degrees)

$\sigma_{(res,lab)}$ = interfacial tension at reservoir and laboratory conditions (dynes/cm²)

From this equation the conversion factor resulted in 0.1343, assuming $\left[\frac{(70 \cos 0)_{(air-water)}}{(485 \cos 140)_{(air-Hg)}} \right]$ to change the fluid system and $\left[\frac{(50 \cos 0)_{(res)}}{(70 \cos 0)_{(lab)}} \right]$ to convert pressure values from laboratory to reservoir conditions.

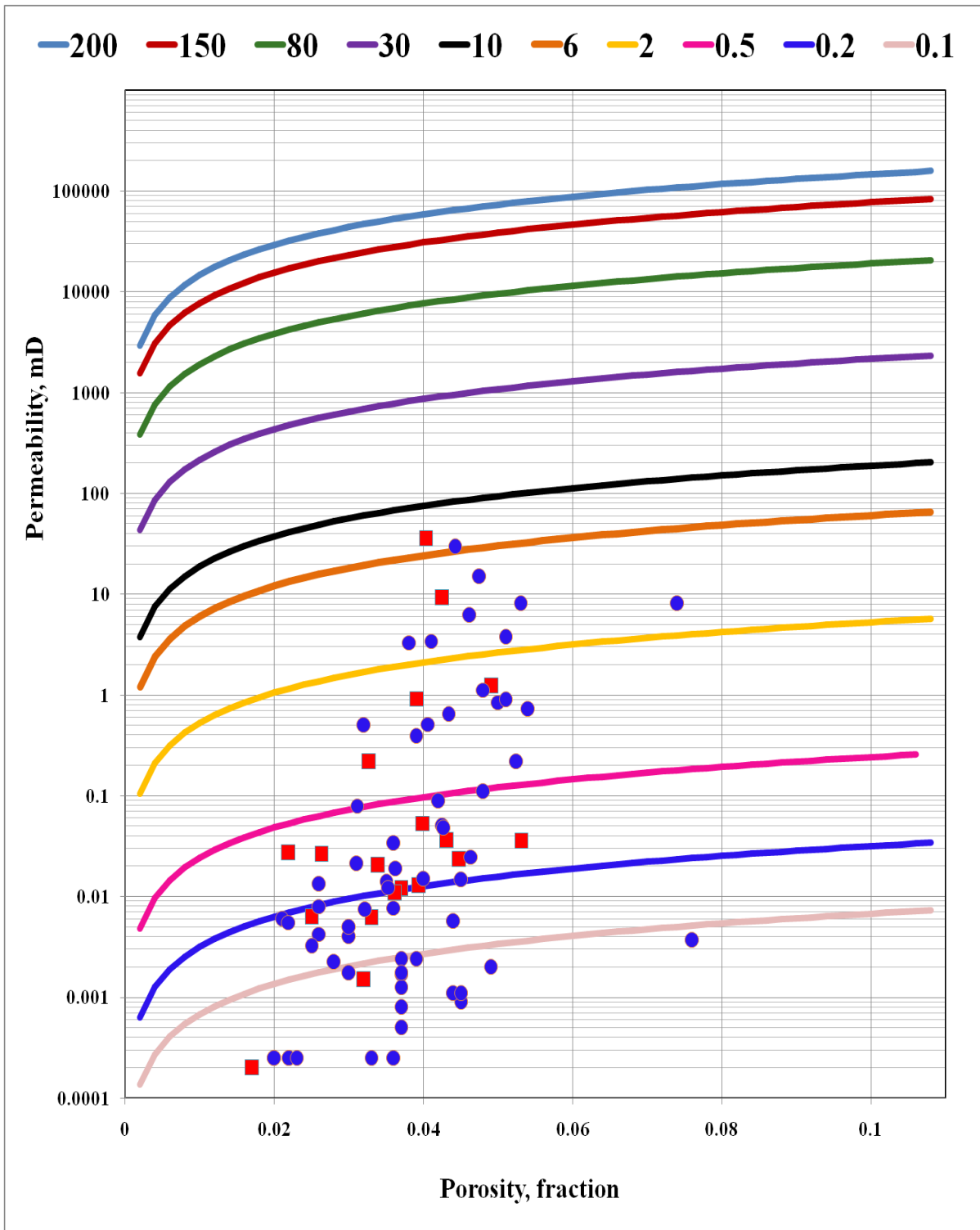


Figure 3.2: r_{p35} Diagnostic plot used to establish pore throat radius size range for microfractures. Solid lines represent a constant r_{p35} value in microns.

Figure 3.3 is a semi-log plot of all the available capillary pressure curves and corresponding saturations. Features like irreducible water saturation, pore throat size distribution, displacement (P_d) and entry pressure (P_e) can be interpreted from this figure. The water saturation scale in Wells 2 and 3 (Sample Ref#16, 21, 32, 44 and 52) seem to have been normalized to 0% water saturation, so irreducible water saturation cannot be determined. The capillary pressure profiles for Wells 4 and 5 stop before reaching 50% water saturation,. However assuming the curves follow the same pattern, dotted lines in Figure 3.3, irreducible water saturation values of 7% and 35% for wells 4 and 5 are inferred. An irreducible water saturation of 35% from NMR in a pilot well was determined (Repsol, 2006). Possibly capillary pressure curves for Wells 4 and 5 are incomplete because of an abrupt drop in capillary pressure indicating an increase in connectivity, and/or a change in the pore geometry, so experiments stopped before affecting original rock conditions. The core experiment protocols were not available to review, however looking at the curves the determination of irreducible water saturation using capillary pressure is not feasible. Sample Ref#66 is considered an outlier, because of the extremely high permeability value.

In Figure 3.3 it can be observed that entry pressures vary from 2 psi to 60 psi. Additionally the displacement pressure, pressure at the approximate plateau of the curve where fluid is a continuous filament inside the pores, varies from 10 psi to 100 psi. Observing the capillary pressure curvatures in Figure 3.3, a flat plateau indicates good pore throat size sorting while a steeper profile indicates poor pore throat sorting. It is also observed the curves fall towards the smaller range of pore throat sizes more evident in Figure 3.4.

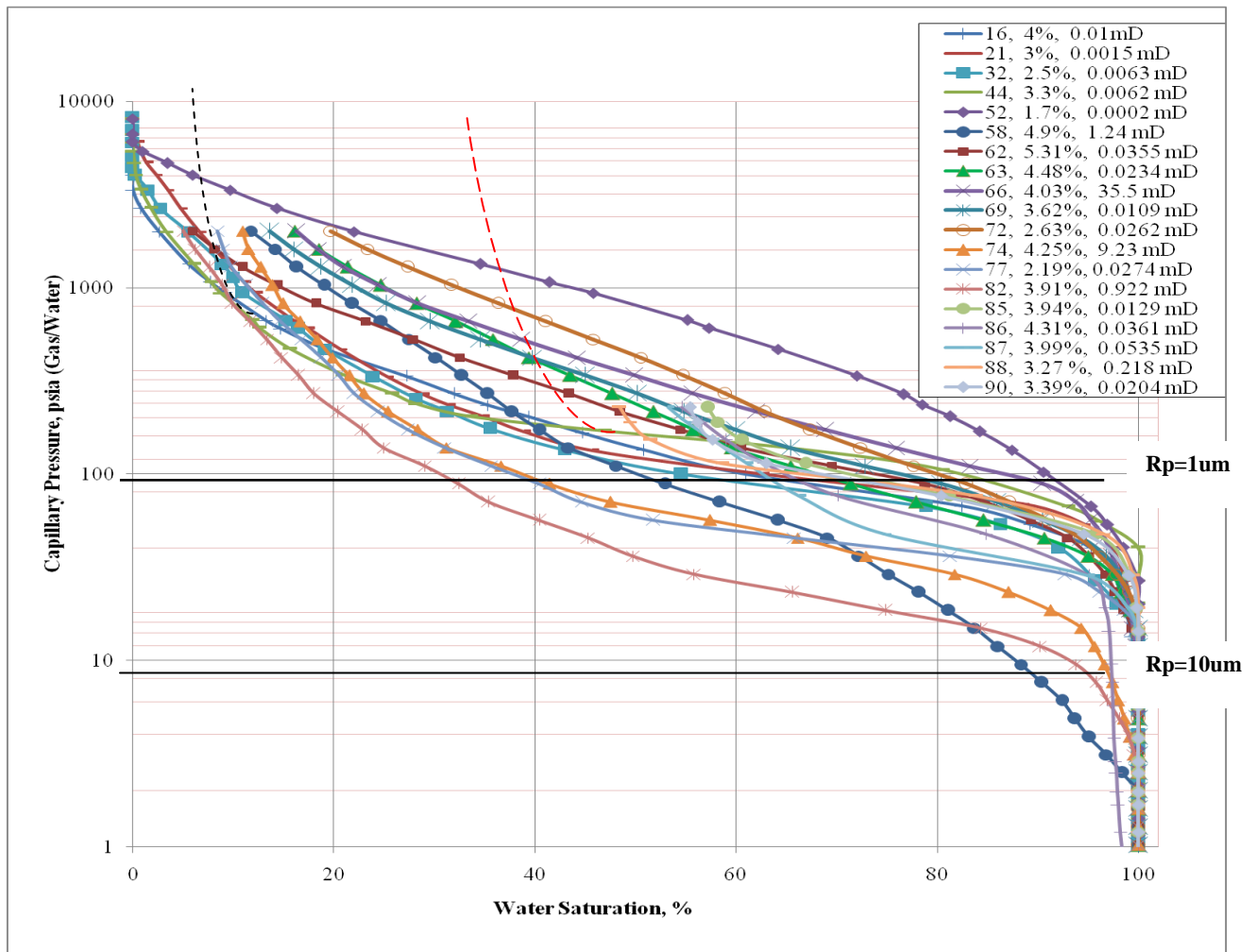


Figure 3.3: Available mercury injection capillary pressure curves semi-log plot used to diagnostic the dataset.

Figure 3.4 is a semi-log plot of incremental mercury volume and pore throat radius used to determine the critical pore throat radius. The critical pore throat radius is the pore throat radius at 35% mercury saturation, the majority of used to determine P_d . In the figure two zones are identified. Zone A delineate the range of pore throat radius sizes for rock with high clay content (Table 3.1). Zone B indicates the limits for cleaner samples. Notice that the samples with high clay content show a bimodal distribution and the cleaner samples have a distribution closer to normal distribution.

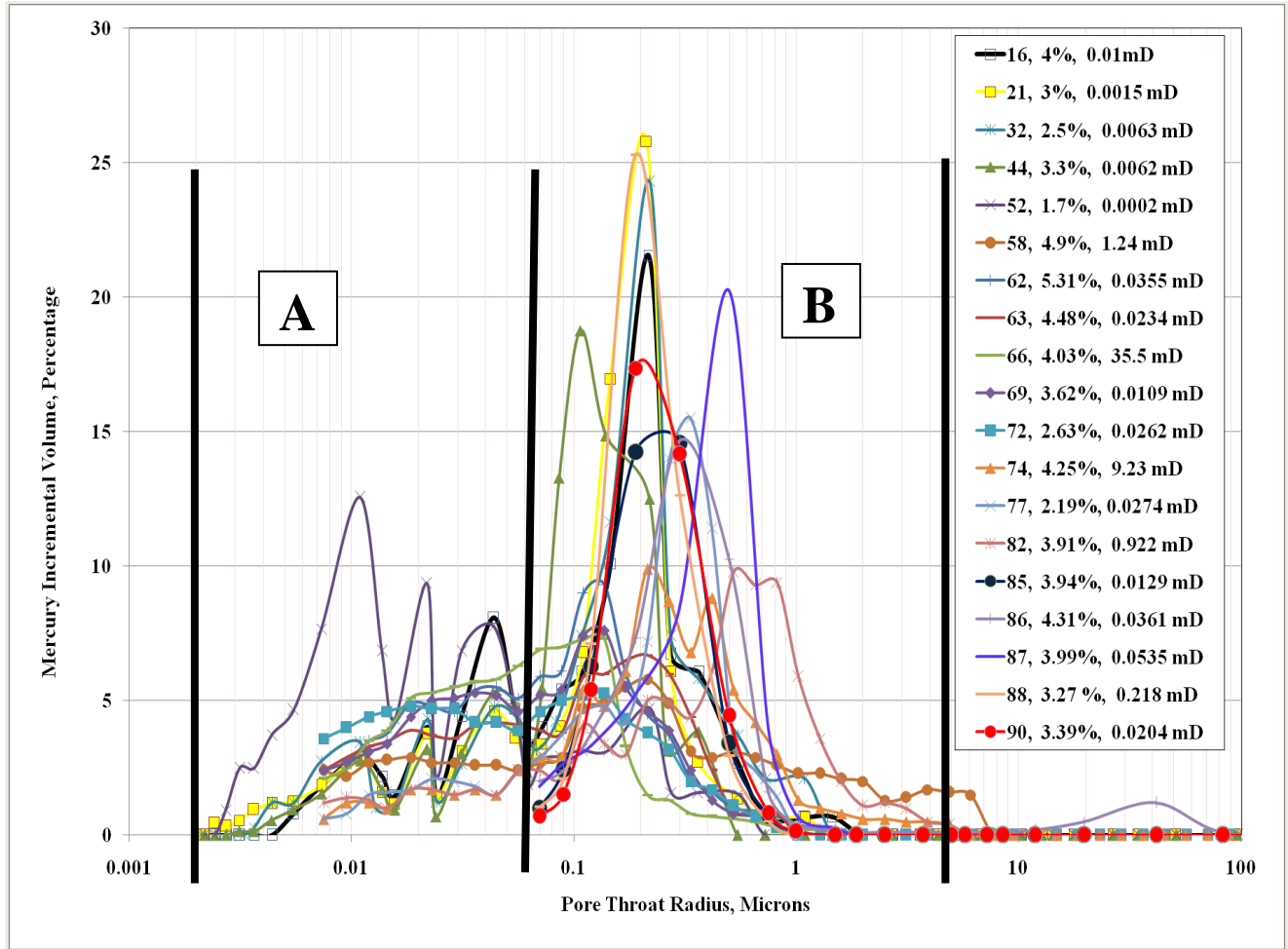


Figure 3.4: Semi-log plot of incremental mercury injection capillary pressure curves used to diagnostic the dataset.

From the 19 capillary pressure curves, 10 were selected to perform simulations. The samples were selected because they are representative of the other samples or because they show a different behavior. The selected samples are: 16, 44, 52, 58, 69, 66, 74, 82, 87, and 88. Considering a strongly water wet system, near constant wettability, mercury capillary pressure curves seem consistent with the variation in pore throat size linked to geology. Histograms of the pore throat radius for these 10 samples are presented in Appendix B, Figures B-7 to B-15. Examining the histograms, Well 2 has a bimodal pore throat radius distribution which becomes

less obvious moving towards Well 5. Wells 4 and 5 showed a pore throat size distribution skewed to the bigger size. This confirms the observations made from Figure 3.4.

3.3 Pore Scale Modeling Matching Core Measurements

The Berea sandstone network is modified to represent the pore system, microfractures, found in Field M. This in turn changes the permeability of the Berea sandstone to approximate Field M characteristics. The controlling parameters to modify the network are: pore shape, aspect ratio, pores and pore throats distribution, shape factor, coordination number and porosity. The Berea sandstone has over 90% of the pores represented by triangles. Triangles are the geometry used to represent more irregularity in the pores, so this parameter is not directly modified. The triangles size is adjusted by the pore throat size radius distribution input of the simulation. To resemble microfractures the pore radius is set to be equal to the pore throat radius, so the aspect ratio is 1. The pore throats then are modeled as narrow channels with triangular cross-section. The porosity of the Berea sandstone is 18.3%, which is modified to match each core sample porosity. The coordination number, number of throats connected to a pore, which affects connectivity is limited to the Berea sandstone average value, 4.09. The coordination number can be reduced but not be above the average value limiting this aspect on the simulation process. In this work, the main parameters to modify for the simulations are pore throat radius distribution from mercury injection experiments with corresponding saturations and the core sample porosity.

Sample Ref #16 from Well 2 is used to discuss the results of the simulation work. First the results from using a pore throat size distribution generated using a Weibull distribution is presented. Then the simulation results using the pore throat size distribution from mercury

injection experiments are presented. Plots for the simulation results using the mercury injection data of the remaining nine core samples can be found in Appendix C.

Figure 3.5 shows the simulated capillary pressure using a Weibull pore throat size distribution. The modeled and experimental capillary pressure show different shape and value ranges. The big gap between the solid line and circles in Figure 3.5 is a result of the different pore throat distribution.

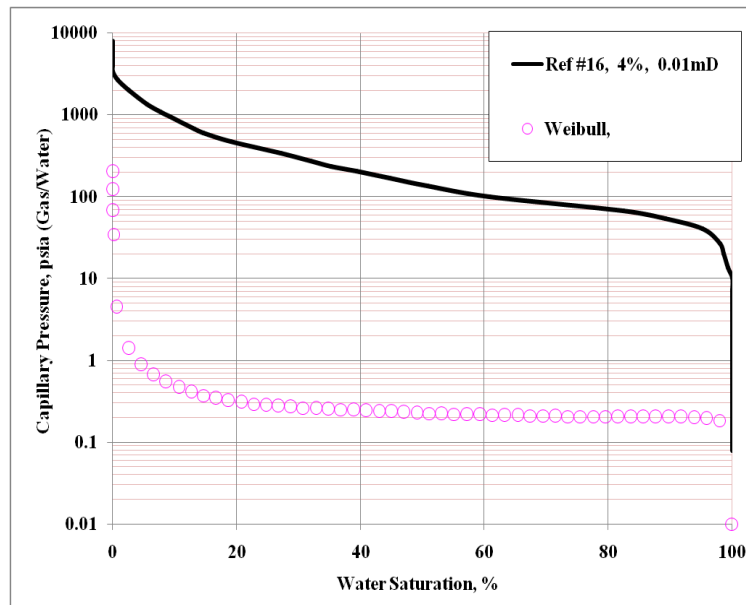


Figure 3.5: Well 2 sample Ref#16 capillary pressure match of experimental data to a pore throat distribution generated using a Weibull distribution.

Although Figure 3.6 does not show an extreme difference between the pore throat size distributions, the difference is evident when histograms are compared (Figures 3.7 and 3.8). The Weibull distribution requires the estimation of two fitting parameters from experimental data. Figure 3.7 shows the resultant histogram from fitting experimental data to a Weibull distribution.

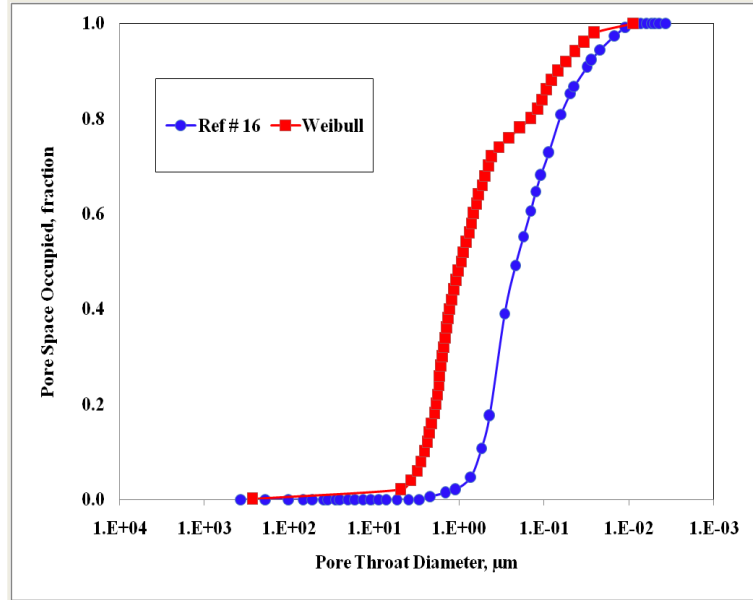


Figure 3.6: Well 2 Sample Ref #16 comparison of original and iterated pore throat size distribution.

Comparing Figure 3.7 and 3.8 it is observed that the pore throat size distribution obtained using a Weibull distribution does not represent the core data. The core data shows a bimodal normal distribution as discussed before in Figure 3.4, whereas the Weibull distribution shows a lognormal skewed distribution. The capillary pressure results from Figure 3.5 confirm that the use of a Weibull distribution is not a good fit to generate a pore network to model Field M pore throat distributions. Thus generating a network using statistical methods introduces more uncertainties than modifying a network with known properties to approximate the characteristics of the reservoir rock.

The results demonstrate the strong effect of the pore throat size distribution and the effect of using a non-representative distribution. This is particularly interesting because the majority of the capillary pressure correlations are based on unimodal pore throat distributions. From hereafter all simulations are performed using mercury injection pore throat distribution as input to the modified Berea sandstone network.

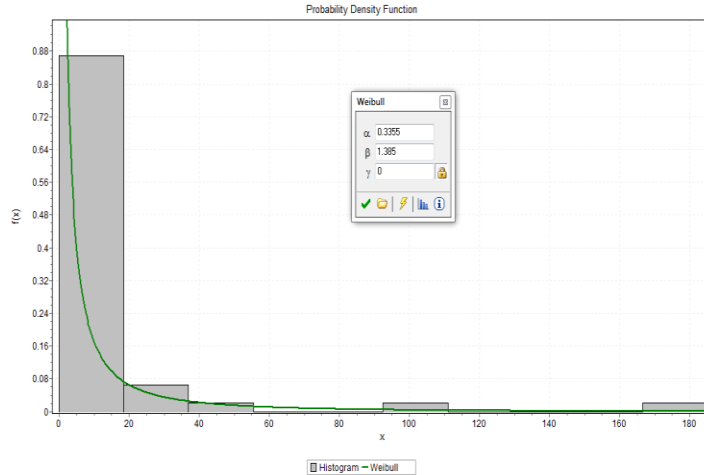


Figure 3.7: Data fitting to determine Weibull distribution parameters generated using Easyfit 5.5 statistical software.

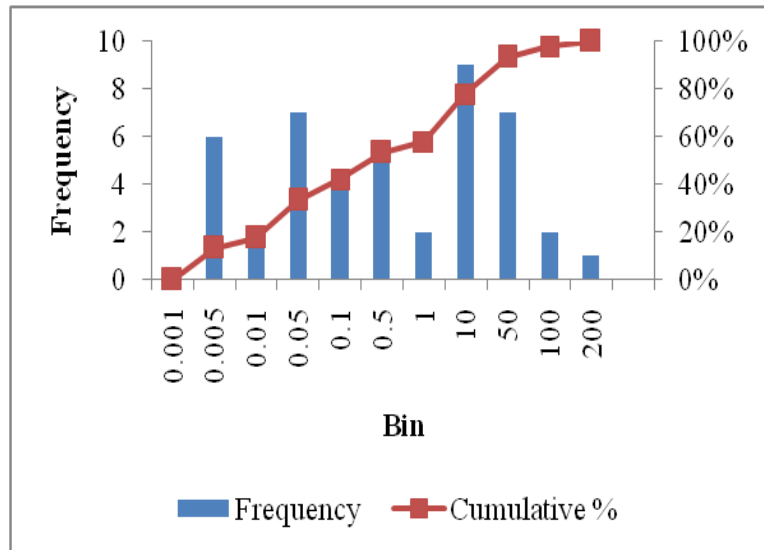


Figure 3.8: Well 2 sample Ref #16 histogram of the pore throat radius distribution, bin is in microns.

The line with squares in Figure 3.9 shows the first simulation run using the mercury pore throat size distribution as input. The experimental and simulated capillary pressures curves match in shape but not in values. The experimental pore throat radius size distribution is manually modified iteratively until a match of capillary pressure curves is achieved (Figure 3.10). The iterated pore throat size diameter distribution shifted to the left from the original distribution representing bigger pore throat sizes than the experimental values.

The experimental pore throat size is calculated using Washburn (1921) Equation 2.3, which might be too simplistic hence the need to adjust the pore throat size distribution (Valvatne, 2004). Another reason to adjust the pore throat size is that the sample might have a higher coordination number than the Berea sandstone. The coordination number is limited to the 4.09 average value from the original Berea sandstone network, so pore throat size is increased instead. The permeability for the simulated and the experimental sample are 1.63 mD and 0.01 mD, respectively. The difference in permeability values indicate that connectivity in the rock has increased after mercury injection, perhaps from opening some filled fractures. This indicates that a core with this type of capillary pressure has a higher permeability value than the permeability recorded from helium injection core experiments.

Analyzing the pore throat distribution moving from Well 1 to Well 5, it is observed that the gap between the iterated and the original pore throat size increases. This indicates that as the clay content decreases the rock samples are more brittle, so it is expected a higher connectivity hence a higher permeability than the permeability from helium injection. This could imply that as the gap between the first simulation, line with squares, and the simulation with adjusted pore throats, line with circles, the uncertainty in the measurements increases.

Relative permeability curves are generated using the calibrated network from matching the simulated and experimental capillary pressure. From the 10 cores selected to run simulations only 3 samples, sample Ref# 66, 69, and 87, have experimental relative permeability curve. Figure 3.11 shows the best match, sample Ref#69, between simulated and experimental relative permeability curves. The match for samples Ref# 66 and 87 are not as good specially for the gas relative permeability curve. Sample Ref#69 relative permeability measurements show an irreducible water saturation of 69%. The simulated curve shows the same approximated value. In

general, simulated water relative permeability curve seems consistent to represent a water wet system. The gas relative permeability curve shows more variation and mismatch to core data.

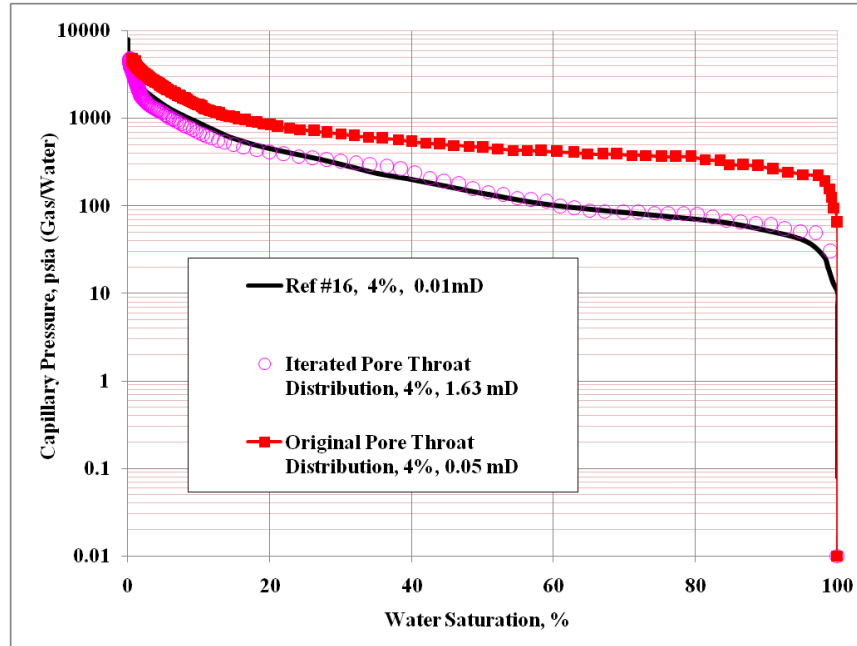


Figure 3.9: Well 2 Sample Ref #16 results of capillary pressure curves match.

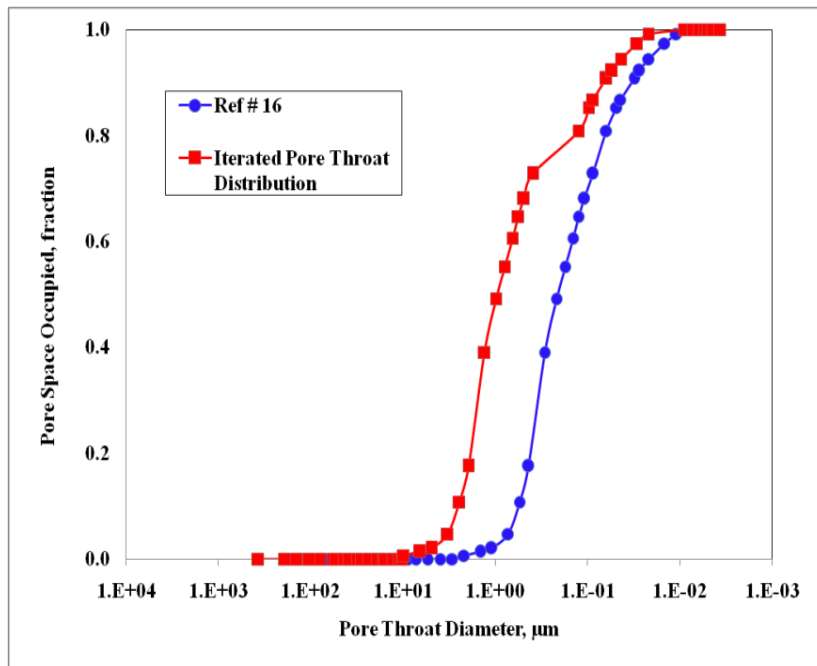


Figure 3.10: Well 2 Sample Ref #16 comparison between original and iterated pore throat diameter size distribution.

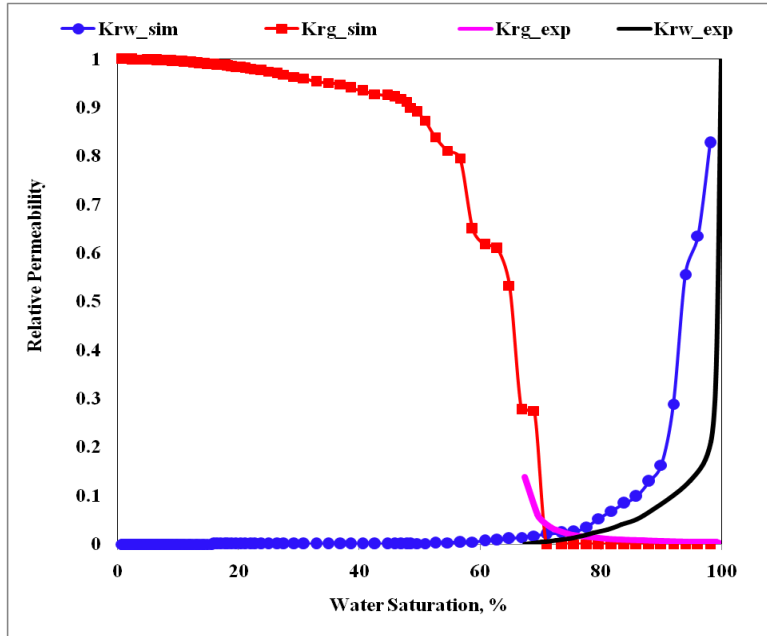


Figure 3.11: Well 4 Sample Ref #69 simulated relative permeability curves from capillary pressure calibrated network.

3.4 Pore Scale Modeling and Effect of Fracture Aperture and Density

Sensitivities on capillary pressure profiles are run to investigate the effect of varying parameters. Sample Ref #16 is the reference sample to run the sensitivities. The modified parameters are pore throat size distribution and the coordination number. These two parameters are analytically viewed as fracture aperture and density. The pore throat size distribution from sample Ref#16 is modified to represent a matrix predominant and fracture predominant sample. The coordination number reduces by removing throats randomly.

The four case scenarios are:

1. matrix predominant pore throat size distribution, coordination number equal to 2,
2. matrix predominant pore throat size distribution, coordination number equal to 4,
3. fracture predominant pore throat size distribution, coordination number equal to 2,

4. fracture predominant pore throat size distribution, coordination number equal to 4.

Figure 3.12 shows the simulated capillary pressures for the four case scenarios described above. As expected Case 1 and 2, matrix predominant, have higher capillary pressure levels than the fracture dominant cases. When the coordination number is reduced, the capillary pressure is higher as demonstrated in Case 1 and 2. On the other hand permeability increases as the coordination number and the fracture presence increases. Also observe that in Cases 1 and 3 where the coordination number is set to two, the capillary pressure curves stop at around 20% water saturation. The results of these four scenarios demonstrate the effect of pore throat size distribution from matrix to fracture predominant and the connectivity have a big effect on capillary pressure values in the order of one or two magnitudes.

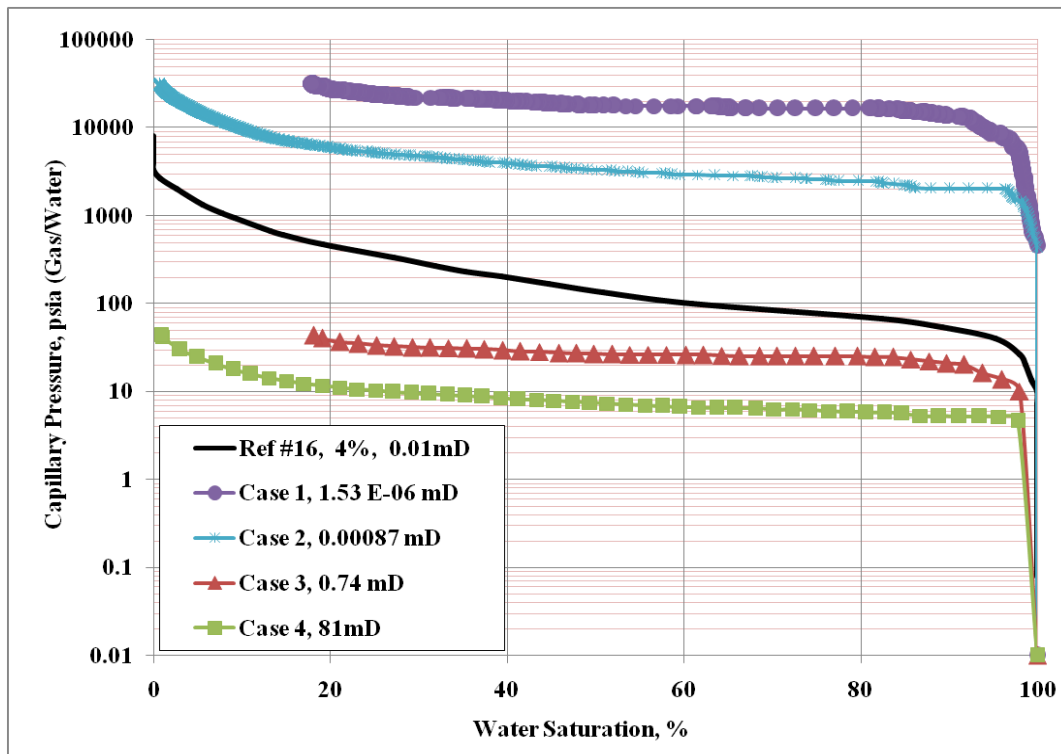


Figure 3.12: Summary plot showing the effect of varying pore throat size distribution and coordination number in the capillary pressure profile. Curve for sample Ref#16 is showed for reference.

Figure 3.13 shows the relative permeability curves for the four case scenarios. For reference, we include forty five degree lines are included in the figure that represent relative permeability curves inside a fracture. The curves for Case 1 and Case 3 both with a low coordination number overlap each other. This indicates that the increase in connectivity represented by the coordination number is a predominant parameter for simulating relative permeability curves.

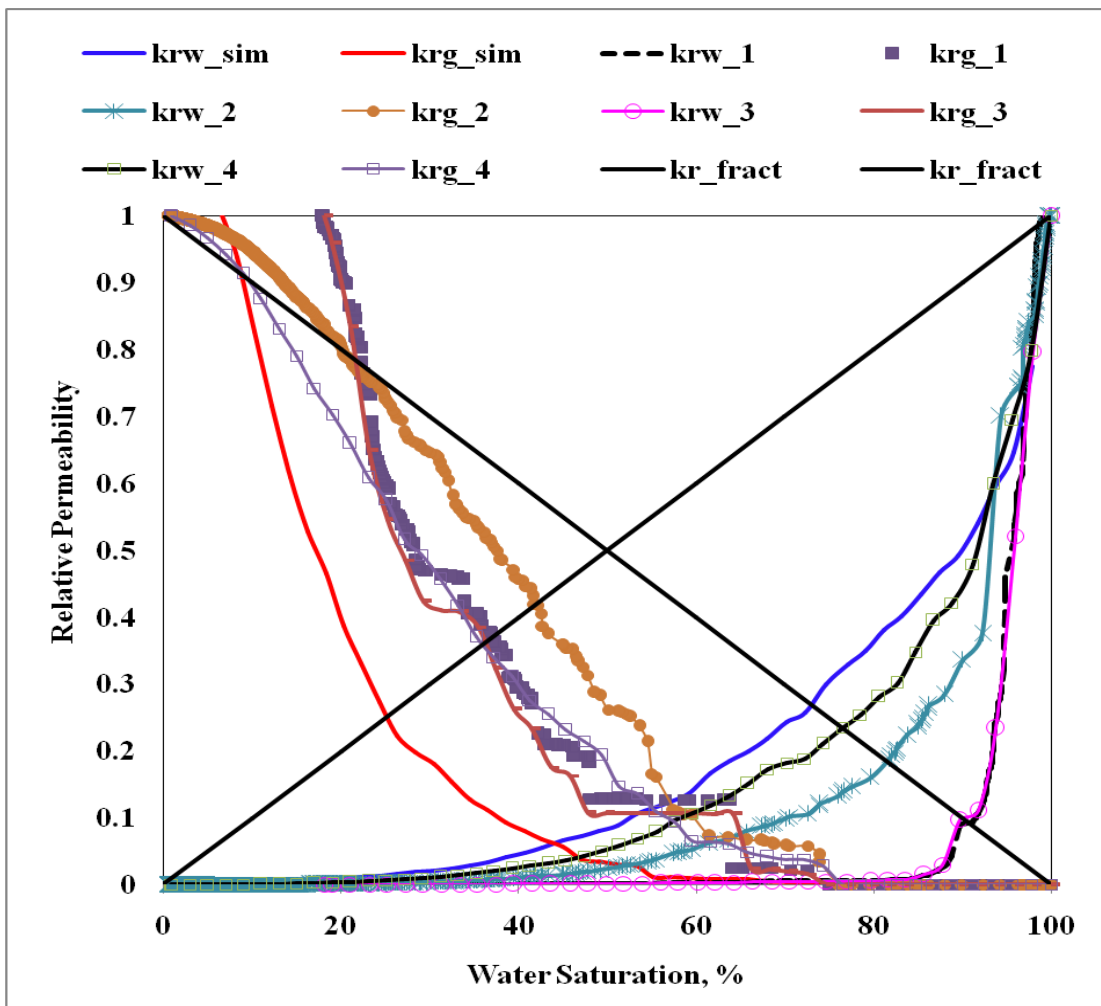


Figure 3.13: Summary plot showing the effect of varying pore throat size distribution and coordination number in relative permeability curves. Curve for sample Ref#16 with data series name krw_sim and krg_sim is showed for reference.

3.5 Summary

In this chapter pore scale simulation is used to investigate core measurements and the uncertainty associated to them. The simulation results indicate that the experimental and simulated curves capillary pressure curves are close to each other particularly for the less brittle rock samples. It was observed that as the sample become cleaner the gap between the first simulation and the experimental capillary pressure curves is greater. The permeability from the simulated matched capillary pressure is always higher than the permeability from core measurement using helium injection. The confidence on the simulation results could be improved by extracting a network of pores and throats from a Field M rock sample.

The simulation confirms that the dominant control for capillary pressure in Field M a water wet sandstone is the pore throat radius distribution. It was also seen that using a Weibull distribution to generate a pore throat size distribution is not suitable for the rock characteristics in Field M. If a normal distribution is used to model properties for a rock with a bimodal distribution might lead to significant errors in capillary pressure estimations. As observed in Figure 3.4 Field M rocks show a bimodal pore throat distribution.

The four case scenarios aided to investigate the effects of varying fracture density and pore throat size variation on the capillary pressure curves. Here the coordination number is used as an analogous to the fracture density. The results showed that the capillary pressure values vary one to two orders of magnitudes to the base case. An increase in coordination number, connectivity, decreases the capillary pressure and viceversa. It is also observed that the predominant feature affecting relative permeability curves for the case scenarios is the coordination number.

CHAPTER 4

CAPILLARY PRESSURE EVALUATION AT THE LOG SCALE

In Chapter 2 the basic formulations of capillary pressure are reviewed. These formulations showed that capillary pressure can be expressed as either the relationship between fluid properties and pore throat radius (Equation 2.2) or the fluids pressure difference expressed in terms of density, and height above the free water level (Equation 2.1). This relationship between formulations is also known as the saturation height function (SHF). The SHF concept implies that from knowing the depth of the free water level the saturation profile above this point can be estimated using capillary pressure algorithms calibrated to core measurements.

Because core capillary pressure measurements are scarce, it is a common practice to use few core measurements to generate a SHF that might not be representative of the different rock types present on an formation. In this chapter a new methodology to estimate water saturation profiles using the SHF concept is proposed. The methodology includes the definition of flow units to characterize capillary pressure profiles. This permits the selection of core capillary pressure measurements with rock properties that better represent the depth interval under investigation

The main objective of this chapter is to investigate a methodology to upscale core capillary measurements to the log scale. To validate results of the proposed methodology the resistivity log derived water saturation profiles and the SHF water saturation profiles are compared. Since the resistivity log derived water saturation profiles are used a petrophysical evaluation using log and core data is performed.

4.1 Formation Evaluation

The log evaluation for Field M is challenging. From Chapter 1, Field M formation can be described as a tight quartzitic sandstone with presence of laminated shale naturally fractured gas condensate reservoir with low salinity formation water. Table 4.1 shows a summary of the available logs for the five wells in Field M.

Table 4.1: Field M Available Log Curves

| Well 1 | Well 2 | Well 3 | Well 4 | Well 5 |
|---|--------|------------|--------|--------|
| AT90 | AT90 | AT90,60,30 | AT90 | HMIN |
| AT30 | AT60 | AO90,60,30 | | HMNO |
| | | AF90,60,30 | | |
| CALIPER | HCAL | CALIPER | HCAL | HCAL |
| DTCO | DTCO | DTCO | DTCO | |
| DTSM | DTSM | DTSM | DTSM | |
| GR | GR | GR | GR | GR |
| | | SGR | | |
| | | Uranium | | |
| | | Potassium | | |
| | | Thorium | | |
| RHOZ | RHOB | RHOB | RHOZ | RHOZ |
| TNPHI | TNPHI | NPOR | | NPOR |
| FMI | FMI | FMI | FMI | |
| PEF | PEF | | | PEF |
| AT=> Array Induction Two Foot Resistivity AF=> Array Induction Four Foot Resistivity AO=>Array Induction One Foot Resistivity HMNO=> Micro Normal Resistivity HMIN=> Microinverse Resistivity | | | | |

The brittleness of the rock in this area facilitates the occurrence of borehole breakouts, causing the bulk density log curve to be unreliable or unavailable in some wells. Another difficulty in the log analysis is to find methods that quantify the effect of shale, gas and fresh water on the log curves. The presence of gas decreases the neutron porosity and decreases the density porosity, however the effect of gas on density curves are of a lesser degree. Shale content increases the neutron porosity and depending on the shale density the density log might increase or decrease. The low salinity on the formation water masks the high resistivity values from

hydrocarbon content underestimating water saturation. The last is perhaps the biggest source of uncertainty affecting the water saturation estimation. Moreover Field M petrophysical evaluation core data should be used recognizing that the measurements correspond to the matrix rock properties and do not include the effect of fractures (macrofractures and low conductivity fractures Figures 1.4 and 1.5). The plots showing the results of the log evaluation are found in Appendix D.

4.1.1 Volume of Shale (Vsh)

Figure 4.1 shows the average mineral composition of the target formation for Field M from core XRD data (Appendix D). The classification others includes calcite and traces of pyrite and mica. The clay type in this reservoir is illite and chlorite. Mica appears as a trace in the XRD analysis, however the geological facies description highlights the presence of mica on Facies A. Core data indicates that mica presence is found in traces up to 6%. It is assumed that Mica affects significantly only in Facies A. Therefore, density logs in Facies A are evaluated cautiously. Spectral gamma ray from Well 3 shows that a uranium free gamma ray is close to the total gamma ray. This indicates that gamma ray logs in this formation is a direct response of shale and that mica does not affect this log significantly. The uranium curve from spectral gamma ray is flat which indicates that feldspar in this formation is not radioactive. (Repsol, 2008). Pyrite in this study is assumed to be an annular occurrence with no significance effect on logs.

Typically multi-mineral stochastic regression modeling is used to evaluate a complex lithology as the one found in Field M. This type of modeling is a multivariate regression based on the log response to the reservoir minerals and fluids, which could potentially overcome the

issues with the presence of shale affecting neutron and density logs and low salinity formation water affecting the resistivity response.

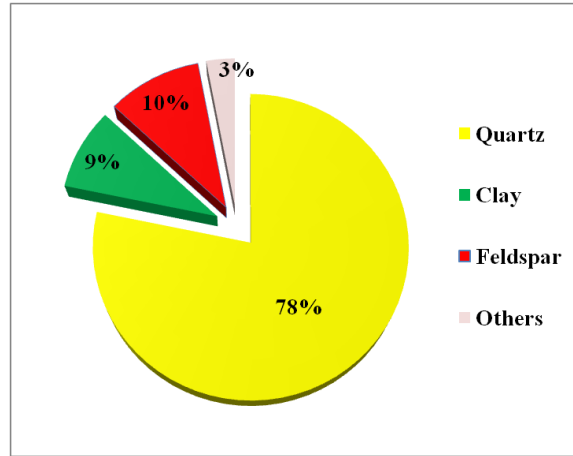


Figure 4.1: Average mineral composition for Field M target formation.

A full multi-mineral model is not feasible in Field M due to the borehole washouts affecting density logs which are the main foundation for this type of modeling. Nonetheless it was found that a simplified model using gamma ray, compressional and neutron logs as inputs yield good results to model shale volume. The simplified model targets to model quartz, illite, chlorite, water and effective porosity. Feldspar is included in the quartz volume because these minerals have similar composition. Similarly mica is considered a part of clay. A trend of decreasing quartz and increasing clay, feldspar and mica is observed. Figure 4.2 shows the results from using the simplified model. The modeled log curves are really close to the original logs. Similar results are obtained for all the wells. (Appendix D)

The volume of shale using other methods is estimated and compared to the modeled curves. A comparison between the Vsh using linear, Clarinov and multi-mineral modeling is shown in Figure 4.3. The linear correlation presents too high values of Vsh, while Clarinov values are high only in the shalier regions. Although the Clarinov correlation presents the best

match to the Vsh from XRD core data, the Vsh obtained from modeling correlates better with the lithology facies description. The final Vsh is an average value between the values from the multi-mineral modeling and Clarinov.

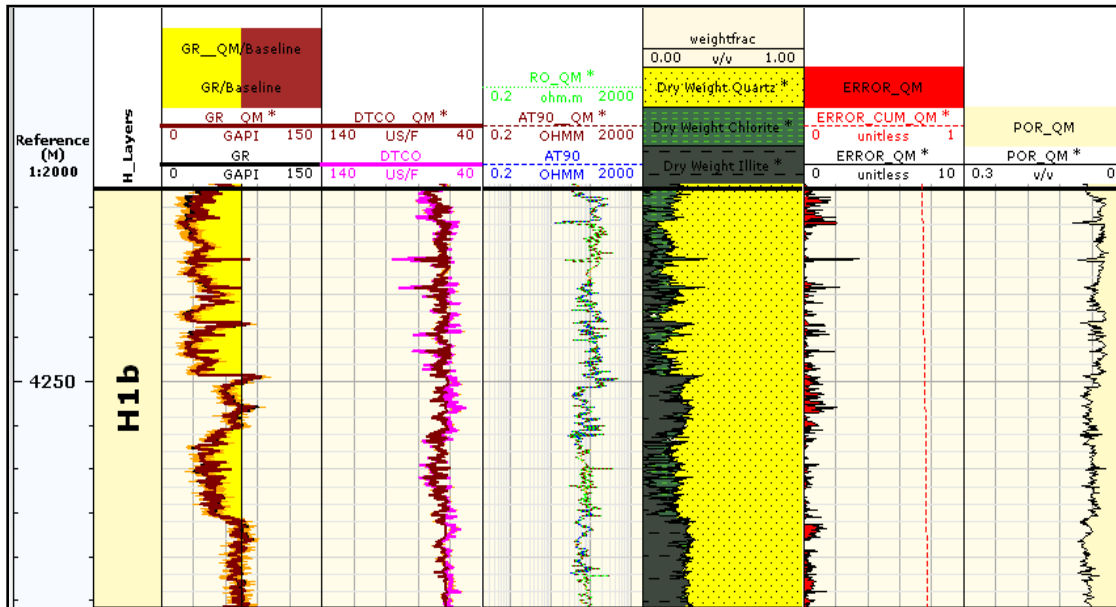


Figure 4.2: Log plot showing the results from the multi-mineral model to estimate simplified lithology track for Well 3.

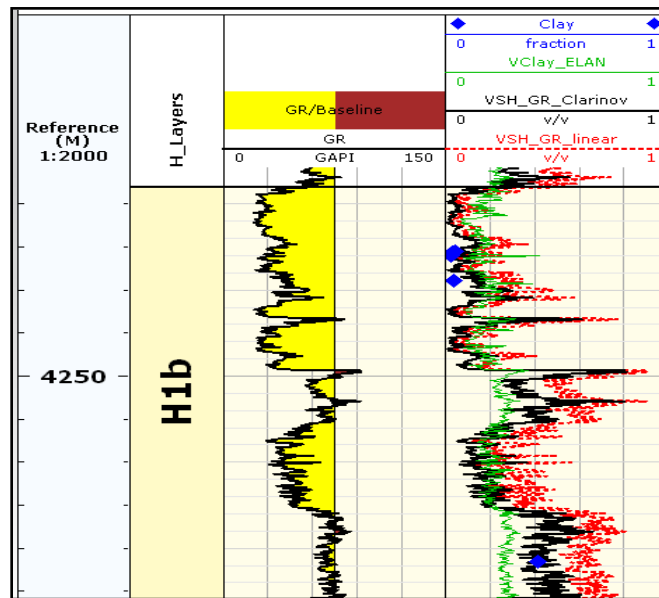


Figure 4.3: Log plot showing the results of Vsh estimation for Well 3.

4.1.2 Porosity

The porosity logs, neutron, density and sonic, are affected by the presence of shale, gas and microfractures. Porosity obtained from neutron and density logs are corrected for the presence of shale. Core or matrix porosity values range between 3% and 7% while fracture porosity is estimated to be below 1%. In this study the effective porosity is referred to as the Vsh corrected porosity. The terms effective and total porosity are interchangeable from here on. Figure 1.5 shows the porosity model adopted for Field M.

Figure 4.4 shows the results for porosity estimation. In the third track the comparison between corrected porosity and the porosity obtained from the multi-mineral modeling shows a good match. In the fifth track the porosity estimations are compared to the core porosity (Phi_2_final) values and a reasonable match is observed. Peaks on the neutron density derived porosity are due to washouts affecting bulk density. The minimum value between the neutron density corrected porosity and the multi-mineral modeled porosity is selected because these values match core data and facies description.

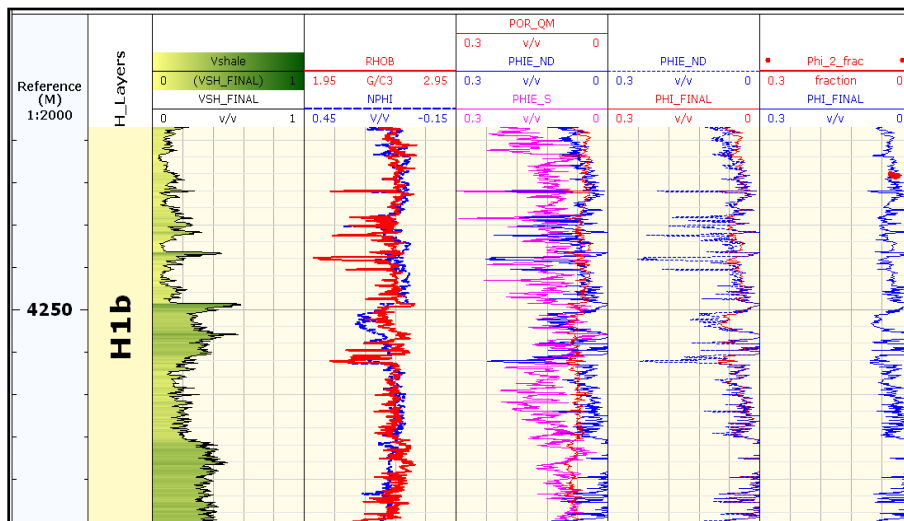


Figure 4.4: Log plot showing the results for effective porosity estimation for Well 3.

4.1.3 Water Saturation

The presence of laminated shale in Field M makes the Archie (1942) water saturation equation unsuitable to evaluate resistivity log derived water saturations. Equation 4.1, known as the Indonesian model, (Poupon and Leveaux, 1971) includes a correction term to Archie's equation to account for the effect of laminated shale. The Indonesian model is documented to be a suitable equation to evaluate laminated reservoirs, therefore it has been selected to evaluate Field M.

$$S_w = \left[\frac{\sqrt{\frac{1}{R_t}}}{\left(\frac{V_{sh}^{(1-V_{sh})/2}}{\sqrt{R_{sh}}} \right) \left(\frac{\sqrt{\phi_e^m}}{\sqrt{aR_w}} \right)} \right]^{2/n} \quad (4.1)$$

Where:

R_t =True formation resistivity,

R_{sh} =Resistivity of the nearest shale,

R_w = Water resistivity,

V_{sh} =Volume of shale,

ϕ_e =Effective porosity,

m =Cementation exponent,

n = Saturation exponent,

a = Tortuosity factor set equal to 1

Studies on an analogous field Aguarague located in Salta, Argentina, indicate that the salinity in Formation H increases with increasing water cut. This indicates that the initial water production is condensate water and not formation water. The formation water is reported to have

63,000 ppm of total dissolved solids. The water resistivity of the mixture of condensate and formation water for Formation H is 0.10 and 0.035 Ohm-m at surface and reservoir temperature, respectively (Aguilera et al., 2003c).

Due to the apparent low salinity water in the area, the estimation water resistivity (R_w) for Field M is complex. The average water resistivity from core measurements for Field M are 0.3 and 0.1 Ohm-m at surface and reservoir temperature, respectively. The formation water is reported to have 20,000 ppm of total dissolved solids compared to the analogous field, 63,000 ppm. This indicates the water samples in Field M could have been contaminated with condensate water reporting higher R_w values. It is also possible that the R_w has a high degree of variation due to the influx of fresh and salt water during deposition (Chapter 1).

For this reason various methods to estimate R_w are tested. The selected R_w value is obtained from calculating apparent R_w using Archie's water saturation equation on Well 2 proved water zone (Figure 4.5) with 100% water saturation. The obtained value is 0.07 Ohm-m at reservoir temperature. The R_w value is varied with temperature using Arp's equation (Asquith, et al., 2004). The resistivity readings on the target formation vary from 80 to 300 Ohm-m (Repsol, 2006).

The value of a is set to 1. Shale resistivity (R_{sh}) is obtained from examination of logs in shale zones and set to a value of 10 Ohm-m. The saturation exponent (n) from core experiments are abnormally low less than 1, resulting in very small values. Aguilera (1995) has observed that n values in naturally fractured reservoirs are close to the cementation exponent (m) values. Then, the n values in the present evaluation are set equal to m . Moreover, m values from core measurements only include the pore system found in the matrix and not the effect of big scale

fractures. In this line, a new cementation exponent model that includes the effect of the pore system from matrix and fractures is investigated and presented in the next section.

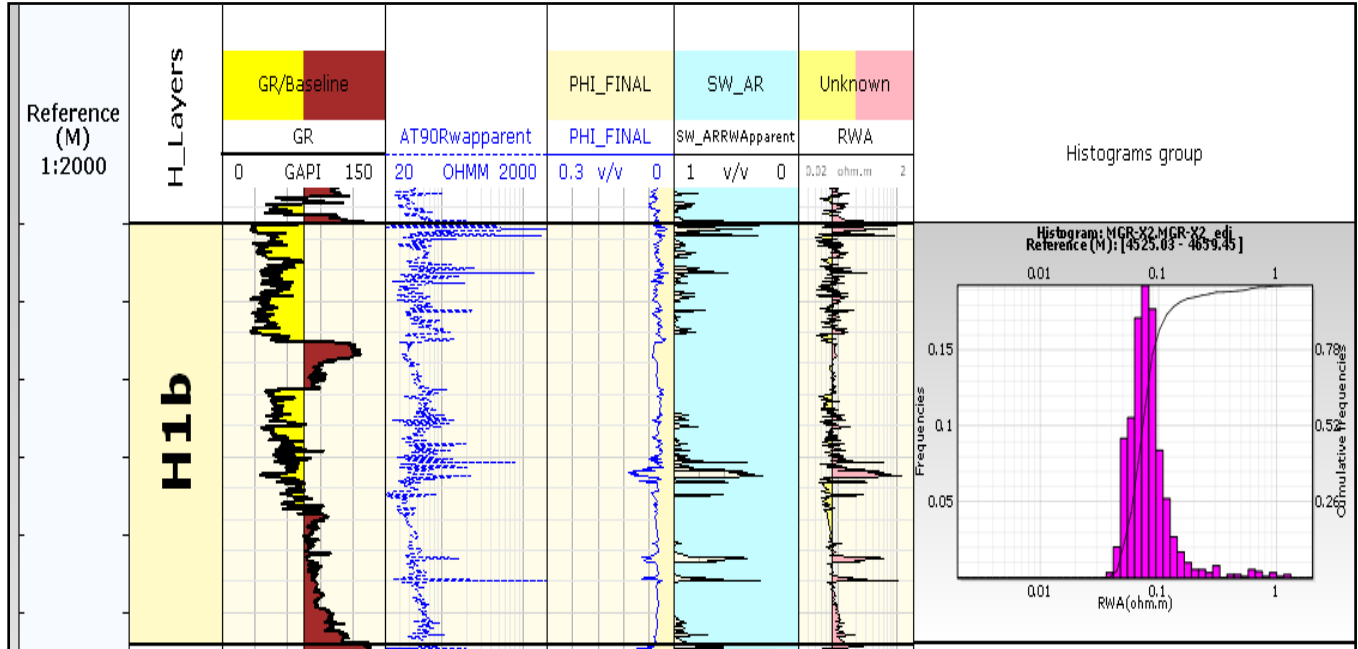


Figure 4.5: Log plot used to estimate R_w in a known water wet zone Well 2.

Development of a New Cementation Exponent Model (Sivila et al., 2011)

Aguilera et al., (2003, 2004) developed models to evaluate the cementation exponent for dual and triple porosity systems for various porosity configurations. The models are founded primarily on two studies: 1) Archie's (1942) relationship between formation resistivity factor and porosity of reservoir rocks filled with conductive fluid and 2) Towle's (1962) evaluation of the cementation exponent from Archie's equation where he tested the relationship between formation resistivity factor and porosity using different assumed pore geometries, and their effects on m . The pore geometries investigated by Towle are resultant from the approximation of intersecting tubes, intersecting planes and vugs. The study concluded that the cementation exponent is greatly affected by pore geometry and that m values increase with tortuosity.

The dual and triple porosity models are based on the theory that porosity components with some degree of connectivity should be modeled as a parallel resistance network while the unconnected pore space are a series of resistance networks. As a result, the variables included on the porosity model and the degree of connectivity among the components are key for the development of the cementation exponent. The high degree of fracturing in Field M provides the basis to assume that in this field the porosity model components have a degree of connectivity among components. With the assumption that all porosity components are connected the basis of the dual porosity model fits best the field characteristics. Equation 4.2 is the dual porosity model for a reservoir composed of fractures and matrix porosity:

$$m = \frac{-\log \left[\frac{1}{\phi_f + (1 - \phi_f) / \phi_b^{-m_b}} \right]}{\log \phi} \quad (4.2)$$

Where:

m = Cementation exponent of the composite system,

m_b = Cementation exponent related to the matrix porosity of the bulk volume without including fractures,

ϕ = Total porosity (total porosity = effective porosity),

ϕ_f = Fracture porosity relative to the bulk volume of the composite system,

ϕ_b = Matrix block porosity relative to the bulk volume of the composite system

Also note that ϕ_b can be expressed as a ratio shown below. This is particularly important when applying the model at the log scale.

$$\phi_b = \frac{\phi - \phi_f}{1 - \phi_f} \quad (4.3)$$

The dual porosity model for estimating the cementation exponent requires knowledge of the matrix cementation exponent (m_b) to then estimate a cementation exponent (m) representative of the composite system of matrix and fractures. Other variables are, fracture porosity (ϕ_f), total effective porosity (ϕ), and the matrix porosity ϕ_b attached to the bulk volume of the composite system minus the fractures and vugs volume. The fracture porosity term includes the pore space from fractures that may possibly be open and/or touching vugs resulting from dissolution. Another condition to apply the equation is that the cementation exponent of the composite system cannot be larger than the cementation exponent of the matrix, or lower than 1 which is the cementation exponent assumed for a fracture ($m_f < m < m_b$).

Selecting a meaningful porosity model and establishing the degree of connectivity among the porosity components is critical for determining cementation exponent values reflecting pore geometry effects. Equation 4.2 is adapted to include the effects of Field M five porosity components: macrofracture, low conductivity fracture, microfracture, fractured shale, dissolution and intergranular porosity (Figure 1.4). The high degree of fracturing, fracture size variability and the dynamic data indicate that in this field all porosity components are connected to some degree. As a result, the cementation exponent model is modeled as a parallel resistance network. The following steps shown the mathematical derivation of the proposed cementation exponent model in the present study:

1. The first step is to define the Archie's relationships for the composite system (fractures and matrix).

$$R_{fot} = F_t R_w \quad (4.4)$$

$$F_t = \phi^{-m} \quad (4.5)$$

Where:

R_{tot} = Formation true resistivity of the composite system,

F_t = Formation factor of the composite system,

R_w = Formation water resistivity at reservoir conditions,

\emptyset = Total porosity (total porosity = effective porosity),

m = Cementation exponent for the composite system

2. Similarly the basic Archie's relationships for the matrix porosity are defined as:

$$R_o = F R_w \quad (4.6)$$

$$F = \emptyset_b^{-m_b} \quad (4.7)$$

Where:

R_o = Resistivity of the matrix system at reservoir conditions at 100% water saturation,

F = Formation factor of the matrix,

R_w = Formation water resistivity at reservoir conditions,

\emptyset_b = Matrix block porosity attached to the bulk volume of the matrix system,

m_b = Cementation exponent related to the matrix porosity of the bulk volume without including fractures

3. Applying the parallel resistance concept in the resistivity associated with the porosity components are expressed as the sum of the reciprocals. The left side of Equation 4.8 represents the resistivity of the composite system. The right hand side presents the resistivity of the composite system in terms of individual components. Note that the macrofractures and low conductivity fractures are associate with the water resistivity. The third term represents the resistivity of the matrix porosity. Note that the matrix porosity can be expressed as $\emptyset_m = 1 -$

$\phi_{MF} - \phi_{LCF}$. and that the total porosity is expressed as the sum of the porosity components ($\phi = \phi_{MF} + \phi_{DISH} + \phi_{LCF} + \phi_{mf}$).

$$\frac{1}{R_{tot}} = \frac{\phi_{MF}}{R_w} + \frac{\phi_{LCF}}{R_w} + \frac{[1 - \phi_{MF} - \phi_{LCF}]}{R_o} \quad (4.8)$$

Where:

ϕ_{MF} =Porosity of macrofractures,

ϕ_{LCF} =Porosity of low conductivity fractures,

ϕ_m =Matrix porosity

4. Replacing R_{tot} , and R_o terms derived from Equations 4.4 through 4.7 and replaced into 4.8, the equation reduces to:

$$\frac{1}{\phi^{-m} R_w} = \frac{\phi_{MF} + \phi_{LCF}}{R_w} + \frac{[1 - \phi_{MF} - \phi_{LCF}]}{\phi_b^{-m_b} R_w} \quad (4.9)$$

5. Isolating the cementation exponent of the composite system from Equation 4.9:

$$m = \frac{-\log \left[\frac{1}{(\phi_{MF} + \phi_{LCF}) + (1 - \phi_{MF} - \phi_{LCF}) / \phi_b^{-m_b}} \right]}{\log \phi} \quad (4.10)$$

For Equation 4.10 to be applicable the following conditions must be true: $m_f < m < m_b$ and $m_f = 1$. In Equation 4.10 all variables are derived from log curves except m_b , which is obtained from picket plots using core measurements. These values are: Well 1,2 and 3= 2.07, Well 4 =1.95 and Well 5= 1.78.

4.1.4 Permeability

Core measurements show that matrix permeability is low, ranging between 0.00031 mD to 0.2 mD (Repsol, 2008). The permeability of poorly connected low conductivity fractures ranges from 10 mD to 18 mD. The macrofractures, fault like sized fractures, supply the productive permeability vary from 2,000 mD to 7,000 mD (Repsol, 2010).

The r_{p35} diagnostic plot for core data, Figure 3.2 in Chapter 3, shows that permeability in Field M has a strong relationship to pore throat radius and not to porosity. For example a fracture with less than 1% porosity could act as very permeable conduit. The r_{p35} correlation best estimates the high permeability values in fractured zone, because it links permeability to the pore throat radius rather than permeability. Furthermore, the fracture permeability is estimated from the r_{p35} correlation using fracture porosity and fracture aperture from FMI logs as inputs. The matrix permeability is estimated using Equation 4.11 derived from semi-log plot of core measurements.. The permeability log curve for the composite system, fractures and matrix, is the resultant curve of the matrix and fracture permeability curves.

$$k_{matrix} = 4.76 \times 10^{-04} e^{91.5\phi_e} \quad (4.11)$$

Where:

ϕ_e = Effective porosity from logs, fraction,

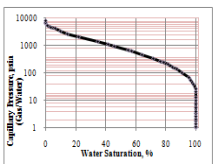
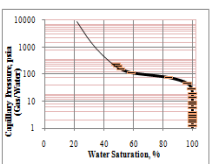
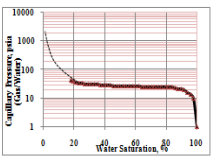
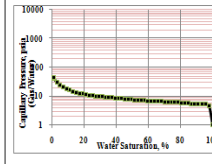
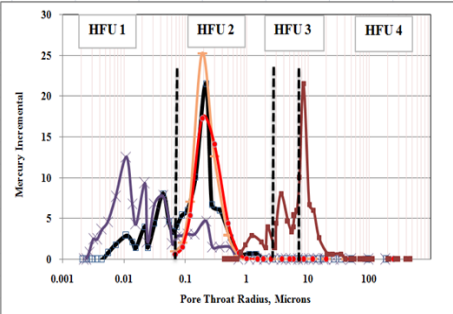
k_{matrix} = Estimated matrix permeability, mD

4.1.5 Rock Typing- Hydraulic Flow Units Determination

In this section a number of rock typing techniques have been investigated. Archie (1950) defined rock types in terms of similarity between petrophysical properties such as porosity,

permeability, capillary pressure and water saturations. Rushing et al., 2008, Deng et al., 2011 and Aguilera, 2003a, presented concepts to define rock types that include features of interest for this research. Rushing et al., 2008 shows how a semi-log plot of incremental mercury volume and pore throat radius r_{p35} plot is used as an additional tool to define hydraulic rock types or hydraulic flow units. Deng et al., (2011) and Aguilera (2003a) demonstrate the r_{p35} correlation as an excellent tool to delineate hydraulic flow units. These concepts are used to define hydraulic flow units (HFU) rock types to identify the most representative capillary pressure profile where characteristic rock properties are predominant. Integrating the observations from: initial petrophysical parameters (Table 2.1), r_{p35} diagnostic plot for core data (Figure 3.2), and a semi-log plot of incremental mercury volume versus pore throat radius (Figure 3.4) four HFU are defined. Table 4.2 summarizes the petrophysical parameters, pore throat size distribution and capillary pressure profiles for these four HFU.

Table 4.2: Hydraulic Flow Units to Select Capillary Pressure Profiles

| Characteristics | HFU1 | HFU2 | HFU3 | HFU4 |
|-------------------------------|--|---|--|---|
| Porosity, % | 3--7 | 3--7 | 3--7 | 3--7 |
| Permeability, mD | 0.0002-0.01 | 0.003--2 | 13--18 | 2000-7000 |
| Vclay% | <15 | 7--15 | 0--7 | 0--7 |
| Pore Throat Radius r_{p35} | > 0.007 | 0-6 | 6--10 | <10 |
| Capillary Bound Water | High | Medium | Very Low | Very Low |
| Capillary Pressure Profile |  |  |  |  |
| Pore throat size distribution |  | | | |

In Chapter 3 it was observed that petrophysical properties could be better characterize, when using pore throat size distribution as the main rock descriptor. The proposed rock typing methodology follows these findings.

HFU1 is characterized by a bimodal pore throat size distribution observed in shaly sand samples. The presence of clay in this rock shifts the pore throat size distribution to lower end values. The high clay content does not have a great effect in the already low porosity, however the permeability is greatly reduced. Because the presence of small pore throats, high irreducible water saturations values from capillary and clay bound water are expected. HFU2 has a dominant pore throat size in the range of 0.07 to 6 microns. This rock has less clay content which indicates higher degree of fracturing and bigger pore throat sizes. Porosity for this rock is expected to be in the higher end values, while permeability is still low in the ranges of 0.003 mD to 2 mD. HFU1 and HFU2 are expected to be present in the matrix. HFU3 is an intermediate rock type between HFU2 and HFU4. This rock type corresponds to rocks where low conductivity fractures are present. The pore throat radius range values for this rock type is not certain, but using the r_{p35} correlation a range of values is established. The degree of connectivity is what differentiates HFU3 from HFU4. Rock type HFU4 is a rock in which highly conductive fractures are predominant. These fractures have very low porosity, so their presence does not affect matrix porosity. Permeability values are extremely high in the ranges of 2000 mD to 7000mD. Pore throat sizes higher than 6 microns are indicative of these large scale fractures, with medium to extremely high permeability values and very low irreducible water saturations.

Figure 4.6 illustrates the application of the proposed rock type methodology at the log scale. The pore throat size curve for the matrix is obtained using r_{p35} (Eq. 2.25). Fracture apertures estimated from image logs are used as analogs for the pore throat size of large

fractures. The histogram in the fifth track indicates that the predominant rock type is HF4 which is distinguished by pore throat sizes bigger than 10 microns.

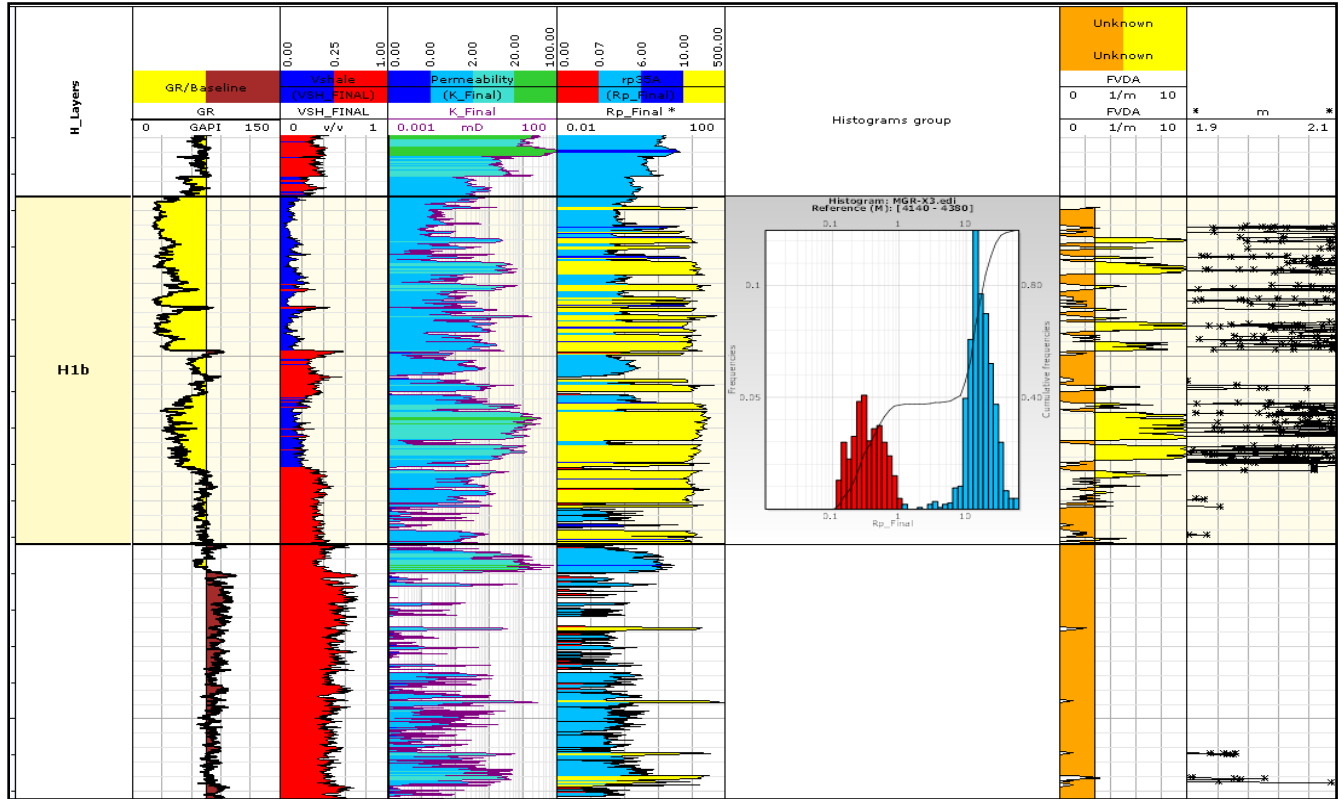


Figure 4.6: Log plot used to define predominant HFU for Well 3. Track 1: Gamma ray, API Track 2: Volume of shale, fraction Track 3: Permeability, mD Track 4: Pore throat radius, microns Track 5: Histogram of pore throat radius showing a bimodal distribution, Track 6: Fracture density interpreted from image logs, 1/meter Track 7: Cementation exponent, unitless

4.2 Modeled Capillary Pressure Water Saturation and Log Derived Water Saturation

In this section a saturation height function (SHF) calibrated to core capillary pressure is used to model water saturation profiles. The results from SHF are compared to the water saturation profiles derived from resistivity logs using the Indonesian equation. The objective is to test the feasibility of using capillary pressure core measurements to model water saturation profiles at the log scale. For this purpose a commercial software Techlog and the Techcore

module is used to model a SHF. Four correlations to model capillary pressure are available in the Techcore module: Brooks and Corey, Lambda, Thomeer and J-Leverett. The fundamentals of these correlations and equations have been summarized in Chapter 2.

The SHF model setup can be summarized as follows:

1. The correlation that best fits the field core capillary pressure is selected. From the four available correlations in Techlog, Thomeer and J-Leverett fit better the core data. Each correlation has predictive relationships between porosity and permeability, which are fitted using different functions (linear, logarithmic, exponential, power and average).
2. The fitted predictive relationships found in step 1 are imported to the Techlog saturation height modeling module. The known free water level and the fluid densities are entered to model water saturation profiles using the saturation height model.
3. Four set-ups for Well 3 to estimated water saturation profile using the SHF model are obtained and compared to the log resistivity water saturation profile. The first two set ups are constructed using the J-Leverett and Thomeer correlations. These setups use predictive relationships obtained from fitting the correlations to all available core capillary pressure curves for the field. The other two set ups use the J-Leverett and Thomeer correlations with predictive relationships found from fitting the correlations using one capillary pressure curve. These setups use a single core capillary pressure from a sample with rock properties similar to the hydraulic flow unit 4 (HFU4), which is the predominant rock type on the investigated depth, Figure 4.6.

Figure 4.7 shows the curves obtained from the four SHF model setups compared to the log resistivity water saturation profile. Track 3 shows the SHF models using the Leverett and the

Thomeer correlations using all core samples. The water saturation profiles from the Leverett and the Thomeer show lower values than the conventional water saturation profile. In track 4 the SHF model from Thommer with the hydraulic flow unit concept shows the closest match to the water saturation from resistivity logs. The water saturation profiles from the Leverett correlation yield very low values indicating that Thomeer correlation is more robust.

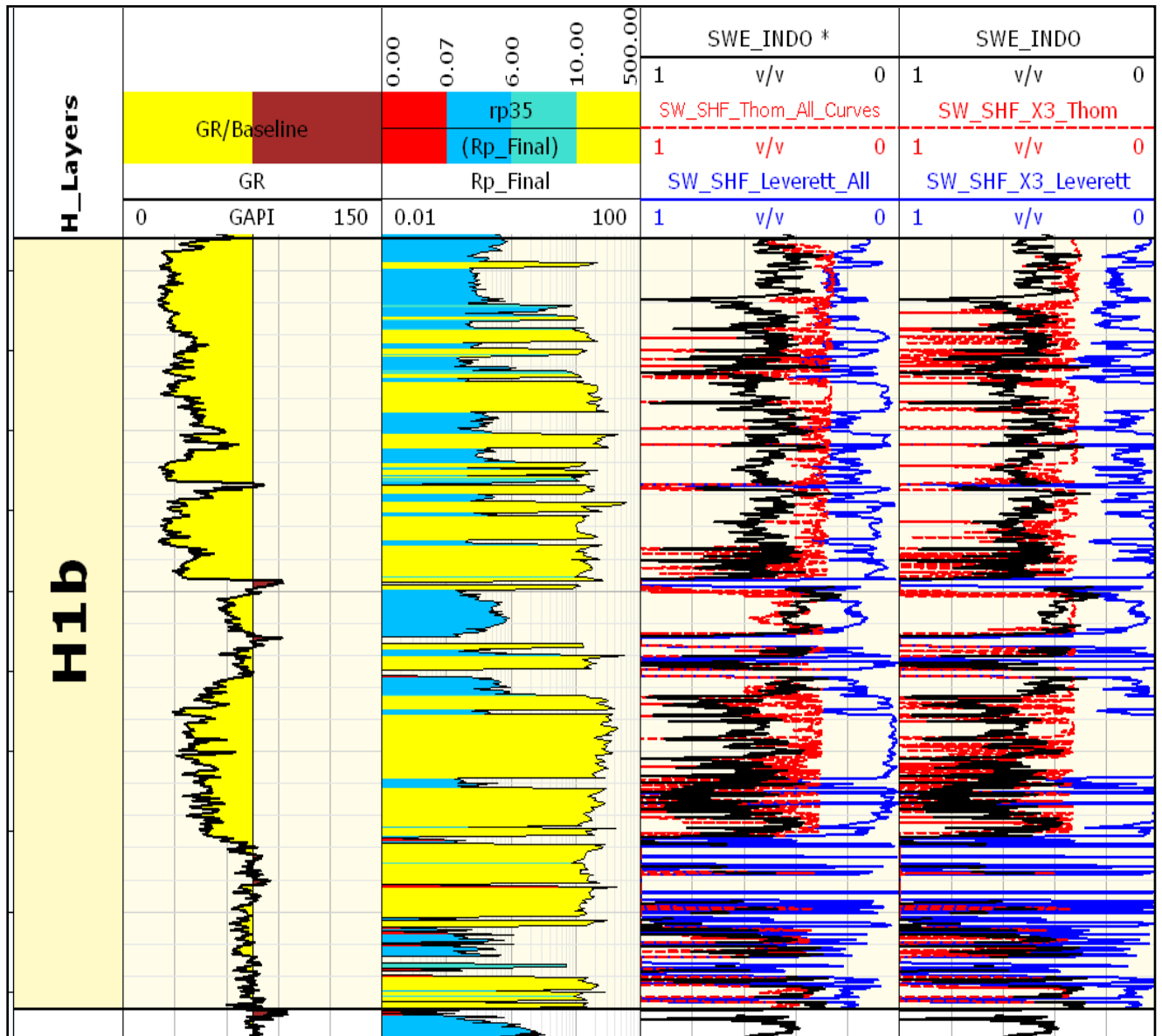


Figure 4.7: Results from applying saturation height function in Well 3.

4.3 Summary

Petrophysical evaluation using log and core data to obtain a log derived water saturation profile wells is implemented. Field M petrophysical evaluation is highly complex. Breakouts and washouts on the wells have introduced uncertainty in the log data. In addition to the data quality and the low number of wells drilled in the formation, the complex mineralogy, the low salinity formation water, shale lamination and gas presence make the log interpretation difficult. From these the low salinity formation water introduces the most uncertainty to the water saturation estimations. Nonetheless the log derived petrophysical properties show reasonable results compared to the geological description and core measurements.

In addition to the petrophysical evaluation a methodology to delineate hydraulic flow units (HFU) to select a representative core capillary pressure is proposed. The objective of this methodology is to match the core sample rock properties to the predominant rock properties found on the depth interval being evaluated. The methodology integrates observations from analyzing core measurement and other sources resulting in a framework for the rock properties of four HFU (Table 4.2).

In this chapter the feasibility of using Field M core capillary pressure data to model a water saturation profile is tested. Field M capillary pressure measurements can be used to model water saturation distributions using a known free water level. The SHF water saturation profiles compared well to the water saturation profiles derived from resistivity. The fourth SHF setup, an optimized Thomeer model through the application of the HFU, shows the closest match to the saturations from resistivity logs.

CHAPTER 5

DISCUSSION OF RESULTS

This chapter outlines the results from the present research, and briefly covers the validity of the applied methods and the implications of the data quality.

5.1 Results from Pore Scale Simulation

In Chapter 2 methods to evaluate capillary pressure at the core and log scale are reviewed. It is found that all these methods implicitly or explicitly are a function of the average pore radius $r_p = \sqrt{\frac{8k}{\phi}}$ as first proposed by Leverett (1939). Following this principle an r_{p35} diagnostic plot (Figure 3.2) using core data is made to analyze the relationship between porosity, permeability and pore throat size distribution. It is observed that a constant porosity various permeability values can be found indicating that permeability has a direct relationship to pore throat radius hence capillary pressure.

The results from simulation confirmed this hypothesis, demonstrating that the main property affecting capillary pressure profiles is the pore throat size distribution. Matching simulated and experimental capillary pressure curves resulted in different permeability values. Core permeability are measured using helium injection showing smaller values than the permeability obtained from the simulations. This indicates that the state of the core might have been affected during mercury injection increasing the pore throat radius or the connectivity by creating additional fractures. The samples with higher clay content (Sample Ref#16) do not show great variation between the experimental and the simulated permeability. On the other hand, the difference between simulated and experimental permeability values for cleaner samples, higher

brittleness (Sample Ref#88), is greater than for the samples with high clay content. Moreover, the results from the case scenarios simulation indicate that small variations in connectivity and pore throat size distribution can have an effect on capillary pressure in the order of one or two orders.

The biggest limitation in pore scale simulation is the constraint to change input parameters in the software. Although a pore network from an analogous rock is used to run the simulations, the match between experimental and simulated values is improved compared to an statistical pore network. The biggest improvement for the pore scale simulation would be to obtain 3D CT scans from Field M core samples to generate an accurate pore network and to measure capillary pressure profiles. Designing the experimental set ups for these measurements would also improve the accuracy of the investigation.

5.2 Results from Log Analysis

In this field petrophysical evaluation using logs is very challenging. Log quality is highly affected by washouts. Here the application of the saturation height function (SHF) to model water saturation profile is demonstrated in Well 3. This well was selected because of the quality of the log data and the very well defined free water level. Due to the low log data quality, it is recommended the results are taken as qualitative rather than quantitative.

Glorioso et al., (2003), shows that capillary pressure profiles from NMR pore throat size profiles can be used to estimate water saturation profiles in this field. In line with Glorioso's findings and the results from pore scale simulation a methodology to estimate water saturation profiles using SHF with a strong link to the pore throat size distribution is presented. The results from applying this methodology in Well 3 are comparable to the water saturation from resistivity

logs. Future work would include the application of this methodology in log data that is of higher quality reducing uncertainties and validating the methodology.

Another finding important to highlight is the development of a cementation exponent model that includes the effect of all components of the porosity model, matrix and fractures (Sivila et al., 2011). Water saturation profiles using the new cementation exponent model and the Borai (1985) method do not show a significant difference. Nonetheless it was observed that the modeled cementation exponent can be used as an additional tool to characterize the presence of fractures on the system. A closer inspection of the log plots in Appendix D show that the variation of cementation exponent values (m) is comparable to the fracture density from FMI logs. This finding is important to characterize the presence of fractures particularly for those wells without FMI logs. In short m from the model presented here can be used as a fracture index.

5.3 General Remarks

The main hypothesis on this research is that the driving parameter to model capillary pressure in Field M is the pore throat size distribution. Literature review, results from pore scale simulation and log evaluation support this theory. Furthermore, in this research there are some assumptions that need to be reviewed into more detailed. Field M is highly affected by structural complexities, so that the assumption of original hydrostatic equilibrium for capillary pressure evaluation might not be applicable. On the other hand, the intense fracturing could have allowed a new hydrostatic equilibrium to occur. It could also be possible that in highly fractured zones the transition zone is absent. If the fracture density in the matrix is evaluated, the uncertainties associated with these assumptions could be reduced.

CHAPTER 6

CONCLUSIONS AND RECOMMENDATIONS

The main objective of this research is to increase the understanding of core capillary pressure profiles in Field M. Then, a saturation height function calibrated to core capillary pressure is used to estimate water saturation profiles to demonstrate the applicability of this measurement. The workflows summarizing the steps for pore scale simulation and the application of the saturation height function can be found in Appendix E and F, respectively.

6.1 Conclusions

The present research led to the following conclusions:

1. The methodology presented in this research is applicable for a field with similar characteristics as Field M to improve the understanding of core capillary pressure profiles.
2. Capillary pressure in Field M is strongly linked to the pore throat size distribution and connectivity (degree of fracturing), hence permeability.
3. Pore scale simulation results show that the samples with less clay content have more uncertainty. The differences in capillary pressure profiles and permeability values between the core measurements and simulation results are significant for samples with less clay content. This suggests that as the clay content decreases, the pore system is more likely to be affected.
4. Capillary pressure core measurements from Field M can be used to estimate fluid distribution at the log scale from a known free water level, since the results are comparable to the resistivity water saturation profiles.

Supplementary conclusions for this research include:

- a) Case scenarios from pore scale simulation results show that a small variation of fracture density, number of fractures, and pore throat size have a significant effect of one to two orders on capillary pressure values, hence permeability.
- b) Defining hydraulic units in terms of capillary pressure is valuable to understand capillary pressure profiles and improve upscaling to the log scale.
- c) Combining results from evaluations at the pore, core and log scale helped to predict capillary pressure profiles that included features from the composite system, matrix and fractures.
- d) The new cementation exponent can be used as an index for the presence of fractures in wells where FMI logs are not available.

6.2 Recommendations

The methodology of evaluation in this work could be improved with the following recommendations:

1. Obtain CT Scans from Field M core samples to supply a 3D pore system network to improve the certainty of the pore scale simulation.
2. Perform additional capillary pressure core measurements using centrifuge and mercury injection methods.
3. Perform pore scale simulations with a simulator that allows a wider range of variation on the input properties, i.e. coordinator number, bimodal pore throat distributions, etc.
4. Due to the extreme borehole environment the logging program should be carefully planned to avoid introducing more errors in data acquisition, so uncertainty is reduced in new log data.

5. Improve the petrophysical evaluation by acquiring new data. As mentioned before, logging in this field is extremely difficult, so new log data should be well planned. If borehole conditions permit RT scanner measurements of vertical and horizontal resistivity should be obtained to improve the analysis on the laminated zones. The addition of NMR (Nuclear Magnetic Resonance) measurements could improve the assessment of pore throat size distribution and irreducible water saturation. Due to the uncertainty of the water resistivity values, it will be important to monitor salinity of produced water.
6. Field M is composed of fractures from various sizes, hence the petrophysical properties are changing as the reservoir is depleted due to pore pressure changes. In this line a pore pressure and earth mechanical models should be integrated to assess the stress effect in petrophysical properties, which are used to model capillary pressure.
7. Field M petrophysical properties are dependant in the fracture model, density and size, therefore the findings from this work should be completed with other sources of data in an integrated analysis.
8. Perform an in depth integrated analysis to improve the understanding of the free water level, fluid contacts and seals.

NOMENCLATURE

| | |
|-----------|---|
| API | = American petroleum institute units |
| BCF | = Billion cubic feet |
| BCM | = Billion cubic meters |
| FMI | = Fullbore micro imager |
| FZI | = Flow zone unit |
| LCF | = Low conductivity fractures |
| MCMD | = Million cubic meters per day |
| NMR | = Nuclear magnetic resonance |
| PSM | = Pore scale modeling |
| PVT | = Pressure volume temperature |
| RQI | = Reservoir quality index |
| SCF/BBL.. | = Standard cubic feet per barrel |
| SCM/BBL.. | = Standard cubic meters per barrel |
| SHF | = Saturation height function |
| TCF | = Trillion cubic feet |
| XRD | = X-ray diffraction |
| F_t | = Formation factor of the composite system |
| P_d | = Displacement pressure, graphically equivalent to threshold pressure |
| R_{fot} | = Formation true resistivity of the composite system |
| R_o | = Resistivity of the matrix system at reservoir conditions at 100% water saturation |
| R_W | = Water resistivity |
| R_{sh} | = Resistivity of the nearest shale |

| | |
|---------------|--|
| V_{sh} | = Volume of shale |
| P_d | = Threshold pressure |
| S_e | = Effective water saturation movable water |
| S_{wir} | = Irreducible water saturation |
| m_f | = Fracture cementation factor |
| a | = Tortuosity factor |
| a, b, A, B, C | = Fitting parameters |
| e | = Exponential |
| F | = Formation factor of the matrix |
| F_g | = Pore geometric factor, which defines the shape of the capillary pressure curve |
| g | = Gravitational constant |
| h | = Height above the free water level |
| h_d | = Height above the free water level at the entry pressure |
| J-function | = Leverett dimensionless function |
| k_{rg} | = Relative permeability to gas |
| k_{rw} | = Relative permeability to water |
| lab | = Laboratory conditions |
| m | = Cementation exponent from the composite system |
| max | = Maximum point |
| m_b | = Cementation exponent related to the matrix porosity of the bulk volume without including fractures |
| n | = Saturation exponent |
| P_c | = Capillary pressure |
| r | = Pore throat radius |

| | |
|--------------------------------------|--|
| R | = Spherical phase |
| Ref. | = Reference |
| res | = Reservoir conditions |
| Rp ₃₅ or rp ₃₅ | = Pore throat radius at 35% mercury saturation |
| R _t | = True formation resistivity |
| S _b | = Bulk mercury saturation, ration of mercury volume and bulk volume |
| S _{b∞} | = Bulk mercury saturation at infinite pressure assumed equal to porosity |
| S _w | = Water saturation |
| <i>DISH</i> | = Dissolution, Intergranular and Fractured shale |
| <i>LCF</i> | = Low conductivity fractures |
| <i>MF</i> | = Macrofractures |
| <i>mf</i> | = Microfractures |
| <i>v</i> | = Partitioning coefficient, ratio of fracture porosity to total porosity |
| ρ _{nw} | = Non-wetting phase density |
| ∅ _b | =Matrix block porosity relative to the bulk volume of the composite system |
| ∅ _f | = Fracture porosity relative to the bulk volume of the composite system |
| ∅ _{LCF} | = Porosity of low conductivity fractures, |
| ∅ _m | = Matrix porosity |
| ∅ _{MF} | =Porosity of macrofractures |
| ∅ _{nc} | = Porosity of non connected pores |
| cos θ | = Contact angle |
| ρ _w | = Wetting phase density |
| <i>k_{matrix}</i> | = Estimated matrix permeability |

| | |
|---------------|---|
| \emptyset_e | = Effective porosity |
| k | = Permeability |
| λ | = Pore size distribution |
| σ | = Interfacial tension |
| β | = Shape factor |
| ϕ | = Total porosity |
| Vsh_Final | = Minimum volume of Shale from log evaluation |
| Swe_Indo | = Water saturation estimated using the Indonesia equation |
| Phi_Final | = Minimum porosity value from log evaluation |
| K_2 | = Core permeability |
| K_Final | = Permeability log derived values for the composite system, matrix and fractures |
| Rp_Final | = Pore throat size log derived profile for the composite system, matrix and fractures |

REFERENCES

- Aguilera, R., 1990, Extensions of Pickett plots for the analysis of shaly formations by well logs, *The Log Analyst*, p. 304-312.
- Aguilera, R., 1995, *Naturally Fractured Reservoirs*, PennWell Books, Tulsa, Oklahoma.
- Aguilera, R., 2002, Incorporating Capillary Pressure, Pore Throat Aperture Radii, Height above Free Water Table, and Windland r_{35} Values on Pickett Plots, *AAPG Bulletin*, v. 86, p. 605-624.
- Aguilera, R., 2003a, Determination of matrix flow units in naturally fractured reservoirs, *Journal of Canadian Petroleum Technology*, v.42 No2, p.54-61.
- Aguilera, R., and Aguilera, M, 2003b, Improved Models for Petrophysical Analysis of Dual Porosity Reservoirs, *Petrophysics*, v.44, No 1,p. 21-35.
- Aguilera, R., and Aguilera, R., 2004, A Triple Porosity Model for Petrophysical Analysis of Naturally Fractured Reservoirs, *Petrophysics*, v. 45, No. 2, March-April, p.157-166.
- Aguilera, R., Conti, J.J., Lagrenade, E., 2003c, Reducing Gas-Production Decline Through Dewatering: A Case History From the Naturally Fractured Aguarague Field, Salta, Argentina, *SPE Reservoir Evaluation & Engineering* Peer Reviewed Publication.
- Al-Ghamdi, A., Chen, B., Behmanesh, H., Farhad Qanbari, Aguilera, R., 2010, An Improved Triple Porosity Model for Evaluation of Naturally Fractured Reservoirs”, *SPE 132879 Trinidad and Tobago Energy Resources Conference*.
- Amaefule, J.O., Atunbay, M., Tiab, D., Kersey, D.G., Keelan, D.K., 1993 Enhanced Reservoir Description: Using Core and Log Data to Identify Hydraulic (Flow) Units and Predict Permeability in Uncored Intervals/Wells, *SPE 26436 SPE-ATCE Conference*.
- Amaefule, J.O., Kersey, D.G., Marschall, D.M., Powell J.D., Valencia, L.E., Keelan, D.K., 1988, Reservoir Description: A Practical Synergistic Engineering and Geological Approach Based on Analysis of Core Data, *SPE 18167 ATCE Conference*.
- Archie, G. E., 1942, The Electrical Resistivity Log as an Aid in Determining Some Reservoir Characteristics: *Petroleum Technology*, v. 1, p. 55-62.
- Archie, G.E., 1950, Introduction to Petrophysics of Reservoir Rocks, *AAPG Bulletin*, v. 34, p. 943-961.
- Asquith, G.B., 1990, *Log Evaluation of Shaly Sandstones: A practical Guide*, AAPG Publication.

- Asquith, G.B., Krygowski, D., 2004, Basic Well Log Analysis, AAPG Methods in Exploration Series, No.16.
- Beaumont, E.A., Foster, N.H., 1995, Exploring for Oil and Gas Traps Treatise of Petroleum Geology, Handbook of Petroleum Geology Series , Chapter 5 and 9.
- Behrenbruch, P., Biniwale, S., 2005, Characterization of Clastic Depositional Environments and Rock Pore Structures Using the Carman-Kozeny Equation: Australian Sedimentary Basins: In press, Journal of Petroleum Science and Engineering (Elsevier)
- Biniwale, S., 2005, An Integrated Method for Modeling Fluid Saturation Profiles and Characterizing Geological Environment Using a Modified FZI Approach: Australian Fields Case Study, SPE 99285-STU, SPE-ATCE Conference.
- Biniwale, S., Behrenbruch, P., 2004, The Mapping of Hydraulic Flow Zone Units and Characterization of Australian Geological Depositional Environments, SPE Asia Pacific Oil and Gas Conference and Exhibition, Perth, Australia.
- Borai, A.M., 1985, "A new correlation for cementation factor in low-porosity carbonates", SPE Formation Evaluation, vol. 4, No 4, p. 495-499.
- Brooks, R., H., Corey, A.T., 1964, Hydraulic Properties of Porous Media, Hydrology Papers v.3, Colorado State University, Fort Collins.
- Brooks, R., H., Corey, A.T., 1966, Properties of Porous Media Affecting Fluid Flow, Journal Irrigation and Drainage Division, ASCE v. 92, p. 61-88.
- Byrnes, A.P., 1997, Reservoir Characteristics of Low-Permeability Sandstones in the Rocky Mountains, The Mountain Geologist, v. 34, No 1.
- Carman, P., C., 1937, Fluid Flow through Granular Beds, Trans. , AICE v. 15, p. 150-166.
- Carman, P., C., 1956, Flow of Gases through Porous Media, Butterworth's Scientific Publications,London, p. 128.
- Coates, G., R., Dumanoir, J., L., 1981, A New Approach to Improved Log Derived Permeability, The Log Analyst, p.17.
- Christiansen, R., 2008, Multiphase Flow Through Porous Media, KNG Engineering.
- Clavier, C.,Coates, G., and Dumanoir, J., 1977, The Theoretical and Experimental Bases for the "Dual Water" Model for the Interpretation of Shaly Sands, SPE-6859, SPE-ATCE Conference.

- Deng, H., Leguizamon, J., Aguilera, R., 2011, Petrophysics of Triple Porosity Tight Gas Reservoirs with a Link to Gas Productivity, SPE 144590, SPE Western North American Regional Meeting, SPE Reservoir Evaluation & Engineering- Formation Evaluation.
- Dewan, J., T., 1983, Essentials of Modern Open-Hole Log Interpretation, PennWell Publishing Co., Tulsa.
- Ebanks, W., J., 1987, Geology in Enhanced Oil Recovery: Reservoir Sedimentology, SEPM Special Publication No 40, p. 1-14.
- Geozum, 2012, San Andrea's Fault Museum Website, Visited on 01/31/2012
- Glorioso, J., C., Aguirre, O., Piotti, G., Mengual, J., F., 2003, Deriving Capillary Pressure and Water Saturation from NMR relaxation, SPE LAC Trinidad and Tobago.
- Hagiwara, T., 1986, Archie's "M" for Permeability, Log Analyst Jan-Feb, p.39-42
- Huet, C.C., 2005, Semi-Analytical Estimates of Permeability Obtained From Capillary Pressure, Msc Thesis, Texas A&M University.
- Inigo, P., J., F., 2009, Structural Model and Fracture Analyses for a Major Gas Emplacement in Devonian Sandstones of the Subandes, Msc. Thesis, University of Texas at Austin.
- Jacques, A.G., 1997, Petrophysical Input to Simulation: Derive Rock Type Maps from Logs Water Saturations and Capillary Pressure Data, SPWLA Symposium.
- Johnson, A., 1987, Permeability Averaged Capillary Data: A Supplement to Log Analysis in Field Studies, SPWLA Symposium.
- Katahara, K., 2008, What is the shale to a petrophysicist?, The Leading Edge.
- Kolodzie, S.Jr., 1980, Analysis of Pore Throat Size and Used of the Waxman-Smiths Equation to determine OOIP in Spindle Field, Colorado, SPE-ATCE.
- Kozeny, J., 1927, Uber-Kapillare Leitung des Wassers in Boden, Sitzungsberichte, Wasserkraft und Wassserwirtschaft, p. 67-86.
- Kwon, B.B., Pickett, G.R., 1975, A New Pore Structure Model and Pore Structure Interrelationships, SPWLA Symposium.
- Leverett, M.C., 1939, Flow of oil-water mixtures through unconsolidated sands, Trans, AIME v. 132, p. 149-171.
- Leverett, M.C., 1941, Capillary Behavior in Porous Solids, Trans, AIME v. 142, p. 341-358.

- McCreech, C.A, Ehrlich, R., Crabtree, S.J., 1991, Petrography and Reservoir Physics II: Relating Thin Section Porosity to Capillary Pressure the Association Between Pore Types and Throat Size, AAPG Bulletin v. 75, No 10, p.1563-1578.
- Nelson, P.H., 2000, Evolution of Permeability-Porosity Trends in Sandstones, SPWLA Symposium.
- Pape, H., Clauser, C., Iffland, J., 1999, Permeability Prediction Based on Fractal Pore Space Geometry, Geophysics, v. 64(5), p. 1447-1460.
- Pickett, G.R., Kwon, B.S., A New Pore Structure Model and Pore Structure Interrelationships, SPWLA Symposium.
- Pittman, E., D., 1992, Relationship of Porosity and Permeability to Various Parameters Derived from Mercury Injection-Capillary Pressure Curves for Sandstone, AAPG Bulletin, v.76 No. 2, p. 191-198.
- Poupon, A. and Leveaux, J., 1971, Evaluation of Water Saturation in Shaly Formations, Trans. SPWLA 12Th Annual Logging Symposium, p. 1-2.
- Purcell, W.R., 1949, Capillary Pressures-Their Measurement Using Mercury and the Calculation of Permeability, AIME 39, p. 186.
- Rahmanian, M., Solano, N., Aguilera, R., 2010, Storage and Output Flow From Shale and Tight Gas Reservoirs, SPE 133611, SPE Western Regional Meeting.
- Repsol YPF Bolivia, 2006, Petrophysics Report.
- Repsol YPF Bolivia, 2007, Fracture Model Report.
- Repsol YPF Bolivia, 2008, Various Core Reports (2008-Well5, 2005-Well4, 2000-Well3 and Well2,1999 and 1998-Well1).
- Repsol YPF Bolivia, 2010, Other Information provided by the company in the form of presentations or summaries, Non-published.
- Revil, A., Cathles III L.M., 1999, Permeability of Shaly Sands, Water Resources Research v. 35, No3, p. 651-662.
- Rodrigues, E., Patricia, 2012, Petrophysical Forward Modeling Class, Advanced Formation Evaluation, Colorado School of Mines.
- Rushing, J.A., Newsham, K.E., Blasingame, T.A., 2008, Rock Typing- Keys to Understanding Productivity in Tight Gas Sands, SPE 114164, Unconventional Reservoirs Conference.

- Serra, O., 1989, "Formation Micro Scanner Image Interpretations: Schlumberger Educational Service, Houston, SMP-7028, p. 117.
- Simandoux, P., 1963, Mesures dialectriques en milieu poreux, application a mesure des saturation en eau, 'etude du comportement des massifs argileux, Revue de l'Institut Francais du Petrole, v. 18, supplementary issue, p. 193-215.
- Sivila, L.J., Graves, R.M., Aguilera, R., 2011, Multiple-Porosity Model For Evaluation of Giant Naturally Fractured Gas Sandstone Reservoirs in Bolivia, SPE 147511 SPE-ATCE.
- Skelt, C.H., Harrison, B., 1995, An Integrated Approach to Saturation Height Analysis, SPWLA Symposium.
- Swanson, B.F., 1981, A Simple Correlation between Permeabilities and Mercury Capillary Pressures, JPT, 2488-2504.
- Thomas, L.K., Katz, D.L., Tek, M.R., 1968, Threshold Pressure Phenomena in Porous Media, SPEJ, p. 174-183.
- Thomeer, J.H.M., 1960, Introduction of a Pore Geometrical Factor Defined by the Capillary Pressure Curve, JPT, pages 73-77.
- Thomeer, J.H.M., 1983, Air Permeability as a Function of Three Pore-Network Parameters, JPT, p. 809-814.
- Timur, A., 1968, An Investigation of Permeability, Porosity, and Residual Water Saturation Relationships for Sandstone Reservoirs, The Log Analyst, v. 9, p. 8-17.
- Towle, G., 1962, An Analysis of the Formation Resistivity Factor-Porosity Relationship of Some Assumed Pore Geometries, SPWLA Transactions, v. 3, paper C.
- Valvatne, H., 2004, Predictive Pore-Scale Modelling of Multiphase, Doctoral Thesis, Imperial College.
- Vavra, C.L., Kaldi, J.G., Sneider, R.M., 1992, Geological Applications of Capillary Pressure: A Review, AAPG Bulletin v. 76, p. 840-850.
- Washburn, E. W., 1921, Note on a Method of Determining the Distribution of Pore Sizes in a Porous Material, National Academy of Science, v.7, p. 115-116.
- Wells, J.D. Amaefule, J.O., 1985, Capillary Pressure and Permeability Relationships in Tight Gas Sands, SPE 13879.
- Wiltgen, N.A., Calvez, J.L., Owen, K., 2003, Methods of Saturation Modeling Using Capillary Pressure Averaging and Pseudos, SPWLA Symposium.

Worthington, P., 2010, Petrophysics of Problematic Reservoirs, March 2010, Short Course at Colorado School of Mines.

Wu, T., 2004, Permeability Prediction and Drainage Capillary Pressure Simulation in Sandstone Reservoirs, Doctoral Thesis, Texas A&M University.

Wu, T., Berg, R.R., 2003b, Relationship of Reservoir Properties for Shaly Sandstones based on Effective Porosity, Petrophysics, v.44, p. 328-341.

APPENDIX A

SUPPLEMENTARY LITERATURE REVIEW

Table A-1: Water Saturation Models

| Author | Equations |
|---|---|
| Archie ,1942 | $S_w = \left(\frac{1}{\phi^m} \times \frac{R_w}{R_t} \right)^{1/n}$ |
| Indonesia Poupon,1983 | $S_w = \left[\frac{\sqrt{\frac{1}{R_t}}}{\left(\frac{V_{sh}^{(1-V_{sh})/2}}{\sqrt{R_{sh}}} \right) \left(\frac{\sqrt{\phi_e^m}}{\sqrt{\alpha * R_w}} \right)} \right]^{2/n}$ |
| Simandoux, 1963 | $S_w = \frac{C R_w}{\phi_e^m} \left[\sqrt{\frac{5\phi_e^2}{R_w * R_t} + \left(\frac{V_{cl}}{R_{sh}} \right)^2} - \frac{V_{cl}}{R_{sh}} \right]$ |
| Dual Water Model Clavier et al.,1977 | $S_{we} = \frac{\left[\frac{[S_b(1-\frac{R_w}{R_b})]}{2} + \sqrt{\left\{ \frac{[S_b(1-\frac{R_w}{R_b})]}{2} \right\}^2 + \left(\frac{R_w}{R_{wa}} \right)} \right]}{(1 - S_b)}$ |
| Poupon et al.,1971 | $S_w^2 = \frac{\alpha(1 - V_{lam})R_w}{\phi^2} \left(\frac{1}{R_t} - \frac{V_{lam}}{R_{sh}} \right)$ |

Table A-2: Cementation Exponent Models-Correlations

| Author | Equations |
|------------------------|--|
| Borai, 1985 | $m = 2.2 - \frac{0.035}{(\phi + 0.042)}$ |
| Al- Ghamdi et al.,2010 | $m = \frac{-\log \left[\phi_{nc} + \frac{(1-\phi_{nc})^2}{\phi_2 + (1-\phi_2 - \phi_{nc})/\phi_b^{-m_b}} \right]}{\log \phi}$ |
| Shell Model | $m = 2.0556 - 2.78 * \phi$ |

Table A-3: Selected Corrections for Log Derived Porosity

| Author | Equations |
|----------------------|--|
| Asquith et al., 2004 | $\phi_{NDgas} = \sqrt{\frac{\phi_N^2 + \phi_D^2}{2}}$ <p>Neutron-Density porosity for a gas zone</p> |
| Dewan, 1983 | $\phi_{Ne} = \phi_N - V_{shale} * \phi_{Nsh}$ $\phi_{De} = \phi_D - V_{shale} * \phi_{Dsh}$ $\phi_{Se} = \phi_S - V_{shale} * \phi_{Ssh}$ |
| Asquith et al., 2004 | $\phi_{sonic} = \left(\frac{\Delta t_{log} - \Delta t_{matrix}}{\Delta t_f - \Delta t_{ma}} * \frac{100}{\Delta t_{shale}} \right) - V_{shale} \left(\frac{\Delta t_{sh} - \Delta t_{ma}}{\Delta t_f - \Delta t_{ma}} \right)$ |
| Katahara, 2008 | $\phi_N - \phi_D$ <p>Study on the Gulf of Mexico Oil Fields the higher the difference the higher the clay presence.</p> |

Table A-4: Permeability Models/Correlations

| Author | Equations |
|----------------------------------|--|
| Kozeny-Carman, 1927,1937,1956 | $k = \frac{\phi_e^3}{(1 - \phi_e)^2} \left(\frac{1}{F_s \tau^2 S_{gv}^2} \right)$ <p style="text-align: center;">Theoretical</p> |
| Coates, 1981 | $k = \left[\frac{100\phi^2(1 - S_{wirr})}{S_{wirr}} \right]^2$ $k = C\phi^4 \left(\frac{FFI}{BVI} \right)^2$ <p style="text-align: center;">Empirical</p> <p style="text-align: center;">Uses NMR data.</p> |
| Pape et al., 1999 | <p style="text-align: center;">Sandstone:</p> $k = 0.031\phi + 7.463\phi^2 + 0.191(10\phi)^{10}$ <p style="text-align: center;">Shaly Sandstone:</p> $k = 0.0062\phi + 1.493\phi^2 + 0.058(10\phi)^{10}$ <p style="text-align: center;">Semi-theoretical</p> |
| Timur, 1968 | $k = A \frac{(100\phi)^{4.4}}{(100 S_{wir})^2}$ $k = 0.136 \frac{(100\phi)^{4.4}}{(100 S_{wir})^2}$ <p style="text-align: center;">Empirical</p> |

Table A-4: Permeability Models/Correlations. Continued

| Author | Equations |
|--------------------------|---|
| Huet, 2005 | $k_{H-B} = 81718.8669 \frac{1}{(P_d)^{1.7846}} \left[\frac{\lambda}{\lambda + 2} \right]^{1.6575} (100 - S_{wi})^{0.5475} \phi^{1.6498} \quad (100)$ <p>Semi-analytical model based on capillary pressure</p> |
| Revil and Cathless, 1999 | <p>Sandstone:</p> $k_{ss} = \frac{10^9 d^2 (\phi_{sd})^{3msd}}{24}$ <p>Clayley Sandstone:</p> $k = k_{ds} \left[1 - \phi_v \left(\frac{1 - \phi_{sh}}{\phi_{sd}} \right) \right]^{3mcs}$ <p>Applicable to core data</p> |

Table A-5: Selected Flow Units Concepts

| Author | Equations or Concepts |
|---------------------------|---|
| Amaefule et al.,1988,1993 | $RQI = \sqrt{\frac{k}{\phi_e}} = \frac{\phi_e}{(1 - \phi_e)} \left(\frac{1}{\sqrt{F_s \tau S_{gv}}} \right)$ $FZI(\mu m) = \left(\frac{1}{\sqrt{F_s \tau S_{gv}}} \right)$ $\phi_z = \frac{\phi_e}{(1 - \phi_e)}$ $\log RQI = \log \phi_z + \log FZI$ |
| Biniwaleet al.,2004 | Proposes the use of geological envelopes overlapping flow zone units determined using Amaefule method. |
| Deng et al., 2011 | Proposes the use of the pore throat radius (Rp35) and cementation exponent to define flow units. |
| Aguilera, 2003a | Presents a workflow to use capillary pressure and picket plots to determine matrix flow units in a naturally fractured reservoir. |
| Jacques, 1997 | Presents a workflow to define rock types maps using log derived water saturation, capillary pressure, permeability, porosity and Vclay. |
| Rushing et al., 2008 | Presents a detailed workflow to characterize tight gas by comparing three rock typing methods: depositional, petrographic and hydraulic |

APPENDIX B

CORE & CAPILLARY PRESSURE DATA

Table B-1:Core Permeability, Porosity and Grain Density (Repsol, 2008)

| Core No | Well No | Sample Name | Grain Density | Porosity @ STD | Porosity @ NOBP | Air Permeability | Klinkenberg Corrected Permeability |
|---------|---------|-------------|--------------------|----------------|-----------------|------------------|------------------------------------|
| | | | gr/cm ³ | % | % | mD | [mD] |
| 1 | Well 1 | 3 | - | - | - | - | - |
| 2 | Well 1 | 2 | 2.64 | 3.50 | - | 0.014 | 0.0056 ^E |
| 3 | Well 1 | 4 | 2.66 | 3.00 | - | 0.004 | 0.0016 ^E |
| 4 | Well 1 | 11 | 2.70 | 3.00 | - | 0.005 | 0.002 ^E |
| 5 | Well 1 | 5 | - | - | - | - | - |
| 6 | Well 1 | 6 | 2.70 | 2.60 | - | 0.008 | 0.0032 ^E |
| 7 | Well 1 | 7 | - | - | - | - | - |
| 8 | Well 1 | 8 | - | - | - | - | - |
| 9 | Well 1 | 9 | 2.66 | 2.10 | - | 0.006 | 0.0024 ^E |
| 10 | Well 1 | 10 | 2.71 | 4.10 | - | 3.43 | 1.372 ^E |
| 11 | Well 2 | 1 | 2.65 | 4.50 | 2.9 | 0.0009 | 0.0001 |
| 12 | Well 2 | 2 | 2.73 | 7.60 | 4.3 | 0.0037 | 0.001 |
| 13 | Well 2 | 11 | 2.65 | 4.90 | 2.3 | 0.002 | 0.0004 |
| 14 | Well 2 | 3F | 2.66 | 5.00 | 4 | 0.847 | 0.569 |
| 15 | Well 2 | 12F | 2.66 | 4.80 | 4 | 0.111 | 0.065 |
| 16 | Well 2 | 4 | 2.67 | 4.60 | 3.6 | 0.0012 | 0.0002 |
| 17 | Well 2 | 5 | 2.68 | 3.70 | 3 | 0.0008 | 0.0001 |
| 18 | Well 2 | 13 | 2.67 | 3.70 | 2.8 | 0.0005 | 0.0001 |
| 19 | Well 2 | 7 | 2.66 | 4.40 | 2.9 | 0.0011 | 0.0002 |
| 20 | Well 2 | 8 | 2.67 | 4.50 | 3.4 | 0.0011 | 0.0002 |
| 21 | Well 2 | 9 | 2.66 | 4.40 | 3.1 | 0.0015 | 0.0003 |
| 22 | Well 2 | 14 | 2.66 | 4.40 | 3.7 | 0.0057 | 0.0017 |
| 23 | Well 2 | 15 | 2.66 | 3.90 | 3.8 | 0.0024 | 0.0006 |
| 24 | Well 2 | 10 | 2.66 | 3.70 | 3 | 0.0017 | 0.0003 |
| 25 | Well 3 | 1F | 2.65 | 5.10 | 4.2 | 3.7518 | 2.9401 |
| 26 | Well 3 | 2 | 2.66 | 5.70 | - | - | - |
| 27 | Well 3 | 2A | 2.66 | 5.10 | - | - | - |
| 28 | Well 3 | 3 | 2.64 | 4.60 | - | - | - |
| 29 | Well 3 | 4 | 2.66 | 5.10 | 3.6 | 0.8999 | 0.6664 |
| 30 | Well 3 | 5F | 2.65 | 5.30 | 3.7 | 8.13 | 6.5056 |

Table B-1: Core Permeability, Porosity and Grain Density (Repsol, 2008), Continued

| Core No | Well No | Sample Name | Grain Density | Porosity @ STD | Porosity @ NOBP | Air Permeability | Klinkenberg Corrected Permeability |
|---------|---------|-------------|--------------------|----------------|-----------------|------------------|------------------------------------|
| | | | gr/cm ³ | % | % | mD | [mD] |
| 31 | Well 3 | 6F | 2.64 | 4.80 | 3.3 | 1.124 | 0.8623 |
| 32 | Well 3 | 7 | 2.64 | 3.70 | 2.7 | 0.0024 | 0.0008 |
| 33 | Well 3 | 8F | 2.65 | 4.20 | 3.2 | 0.0887 | 0.0545 |
| 34 | Well 3 | 9 | 2.67 | 7.00 | - | - | - |
| 35 | Well 3 | 1F-swc | 2.64 | 7.40 | 5.5 | 8.09 | 6.21 |
| 37 | Well 3 | 1-swc | 2.64 | 3.60 | 1.4 | - | 0.0031 |
| 38 | Well 3 | 1 | 2.65 | 3.60 | 2.5 | - | 0.0001 |
| 39 | Well 3 | 2 | 2.66 | 3.70 | 1.5 | - | 0.0005 |
| 40 | Well 3 | 3 | 2.65 | 2.80 | 1.7 | - | 0.0009 |
| 41 | Well 3 | 4* | 2.67 | 2.60 | 1.9 | - | 0.0053 |
| 42 | Well 3 | 5 | 2.65 | 2.20 | 2.2 | - | 0.0001 |
| 43 | Well 3 | 6* | 2.65 | 3.90 | 2.9 | - | 0.157 |
| 44 | Well 3 | 7 | 2.65 | 3.00 | 2.3 | - | 0.0009 |
| 45 | Well 3 | 8 | 2.66 | 3.10 | 2.6 | - | 0.0009 |
| 46 | Well 3 | 9 | 2.67 | 3.70 | 3 | - | 0.0007 |
| 47 | Well 3 | 10 | 2.67 | 3.00 | 2.5 | - | 0.0007 |
| 48 | Well 3 | 11 | 2.69 | 2.20 | 1.2 | - | 0.0001 |
| 49 | Well 3 | 12 | 2.74 | 2.30 | 1.4 | - | 0.0001 |
| 50 | Well 3 | 13 | 2.75 | 3.30 | 1.4 | - | 0.0001 |
| 51 | Well 3 | 14 | 2.73 | 2.00 | 0.8 | - | 0.0001 |
| 52 | Well 3 | 15 | 2.73 | 2.40 | 1.8 | - | 0.0001 |
| 53 | Well 3 | 16 | 2.70 | 2.00 | 1.5 | - | 0.0001 |
| 54 | Well 3 | 17 | 2.73 | 2.60 | 0.9 | - | 0.0017 |
| 55 | Well 3 | 18 | 2.72 | 2.50 | 2.1 | - | 0.0013 |
| 56 | Well 4 | 4-1-3-1 F | 2.69 | 4.51 | - | 0.0147 | 0.0059 ^E |
| 57 | Well 4 | 4-1-3-2 F | 2.70 | 4.25 | - | 0.0502 | 0.0201 ^E |
| 58 | Well 4 | 4-1-3-3 F | 2.71 | 4.91 | - | 1.2379 | 0.4952 ^E |
| 59 | Well 4 | 4-1-3-4 F | 2.68 | 4.63 | - | 0.0248 | 0.0099 ^E |
| 60 | Well 4 | 4-1-3-5 M | 2.68 | 2.19 | - | 0.0056 | 0.0022 ^E |

Table B-1: Core Permeability, Porosity and Grain Density (Repsol, 2008), Continued

| Core No | Well No | Sample Name | Grain Density | Porosity @ STD | Porosity @ NOBP | Air Permeability | Klinkenberg Corrected Permeability |
|---------|-----------|---------------|--------------------|----------------|-----------------|------------------|------------------------------------|
| | | | gr/cm ³ | % | % | mD | [mD] |
| 61 | Well 4 | 4-1-3-6 M | 2.68 | 4.00 | - | 0.0149 | 0.0060 ^E |
| 62 | Well 4 | 4-1-2-7 F | 2.71 | 5.31 | - | 0.0355 | 0.0142 ^E |
| 63 | Well 4 | 4-1-2-8 M | 2.72 | 4.48 | - | 0.0234 | 0.0094 ^E |
| 64 | Well 4 | 4-1-2-9 M | 2.69 | 3.62 | - | 0.0190 | 0.0076 ^E |
| 65 | Well 4 | 4-1-2-10 M | 2.69 | 3.11 | - | 0.0797 | 0.0319 ^E |
| 66 | Well 4 | 4-1-2-11 F | 2.70 | 4.03 | - | 35.4947 | 14.1979 ^E |
| 67 | Well 4 | 4-1-2-12 F | 2.70 | 4.27 | - | 0.0480 | 0.0192 ^E |
| 68 | Well 4 | 4-1-1-13 F | 2.70 | 3.81 | - | 3.3179 | 1.3272 ^E |
| 69 | Well 4 | 4-1-1-14 M | 2.68 | 3.62 | - | 0.0109 | 0.0044 ^E |
| 70 | Well 4 | 4-1-1-16 M | 2.67 | 3.22 | - | 0.0074 | 0.0030 ^E |
| 71 | Well 4 | 4-1-1-17 F | 2.69 | 3.10 | - | 0.0212 | 0.0085 ^E |
| 72 | Well 4 | 4-1-1-18 F | 2.70 | 2.63 | - | 0.0262 | 0.0105 ^E |
| 73 | Well 4 ST | 4 ST 1-4-1 F | 2.67 | 5.40 | - | 0.7238 | 0.2895 ^E |
| 74 | Well 4 ST | 4 ST 1-4-2 F | 2.64 | 5.32 | - | 9.2255 | 3.6902 ^E |
| 75 | Well 4 ST | 4 ST 1-4-3 M | 2.63 | 4.33 | - | 0.6417 | 0.2567 ^E |
| 76 | Well 4 ST | 4 ST 1-3-4M | 2.63 | 3.53 | - | 0.0124 | 0.0050 ^E |
| 77 | Well 4 ST | 4 ST 1-3-5M | 2.63 | 3.97 | - | 0.0274 | 0.0109 ^E |
| 78 | Well 4 ST | 4 ST 1-2-6 F | 2.63 | 4.62 | - | 6.2400 | 2.4960 ^E |
| 79 | Well 4 ST | 4 ST 1-2-7 F | 2.64 | 4.42 | - | 29.6216 | 11.8486 ^E |
| 80 | Well 4 ST | 4 ST 1-2-8 F | 2.66 | 5.24 | - | 0.2188 | 0.0875 ^E |
| 81 | Well 4 ST | 4 ST 1-2-9 F | 2.64 | 3.60 | - | 0.0336 | 0.0134 ^E |
| 82 | Well 4 ST | 4 ST 1-1-10 M | 2.65 | 4.73 | - | 0.9223 | 0.3689 ^E |
| 83 | Well 4 ST | 4 ST 1-1-11 F | 2.67 | 4.75 | - | 14.9610 | 5.9844 ^E |
| 84 | Well 5 | 1-2-1F | 2.65 | 4.06 | 3.5733 | 0.5150 | 0.2060 ^E |
| 85 | Well 5 | 1-2-2 | 2.67 | 4.31 | 3.8091 | 0.0023 | 0.0009 ^E |
| 86 | Well 5 | 1-2-3 | 2.66 | 3.99 | 3.1192 | 0.0037 | 0.0015 ^E |
| 87 | Well 5 | 1-2-4F | 2.66 | 3.27 | 2.7790 | 0.0102 | 0.0041 ^E |
| 88 | Well 5 | 1-2-5 | 2.65 | 3.39 | 2.9878 | 0.0007 | 0.0003 ^E |
| 89 | Well 5 | 1-1-6F | 2.65 | 3.20 | 2.2275 | 0.5020 | 0.2008 ^E |
| 90 | Well 5 | 1-1-7 | 2.67 | 3.94 | 3.5083 | 0.0007 | 0.0003 ^E |

Notes.
1. E= Klinkenberg permeability estimated using a 0.4 factor.
2. Net overburden pressure for porosity measurement: Well 2=6300 psi ; Well3= 4610 psi and 7200 psi; Well5= 4921 psi
3. In sample name: F = fractured , M= Matrix, swc=sidewall core, ST= sidetrack, *= not suitable for overburden measurements

Table B-2 Capillary Pressure Data, (Repsol, 2008)

| Reference N° | 16 | | Reference N° | 21 | | Reference N° | 44 | |
|--------------------|--------------------|--------------------|--------------------|--------------------|--------------------|--------------------|--------------------|--------------------|
| Porosity | 0.04 | fraction | Porosity | 0.03 | fraction | Porosity | 0.03 | fraction |
| Permeability | 0.01 | mD | Permeability | 0.0015 | mD | Permeability | 0.01 | mD |
| Capillary Pressure | Mercury Saturation | Pore Throat Radius | Capillary Pressure | Mercury Saturation | Pore Throat Radius | Capillary Pressure | Mercury Saturation | Pore Throat Radius |
| psia | % | µm | psia | % | µm | psia | % | µm |
| 0.08 | 0 | 185.1 | 0.08 | 0 | 185.1 | 0.08 | 0 | 188.3 |
| 0.15 | 0 | 95.0 | 0.15 | 0 | 95.0 | 0.15 | 0 | 95.8 |
| 0.29 | 0 | 51.0 | 0.29 | 0 | 51.0 | 0.29 | 0 | 51.3 |
| 0.42 | 0 | 34.7 | 0.42 | 0 | 34.7 | 0.42 | 0 | 34.8 |
| 0.55 | 0 | 26.6 | 0.55 | 0 | 26.6 | 0.55 | 0 | 26.6 |
| 0.75 | 0 | 19.5 | 0.75 | 0 | 19.5 | 0.75 | 0 | 19.4 |
| 0.82 | 0 | 17.9 | 0.82 | 0 | 17.9 | 0.82 | 0 | 17.9 |
| 1.02 | 0 | 14.4 | 1.02 | 0 | 14.4 | 1.02 | 0 | 14.4 |
| 1.15 | 0 | 12.7 | 1.15 | 0 | 12.7 | 1.15 | 0 | 12.7 |
| 1.42 | 0 | 10.3 | 1.42 | 0 | 10.3 | 1.42 | 0 | 10.3 |
| 1.76 | 0 | 8.351 | 1.76 | 0 | 8.338 | 1.76 | 0 | 8.351 |
| 2.16 | 0 | 6.806 | 2.16 | 0 | 6.784 | 2.16 | 0 | 6.801 |
| 2.69 | 0 | 5.451 | 2.69 | 0 | 5.462 | 2.69 | 0 | 5.453 |
| 3.36 | 0 | 4.369 | 3.36 | 0 | 4.369 | 3.36 | 0 | 4.367 |
| 4.03 | 0 | 3.642 | 4.03 | 0 | 3.641 | 4.03 | 0 | 3.641 |
| 5.38 | 0 | 2.725 | 5.40 | 0 | 2.717 | 5.41 | 0 | 2.710 |
| 7.39 | 0 | 1.985 | 7.37 | 0 | 1.990 | 7.44 | 0 | 1.971 |
| 10.08 | 0 | 1.456 | 10.08 | 0 | 1.454 | 10.07 | 0 | 1.457 |
| 13.42 | 1 | 1.093 | 13.39 | 0 | 1.096 | 13.39 | 0 | 1.095 |
| 20.09 | 1 | 0.730 | 20.01 | 1 | 0.733 | 20.21 | 0 | 0.726 |
| 26.73 | 2 | 0.549 | 26.86 | 1 | 0.546 | 26.89 | 0 | 0.545 |
| 40.16 | 5 | 0.365 | 40.55 | 3 | 0.362 | 40.31 | 0 | 0.364 |
| 53.68 | 11 | 0.273 | 53.71 | 5 | 0.273 | 55.81 | 4 | 0.263 |
| 67.42 | 18 | 0.218 | 69.16 | 12 | 0.212 | 66.96 | 7 | 0.219 |
| 100.24 | 39 | 0.146 | 100.31 | 37 | 0.146 | 105.24 | 19 | 0.139 |
| 134.29 | 49 | 0.109 | 133.75 | 54 | 0.110 | 136.97 | 34 | 0.107 |
| 166.51 | 55 | 0.088 | 169.20 | 61 | 0.087 | 170.54 | 53 | 0.086 |
| 202.77 | 61 | 0.072 | 204.11 | 65 | 0.072 | 204.11 | 66 | 0.072 |
| 233.66 | 65 | 0.063 | 235.00 | 69 | 0.062 | 237.69 | 72 | 0.062 |
| 269.91 | 68 | 0.054 | 267.23 | 71 | 0.055 | 269.91 | 74 | 0.054 |
| 335.72 | 73 | 0.044 | 334.37 | 75 | 0.044 | 339.74 | 79 | 0.043 |
| 467.32 | 81 | 0.031 | 467.32 | 79 | 0.031 | 470.00 | 84 | 0.031 |
| 601.60 | 85 | 0.024 | 604.29 | 83 | 0.024 | 611.00 | 87 | 0.024 |
| 668.74 | 87 | 0.022 | 668.74 | 84 | 0.022 | 670.09 | 88 | 0.022 |
| 937.32 | 91 | 0.016 | 937.32 | 88 | 0.016 | 935.97 | 91 | 0.016 |
| 1070.26 | 92 | 0.014 | 1068.92 | 89 | 0.014 | 1070.26 | 92 | 0.014 |
| 1342.86 | 94 | 0.011 | 1342.86 | 91 | 0.011 | 1342.86 | 94 | 0.011 |
| 2000.86 | 97 | 0.007 | 2000.86 | 93 | 0.007 | 2000.86 | 97 | 0.007 |
| 2672.29 | 99 | 0.005 | 2672.29 | 95 | 0.005 | 2685.72 | 98 | 0.005 |
| 3343.72 | 100 | 0.004 | 3343.72 | 97 | 0.004 | 3357.15 | 99 | 0.004 |
| 4015.15 | 100 | 0.004 | 4028.58 | 98 | 0.004 | 4028.58 | 100 | 0.004 |
| 4686.58 | 100 | 0.003 | 4700.01 | 99 | 0.003 | 4686.58 | 100 | 0.003 |
| 5358.01 | 100 | 0.003 | 5371.44 | 99 | 0.003 | 5371.44 | 100 | 0.003 |
| 6016.01 | 100 | 0.002 | 6042.87 | 100 | 0.002 | 6029.44 | 100 | 0.002 |
| 6714.30 | 100 | 0.002 | 6727.73 | 100 | 0.002 | 6687.44 | 100 | 0.002 |
| 8016.87 | 100 | 0.002 | 8030.30 | 100 | 0.002 | 8030.30 | 100 | 0.002 |

Table B-2 Capillary Pressure Data, (Repsol, 2008), Continued

| Reference N° | 52 | fraction | Reference N° | 32 | fraction | Reference N° | 58 | fraction |
|--------------------|--------------------|--------------------|--------------------|--------------------|--------------------|--------------------|--------------------|--------------------|
| Porosity | 0.02 | fraction | Porosity | 0.03 | fraction | Porosity | 0.05 | fraction |
| Permeability | 0.0002 | mD | Permeability | 0.01 | mD | Permeability | 1.24 | mD |
| Capillary Pressure | Mercury Saturation | Pore Throat Radius | Capillary Pressure | Mercury Saturation | Pore Throat Radius | Capillary Pressure | Mercury Saturation | Pore Throat Radius |
| psia | % | µm | psia | % | µm | psia | % | µm |
| 0.08 | 0 | 182.1 | 0.08 | 0 | 173.4 | 0.11 | 0 | 111.0 |
| 0.15 | 0 | 97.5 | 0.16 | 0 | 94.2 | 0.14 | 0 | 88.5 |
| 0.29 | 0 | 51.3 | 0.29 | 0 | 50.8 | 0.17 | 0 | 71.0 |
| 0.42 | 0 | 34.8 | 0.42 | 0 | 34.8 | 0.21 | 0 | 57.0 |
| 0.55 | 0 | 26.6 | 0.56 | 0 | 26.4 | 0.27 | 0 | 45.5 |
| 0.75 | 0 | 19.5 | 0.75 | 0 | 19.4 | 0.33 | 0 | 36.4 |
| 0.82 | 0 | 17.9 | 0.82 | 0 | 17.8 | 0.42 | 0 | 29.1 |
| 1.02 | 0 | 14.4 | 1.02 | 0 | 14.3 | 0.52 | 0 | 23.3 |
| 1.15 | 0 | 12.7 | 1.15 | 0 | 12.7 | 0.65 | 0 | 18.6 |
| 1.42 | 0 | 10.3 | 1.42 | 0 | 10.3 | 0.82 | 0 | 14.9 |
| 1.76 | 0 | 8.338 | 1.76 | 0 | 8.351 | 1.02 | 0 | 11.900 |
| 2.15 | 0 | 6.827 | 2.16 | 0 | 6.797 | 1.28 | 0 | 9.550 |
| 2.69 | 0 | 5.462 | 2.69 | 0 | 5.456 | 1.60 | 0 | 7.600 |
| 3.36 | 0 | 4.369 | 3.36 | 0 | 4.367 | 2.00 | 0 | 6.100 |
| 4.03 | 0 | 3.641 | 4.05 | 0 | 3.619 | 2.50 | 2 | 4.880 |
| 5.36 | 0 | 2.738 | 5.36 | 0 | 2.736 | 3.12 | 3 | 3.905 |
| 7.41 | 0 | 1.979 | 7.40 | 0 | 1.983 | 3.89 | 5 | 3.125 |
| 10.06 | 0 | 1.458 | 10.04 | 0 | 1.461 | 4.87 | 6 | 2.500 |
| 13.40 | 0 | 1.094 | 13.42 | 0 | 1.093 | 6.08 | 8 | 2.000 |
| 20.14 | 0 | 0.728 | 20.05 | 2 | 0.732 | 7.61 | 10 | 1.600 |
| 26.72 | 0 | 0.549 | 26.76 | 4 | 0.548 | 9.51 | 12 | 1.280 |
| 40.55 | 2 | 0.362 | 40.20 | 8 | 0.365 | 11.88 | 14 | 1.025 |
| 53.58 | 3 | 0.274 | 53.64 | 14 | 0.273 | 14.91 | 16 | 0.820 |
| 67.01 | 5 | 0.219 | 66.98 | 21 | 0.219 | 18.53 | 19 | 0.655 |
| 102.73 | 9 | 0.143 | 100.26 | 45 | 0.146 | 23.23 | 22 | 0.524 |
| 134.69 | 13 | 0.109 | 135.13 | 57 | 0.109 | 29.01 | 25 | 0.419 |
| 169.20 | 16 | 0.087 | 175.50 | 64 | 0.084 | 36.26 | 28 | 0.336 |
| 204.11 | 19 | 0.072 | 217.00 | 69 | 0.068 | 45.39 | 31 | 0.268 |
| 236.34 | 21 | 0.062 | 254.64 | 72 | 0.058 | 56.67 | 36 | 0.215 |
| 268.57 | 23 | 0.055 | 334.37 | 76 | 0.044 | 70.90 | 42 | 0.172 |
| 337.06 | 28 | 0.044 | 467.32 | 81 | 0.031 | 88.63 | 47 | 0.138 |
| 467.32 | 36 | 0.031 | 605.63 | 84 | 0.024 | 110.79 | 52 | 0.110 |
| 608.32 | 43 | 0.024 | 668.74 | 85 | 0.022 | 138.45 | 57 | 0.088 |
| 670.09 | 45 | 0.022 | 938.66 | 89 | 0.016 | 172.96 | 60 | 0.071 |
| 935.97 | 54 | 0.016 | 1138.75 | 90 | 0.013 | 216.33 | 62 | 0.057 |
| 1070.26 | 59 | 0.014 | 1337.49 | 91 | 0.011 | 270.32 | 65 | 0.045 |
| 1342.86 | 65 | 0.011 | 2000.86 | 95 | 0.007 | 338.00 | 67 | 0.036 |
| 2000.86 | 78 | 0.007 | 2672.29 | 97 | 0.005 | 422.46 | 70 | 0.029 |
| 2672.29 | 86 | 0.005 | 3343.72 | 99 | 0.004 | 528.01 | 73 | 0.023 |
| 3343.72 | 90 | 0.004 | 4015.15 | 100 | 0.004 | 660.02 | 75 | 0.019 |
| 4028.58 | 94 | 0.004 | 4418.01 | 100 | 0.003 | 825.05 | 78 | 0.015 |
| 4673.15 | 97 | 0.003 | 5089.44 | 100 | 0.003 | 1031.32 | 81 | 0.012 |
| 5384.87 | 99 | 0.003 | 6029.44 | 100 | 0.002 | 1289.15 | 84 | 0.010 |
| 6042.87 | 100 | 0.002 | 6956.01 | 100 | 0.002 | 1611.43 | 86 | 0.008 |
| 6687.44 | 100 | 0.002 | 8164.59 | 100 | 0.002 | 2014.29 | 88 | 0.006 |
| 8057.16 | 100 | 0.002 | | | | | | |

Table B-2 Capillary Pressure Data, (Repsol, 2008), Continued

| Reference N° | 62 | | Reference N° | 63 | | Reference N° | 66 | |
|--------------------|--------------------|--------------------|--------------------|--------------------|--------------------|--------------------|--------------------|--------------------|
| Porosity | 0.05 | fraction | Porosity | 0.04 | fraction | Porosity | 0.04 | fraction |
| Permeability | 0.04 | mD | Permeability | 0.02 | mD | Permeability | 35.50 | mD |
| Capillary Pressure | Mercury Saturation | Pore Throat Radius | Capillary Pressure | Mercury Saturation | Pore Throat Radius | Capillary Pressure | Mercury Saturation | Pore Throat Radius |
| psia | % | µm | psia | % | µm | psia | % | µm |
| 0.11 | 0 | 111.0 | 0.11 | 0 | 111.0 | 0.11 | 0 | 111.0 |
| 0.14 | 0 | 88.5 | 0.14 | 0 | 88.5 | 0.14 | 0 | 88.5 |
| 0.17 | 0 | 71.0 | 0.17 | 0 | 71.0 | 0.17 | 0 | 71.0 |
| 0.21 | 0 | 57.0 | 0.21 | 0 | 57.0 | 0.21 | 0 | 57.0 |
| 0.27 | 0 | 45.5 | 0.27 | 0 | 45.5 | 0.27 | 0 | 45.5 |
| 0.33 | 0 | 36.4 | 0.33 | 0 | 36.4 | 0.33 | 0 | 36.4 |
| 0.42 | 0 | 29.1 | 0.42 | 0 | 29.1 | 0.42 | 0 | 29.1 |
| 0.52 | 0 | 23.3 | 0.52 | 0 | 23.3 | 0.52 | 0 | 23.3 |
| 0.65 | 0 | 18.6 | 0.65 | 0 | 18.6 | 0.65 | 0 | 18.6 |
| 0.82 | 0 | 14.9 | 0.82 | 0 | 14.9 | 0.82 | 0 | 14.9 |
| 1.02 | 0 | 11.900 | 1.02 | 0 | 11.900 | 1.02 | 0 | 11.900 |
| 1.28 | 0 | 9.550 | 1.28 | 0 | 9.550 | 1.28 | 0 | 9.550 |
| 1.60 | 0 | 7.600 | 1.60 | 0 | 7.600 | 1.60 | 0 | 7.600 |
| 2.00 | 0 | 6.100 | 2.00 | 0 | 6.100 | 2.00 | 0 | 6.100 |
| 2.50 | 0 | 4.880 | 2.50 | 0 | 4.880 | 2.50 | 0 | 4.880 |
| 3.12 | 0 | 3.905 | 3.12 | 0 | 3.905 | 3.12 | 0 | 3.905 |
| 3.89 | 0 | 3.125 | 3.89 | 0 | 3.125 | 3.89 | 0 | 3.125 |
| 4.87 | 0 | 2.500 | 4.87 | 0 | 2.500 | 4.87 | 0 | 2.500 |
| 6.08 | 0 | 2.000 | 6.08 | 0 | 2.000 | 6.08 | 0 | 2.000 |
| 7.61 | 0 | 1.600 | 7.61 | 0 | 1.600 | 7.61 | 0 | 1.600 |
| 9.51 | 0 | 1.280 | 9.51 | 0 | 1.280 | 9.51 | 0 | 1.280 |
| 11.88 | 0 | 1.025 | 11.88 | 0 | 1.025 | 11.88 | 0 | 1.025 |
| 14.91 | 1 | 0.820 | 14.91 | 0 | 0.820 | 14.91 | 1 | 0.820 |
| 18.53 | 1 | 0.655 | 18.53 | 1 | 0.655 | 18.53 | 1 | 0.655 |
| 23.23 | 2 | 0.524 | 23.23 | 2 | 0.524 | 23.23 | 1 | 0.524 |
| 29.01 | 3 | 0.419 | 29.01 | 3 | 0.419 | 29.01 | 2 | 0.419 |
| 36.26 | 5 | 0.336 | 36.26 | 5 | 0.336 | 36.26 | 3 | 0.336 |
| 45.39 | 7 | 0.268 | 45.39 | 9 | 0.268 | 45.39 | 3 | 0.268 |
| 56.67 | 11 | 0.215 | 56.67 | 15 | 0.215 | 56.67 | 5 | 0.215 |
| 70.90 | 15 | 0.172 | 70.90 | 22 | 0.172 | 70.90 | 6 | 0.172 |
| 88.63 | 21 | 0.138 | 88.63 | 29 | 0.138 | 88.63 | 10 | 0.138 |
| 110.79 | 31 | 0.110 | 110.79 | 35 | 0.110 | 110.79 | 17 | 0.110 |
| 138.45 | 40 | 0.088 | 138.45 | 41 | 0.088 | 138.45 | 24 | 0.088 |
| 172.96 | 46 | 0.071 | 172.96 | 44 | 0.071 | 172.96 | 31 | 0.071 |
| 216.33 | 52 | 0.057 | 216.33 | 48 | 0.057 | 216.33 | 38 | 0.057 |
| 270.32 | 57 | 0.045 | 270.32 | 52 | 0.045 | 270.32 | 44 | 0.045 |
| 338.00 | 62 | 0.036 | 338.00 | 57 | 0.036 | 338.00 | 50 | 0.036 |
| 422.46 | 68 | 0.029 | 422.46 | 61 | 0.029 | 422.46 | 56 | 0.029 |
| 528.01 | 72 | 0.023 | 528.01 | 64 | 0.023 | 528.01 | 61 | 0.023 |
| 660.02 | 77 | 0.019 | 660.02 | 68 | 0.019 | 660.02 | 67 | 0.019 |
| 825.05 | 82 | 0.015 | 825.05 | 72 | 0.015 | 825.05 | 72 | 0.015 |
| 1031.32 | 86 | 0.012 | 1031.32 | 75 | 0.012 | 1031.32 | 76 | 0.012 |
| 1289.15 | 89 | 0.010 | 1289.15 | 79 | 0.010 | 1289.15 | 79 | 0.010 |
| 1611.43 | 92 | 0.008 | 1611.43 | 82 | 0.008 | 1611.43 | 82 | 0.008 |
| 2014.29 | 94 | 0.006 | 2014.29 | 84 | 0.006 | 2014.29 | 84 | 0.006 |

Table B-2 Capillary Pressure Data, (Repsol, 2008), Continued

| Reference N° | 69 | | | Reference N° | 72 | | | Reference N° | 74 | | |
|--------------------|--------------------|--------------------|--------------------|--------------------|--------------------|--------------------|--------------------|--------------------|------|----------|--|
| Porosity | 0.04 | fraction | | Porosity | 0.03 | fraction | | Porosity | 0.04 | fraction | |
| Permeability | 0.01 | mD | | Permeability | 0.03 | mD | | Permeability | 9.23 | mD | |
| Capillary Pressure | Mercury Saturation | Pore Throat Radius | Capillary Pressure | Mercury Saturation | Pore Throat Radius | Capillary Pressure | Mercury Saturation | Pore Throat Radius | | | |
| psia | % | µm | psia | % | µm | psia | % | µm | | | |
| 0.11 | 0 | 111.0 | 0.11 | 0 | 111.0 | 0.11 | 0 | 111.0 | | | |
| 0.14 | 0 | 88.5 | 0.14 | 0 | 88.5 | 0.14 | 0 | 88.8 | | | |
| 0.17 | 0 | 71.0 | 0.17 | 0 | 71.0 | 0.17 | 0 | 71.0 | | | |
| 0.21 | 0 | 57.0 | 0.21 | 0 | 57.0 | 0.21 | 0 | 56.8 | | | |
| 0.27 | 0 | 45.5 | 0.27 | 0 | 45.5 | 0.27 | 0 | 45.5 | | | |
| 0.33 | 0 | 36.4 | 0.33 | 0 | 36.4 | 0.33 | 0 | 36.4 | | | |
| 0.42 | 0 | 29.1 | 0.42 | 0 | 29.1 | 0.42 | 0 | 29.1 | | | |
| 0.52 | 0 | 23.3 | 0.52 | 0 | 23.3 | 0.52 | 0 | 23.3 | | | |
| 0.65 | 0 | 18.6 | 0.65 | 0 | 18.6 | 0.65 | 0 | 18.6 | | | |
| 0.82 | 0 | 14.9 | 0.82 | 0 | 14.9 | 0.82 | 0 | 14.9 | | | |
| 1.02 | 0 | 11.900 | 1.02 | 0 | 11.900 | 1.02 | 0 | 11.900 | | | |
| 1.28 | 0 | 9.550 | 1.28 | 0 | 9.550 | 1.28 | 0 | 9.550 | | | |
| 1.60 | 0 | 7.600 | 1.60 | 0 | 7.600 | 1.60 | 0 | 7.600 | | | |
| 2.00 | 0 | 6.100 | 2.00 | 0 | 6.100 | 2.00 | 0 | 6.100 | | | |
| 2.50 | 0 | 4.880 | 2.50 | 0 | 4.880 | 2.50 | 0 | 4.880 | | | |
| 3.12 | 0 | 3.905 | 3.12 | 0 | 3.905 | 3.12 | 0 | 3.905 | | | |
| 3.89 | 0 | 3.125 | 3.89 | 0 | 3.125 | 3.89 | 1 | 3.125 | | | |
| 4.87 | 0 | 2.500 | 4.87 | 0 | 2.500 | 4.87 | 1 | 2.500 | | | |
| 6.08 | 0 | 2.000 | 6.08 | 0 | 2.000 | 6.08 | 2 | 2.000 | | | |
| 7.61 | 0 | 1.600 | 7.61 | 0 | 1.600 | 7.61 | 3 | 1.600 | | | |
| 9.51 | 0 | 1.280 | 9.51 | 0 | 1.280 | 9.51 | 3 | 1.280 | | | |
| 11.88 | 0 | 1.025 | 11.88 | 0 | 1.025 | 11.88 | 4 | 1.025 | | | |
| 14.91 | 0 | 0.820 | 14.91 | 0 | 0.820 | 14.91 | 6 | 0.820 | | | |
| 18.53 | 0 | 0.655 | 18.53 | 0 | 0.655 | 18.53 | 9 | 0.655 | | | |
| 23.23 | 1 | 0.524 | 23.23 | 1 | 0.524 | 23.23 | 13 | 0.524 | | | |
| 29.01 | 2 | 0.419 | 29.01 | 2 | 0.419 | 29.01 | 18 | 0.419 | | | |
| 36.26 | 3 | 0.336 | 36.26 | 4 | 0.336 | 36.26 | 27 | 0.336 | | | |
| 45.39 | 6 | 0.268 | 45.39 | 6 | 0.268 | 45.39 | 34 | 0.268 | | | |
| 56.67 | 10 | 0.215 | 56.67 | 9 | 0.215 | 56.67 | 43 | 0.215 | | | |
| 70.90 | 14 | 0.172 | 70.90 | 13 | 0.172 | 70.90 | 53 | 0.172 | | | |
| 88.63 | 20 | 0.138 | 88.63 | 17 | 0.138 | 88.63 | 59 | 0.138 | | | |
| 110.79 | 27 | 0.110 | 110.79 | 22 | 0.110 | 110.79 | 63 | 0.110 | | | |
| 138.45 | 35 | 0.088 | 138.45 | 28 | 0.088 | 138.45 | 69 | 0.088 | | | |
| 172.96 | 40 | 0.071 | 172.96 | 33 | 0.071 | 172.96 | 72 | 0.071 | | | |
| 216.33 | 45 | 0.057 | 216.33 | 37 | 0.057 | 216.33 | 75 | 0.057 | | | |
| 270.32 | 50 | 0.045 | 270.32 | 41 | 0.045 | 270.32 | 77 | 0.045 | | | |
| 338.00 | 55 | 0.036 | 338.00 | 45 | 0.036 | 338.00 | 79 | 0.036 | | | |
| 422.46 | 60 | 0.029 | 422.46 | 50 | 0.029 | 422.46 | 80 | 0.029 | | | |
| 528.01 | 65 | 0.023 | 528.01 | 54 | 0.023 | 528.01 | 82 | 0.023 | | | |
| 660.02 | 70 | 0.019 | 660.02 | 59 | 0.019 | 660.02 | 83 | 0.019 | | | |
| 825.05 | 75 | 0.015 | 825.05 | 64 | 0.015 | 825.05 | 85 | 0.015 | | | |
| 1031.32 | 78 | 0.012 | 1031.32 | 68 | 0.012 | 1031.32 | 86 | 0.012 | | | |
| 1289.15 | 81 | 0.010 | 1289.15 | 73 | 0.010 | 1289.15 | 87 | 0.010 | | | |
| 1611.43 | 84 | 0.008 | 1611.43 | 77 | 0.008 | 1611.43 | 89 | 0.008 | | | |
| 2014.29 | 86 | 0.006 | 2014.29 | 80 | 0.006 | 2014.29 | 89 | 0.006 | | | |

Table B-2 Capillary Pressure Data, (Repsol, 2008), Continued

| Reference N° | 77 | | Reference N° | 82 | | Reference N° | 85 | |
|--------------------|--------------------|--------------------|--------------------|--------------------|--------------------|--------------------|--------------------|--------------------|
| Porosity | 0.02 | fraction | Porosity | 0.04 | fraction | Porosity | 0.04 | fraction |
| Permeability | 0.03 | mD | Permeability | 0.92 | mD | Permeability | 0.01 | mD |
| Capillary Pressure | Mercury Saturation | Pore Throat Radius | Capillary Pressure | Mercury Saturation | Pore Throat Radius | Capillary Pressure | Mercury Saturation | Pore Throat Radius |
| psia | % | µm | psia | % | µm | psia | % | µm |
| 0.11 | 0 | 111.0 | 0.11 | 0 | 111.0 | 0.06 | 0 | 249.6 |
| 0.14 | 0 | 88.8 | 0.14 | 0 | 88.5 | 0.17 | 0 | 83.2 |
| 0.17 | 0 | 71.0 | 0.17 | 0 | 71.0 | 0.34 | 0 | 41.6 |
| 0.21 | 0 | 56.8 | 0.21 | 0 | 57.0 | 0.72 | 0 | 19.7 |
| 0.27 | 0 | 45.5 | 0.27 | 0 | 45.5 | 1.20 | 0 | 11.9 |
| 0.33 | 0 | 36.4 | 0.33 | 0 | 36.4 | 1.68 | 0 | 8.5 |
| 0.42 | 0 | 29.1 | 0.42 | 0 | 29.1 | 1.96 | 0 | 7.3 |
| 0.52 | 0 | 23.3 | 0.52 | 0 | 23.3 | 2.48 | 0 | 5.8 |
| 0.65 | 0 | 18.6 | 0.65 | 0 | 18.6 | 2.86 | 0 | 5.0 |
| 0.82 | 0 | 14.9 | 0.82 | 0 | 14.9 | 3.81 | 0 | 3.7 |
| 1.02 | 0 | 11.900 | 1.02 | 0 | 11.900 | 5.72 | 0 | 2.500 |
| 1.28 | 0 | 9.550 | 1.28 | 0 | 9.550 | 7.63 | 0 | 1.870 |
| 1.60 | 0 | 7.600 | 1.60 | 0 | 7.600 | 9.53 | 0 | 1.500 |
| 2.00 | 0 | 6.100 | 2.00 | 0 | 6.100 | 14.30 | 0 | 1.000 |
| 2.50 | 0 | 4.880 | 2.50 | 0 | 4.880 | 19.07 | 0 | 0.750 |
| 3.12 | 0 | 3.905 | 3.12 | 0 | 3.905 | 28.60 | 1 | 0.500 |
| 3.89 | 0 | 3.125 | 3.89 | 1 | 3.125 | 47.67 | 4 | 0.300 |
| 4.87 | 0 | 2.500 | 4.87 | 2 | 2.500 | 76.27 | 19 | 0.190 |
| 6.08 | 0 | 2.000 | 6.08 | 3 | 2.000 | 114.41 | 33 | 0.120 |
| 7.61 | 0 | 1.600 | 7.61 | 4 | 1.600 | 152.55 | 39 | 0.090 |
| 9.51 | 0 | 1.280 | 9.51 | 6 | 1.280 | 190.69 | 42 | 0.070 |
| 11.88 | 0 | 1.025 | 11.88 | 10 | 1.025 | 228.82 | 43 | 0.060 |
| 14.91 | 0 | 0.820 | 14.91 | 16 | 0.820 | | | |
| 18.53 | 1 | 0.655 | 18.53 | 25 | 0.655 | | | |
| 23.23 | 4 | 0.524 | 23.23 | 34 | 0.524 | | | |
| 29.01 | 7 | 0.419 | 29.01 | 44 | 0.419 | | | |
| 36.26 | 19 | 0.336 | 36.26 | 50 | 0.336 | | | |
| 45.39 | 34 | 0.268 | 45.39 | 55 | 0.268 | | | |
| 56.67 | 48 | 0.215 | 56.67 | 60 | 0.215 | | | |
| 70.90 | 55 | 0.172 | 70.90 | 65 | 0.172 | | | |
| 88.63 | 60 | 0.138 | 88.63 | 68 | 0.138 | | | |
| 110.79 | 64 | 0.110 | 110.79 | 71 | 0.110 | | | |
| 138.45 | 69 | 0.088 | 138.45 | 75 | 0.088 | | | |
| 172.96 | 73 | 0.071 | 172.96 | 77 | 0.071 | | | |
| 216.33 | 76 | 0.057 | 216.33 | 80 | 0.057 | | | |
| 270.32 | 78 | 0.045 | 270.32 | 82 | 0.045 | | | |
| 338.00 | 80 | 0.036 | 338.00 | 84 | 0.036 | | | |
| 422.46 | 81 | 0.029 | 422.46 | 85 | 0.029 | | | |
| 528.01 | 83 | 0.023 | 528.01 | 87 | 0.023 | | | |
| 660.02 | 85 | 0.019 | 660.02 | 88 | 0.019 | | | |
| 825.05 | 87 | 0.015 | 825.05 | 90 | 0.015 | | | |
| 1031.32 | 89 | 0.012 | 1031.32 | 91 | 0.012 | | | |
| 1289.15 | 90 | 0.010 | 1289.15 | 92 | 0.010 | | | |
| 1611.43 | 91 | 0.008 | 1611.43 | 94 | 0.008 | | | |
| 2014.29 | 92 | 0.006 | 2014.29 | 95 | 0.006 | | | |

Table B-2 Capillary Pressure Data, (Repsol, 2008), Continued

| Reference N° | 86 | | Reference N° | 87 | | Reference N° | 88 | | Reference N° | 90 | |
|--------------------|--------------------|--------------------|--------------------|--------------------|--------------------|--------------------|--------------------|--------------------|--------------------|--------------------|--------------------|
| Porosity | 0.04 | fraction | Porosity | 0.04 | fraction | Porosity | 0.03 | fraction | Porosity | 0.03 | fraction |
| Permeability | 0.04 | mD | Permeability | 0.05 | mD | Permeability | 0.22 | mD | Permeability | 0.02 | mD |
| Capillary Pressure | Mercury Saturation | Pore Throat Radius | Capillary Pressure | Mercury Saturation | Pore Throat Radius | Capillary Pressure | Mercury Saturation | Pore Throat Radius | Capillary Pressure | Mercury Saturation | Pore Throat Radius |
| psia | % | µm | psia | % | µm | psia | % | µm | psia | % | µm |
| 0.06 | 0 | 249.6 | 0.06 | 0 | 249.6 | 0.06 | 0 | 249.6 | 0.06 | 0 | 249.6 |
| 0.17 | 0 | 83.2 | 0.17 | 0 | 83.2 | 0.17 | 0 | 83.2 | 0.17 | 0 | 83.2 |
| 0.34 | 0 | 41.6 | 0.34 | 0 | 41.6 | 0.34 | 0 | 41.6 | 0.34 | 0 | 41.6 |
| 0.72 | 1 | 19.7 | 0.72 | 0 | 19.7 | 0.72 | 0 | 19.7 | 0.72 | 0 | 19.7 |
| 1.20 | 2 | 11.9 | 1.20 | 0 | 11.9 | 1.20 | 0 | 11.9 | 1.20 | 0 | 11.9 |
| 1.68 | 2 | 8.5 | 1.68 | 0 | 8.5 | 1.68 | 0 | 8.5 | 1.68 | 0 | 8.5 |
| 1.96 | 2 | 7.3 | 1.96 | 0 | 7.3 | 1.96 | 0 | 7.3 | 1.96 | 0 | 7.3 |
| 2.48 | 2 | 5.8 | 2.48 | 0 | 5.8 | 2.48 | 0 | 5.8 | 2.48 | 0 | 5.8 |
| 2.86 | 2 | 5.0 | 2.86 | 0 | 5.0 | 2.86 | 0 | 5.0 | 2.86 | 0 | 5.0 |
| 3.81 | 2 | 3.7 | 3.81 | 0 | 3.7 | 3.81 | 0 | 3.7 | 3.81 | 0 | 3.7 |
| 5.72 | 3 | 2.500 | 5.72 | 0 | 2.500 | 5.72 | 0 | 2.500 | 5.72 | 0 | 2.500 |
| 7.63 | 3 | 1.870 | 7.63 | 0 | 1.870 | 7.63 | 0 | 1.870 | 7.63 | 0 | 1.870 |
| 9.53 | 3 | 1.500 | 9.53 | 0 | 1.500 | 9.53 | 0 | 1.500 | 9.53 | 0 | 1.500 |
| 14.30 | 3 | 1.000 | 14.30 | 0 | 1.000 | 14.30 | 0 | 1.000 | 14.30 | 0 | 1.000 |
| 19.07 | 3 | 0.750 | 19.07 | 1 | 0.750 | 19.07 | 0 | 0.750 | 19.07 | 0 | 0.750 |
| 28.60 | 5 | 0.500 | 28.60 | 5 | 0.500 | 28.60 | 1 | 0.500 | 28.60 | 1 | 0.500 |
| 47.67 | 15 | 0.300 | 47.67 | 25 | 0.300 | 47.67 | 3 | 0.300 | 47.67 | 5 | 0.300 |
| 76.27 | 30 | 0.190 | 76.27 | 34 | 0.190 | 76.27 | 16 | 0.190 | 76.27 | 20 | 0.190 |
| 114.41 | 37 | 0.120 | 114.41 | 39 | 0.120 | 114.41 | 41 | 0.120 | 114.41 | 37 | 0.120 |
| 152.55 | 41 | 0.090 | 152.55 | 42 | 0.090 | 152.55 | 49 | 0.090 | 152.55 | 42 | 0.090 |
| 190.69 | 43 | 0.070 | 190.69 | 45 | 0.070 | 190.69 | 51 | 0.070 | 190.69 | 44 | 0.070 |
| 228.82 | 45 | 0.060 | 228.82 | 47 | 0.060 | 228.82 | 52 | 0.060 | 228.82 | 45 | 0.060 |

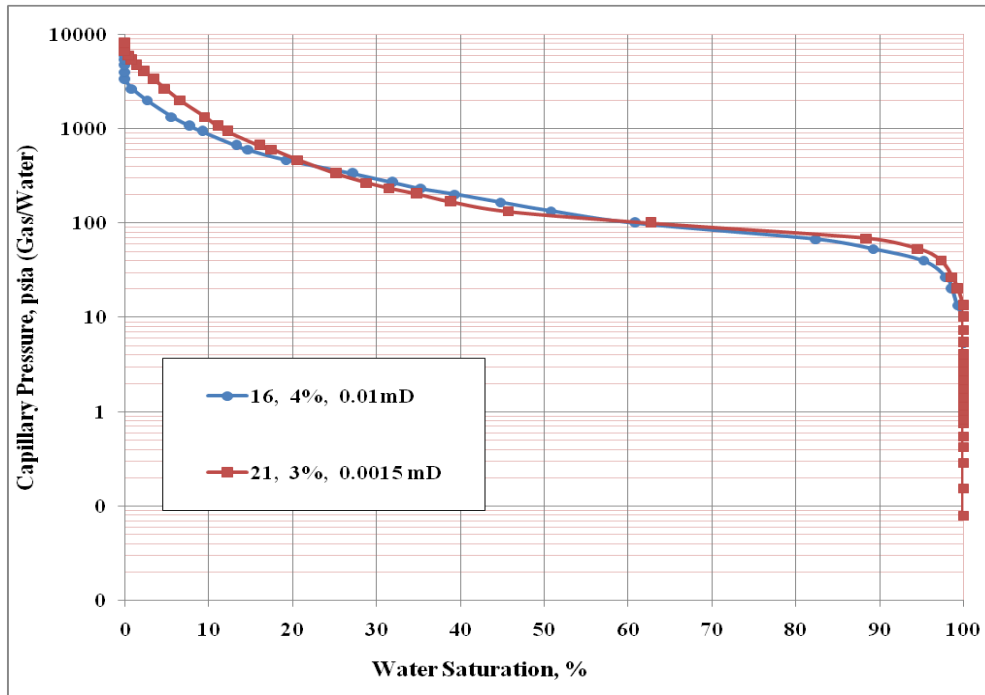


Figure B-1: Well 2 mercury capillary pressure profiles.

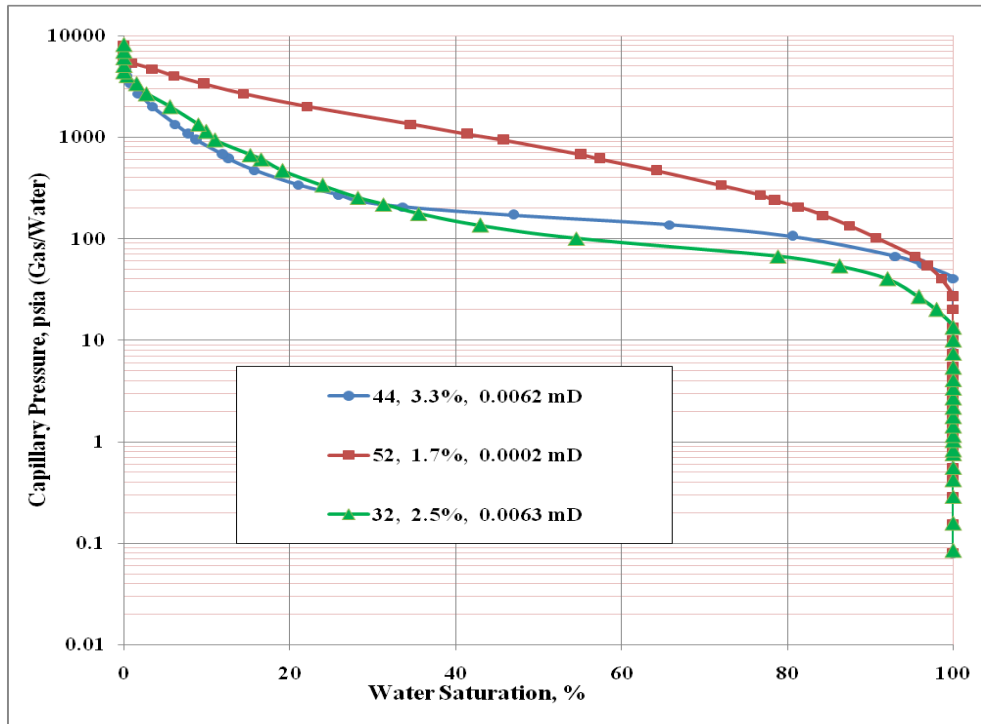


Figure B-2: Well 3 mercury capillary pressure profiles.

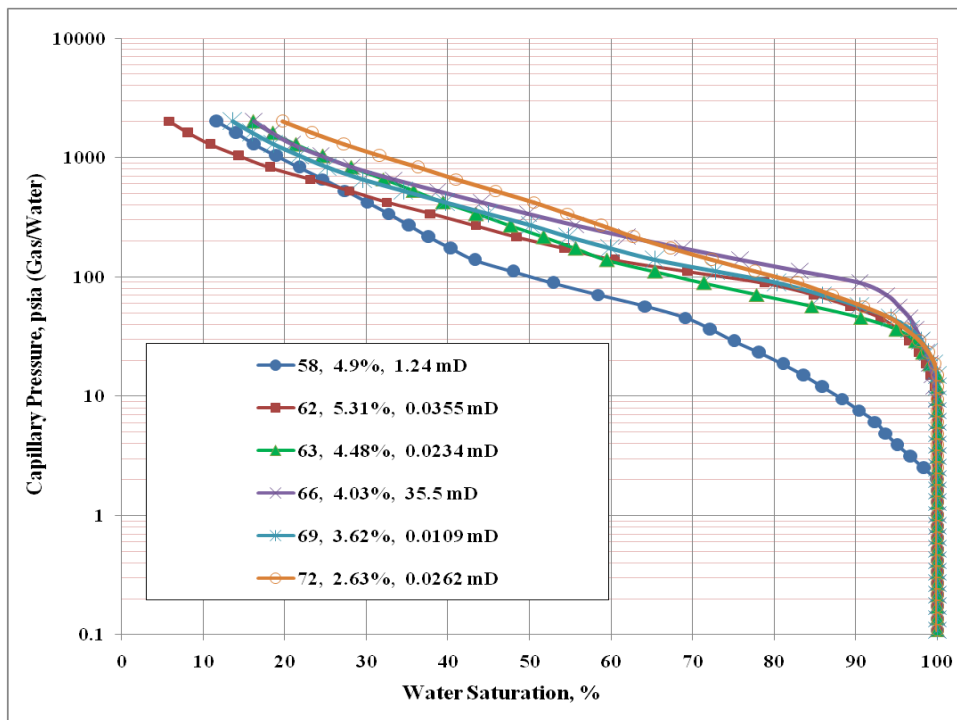


Figure B-3: Well 4 mercury capillary pressure profiles.

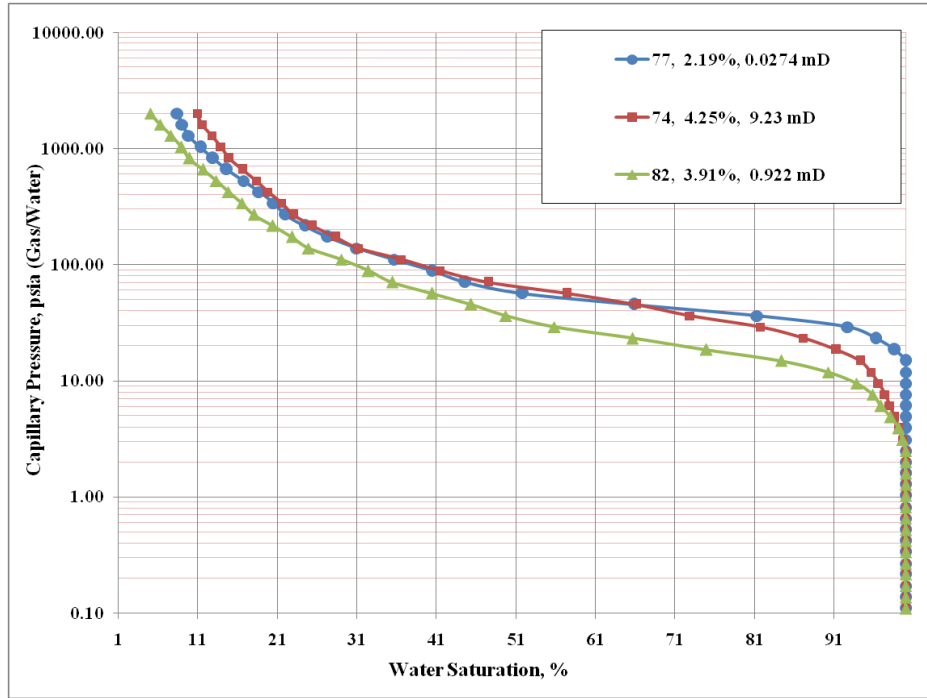


Figure B-5: Well 4ST mercury capillary pressure profiles.

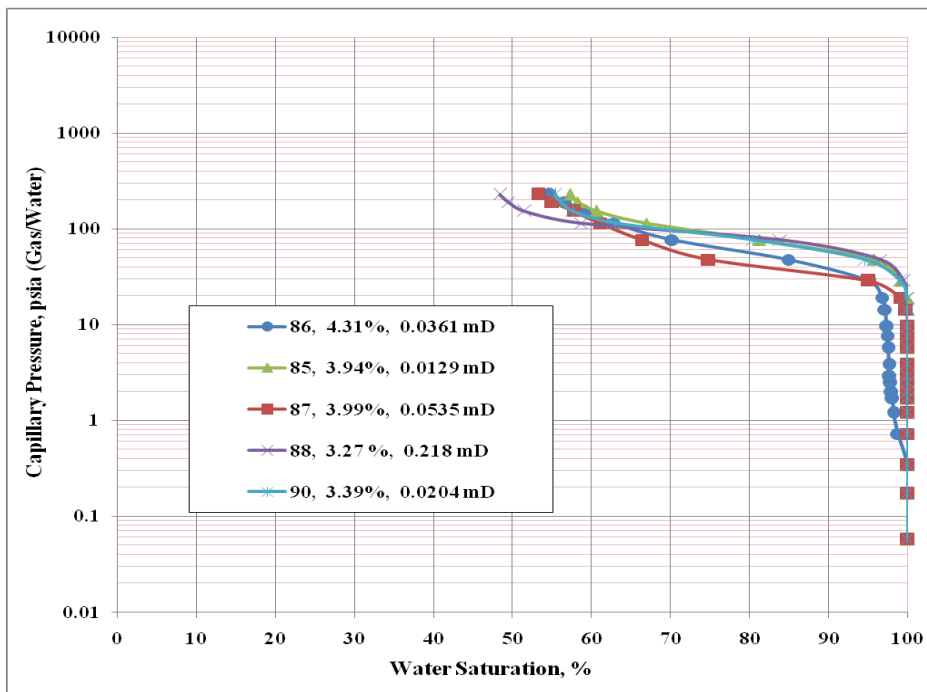


Figure B-6: Well 5 mercury capillary pressure profiles.

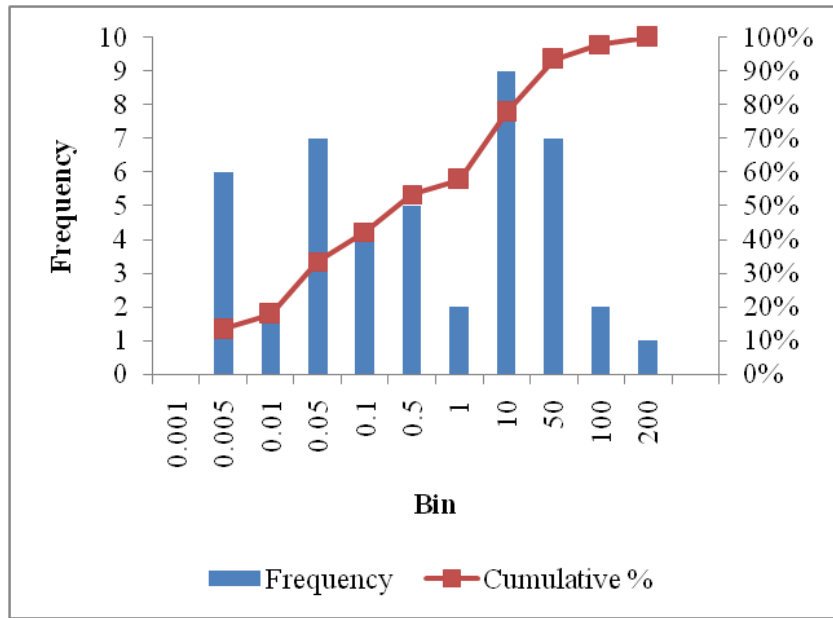


Figure B-7: Well 3 Ref #44 pore throat radius histogram, bin is microns.

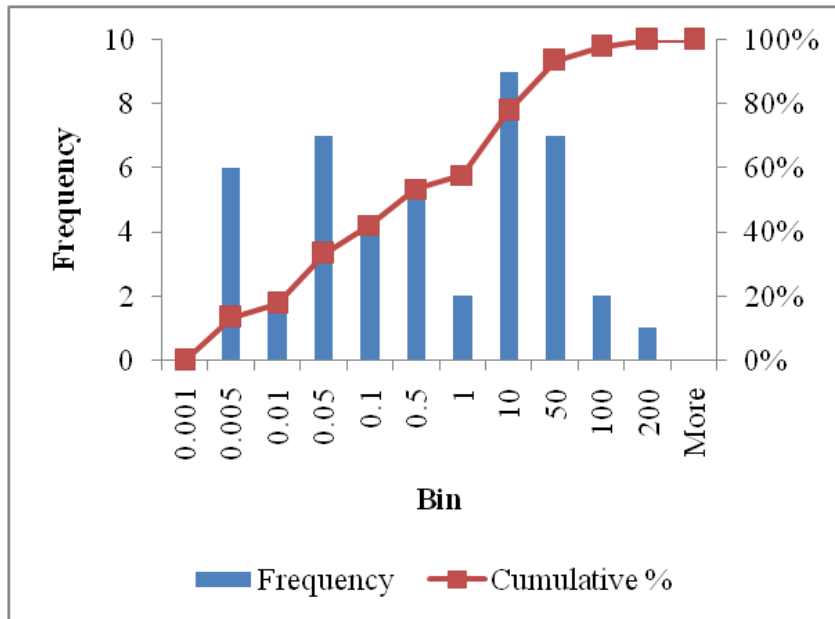


Figure B-8: Well 4 Ref#52 pore throat radius histogram, bin is microns.

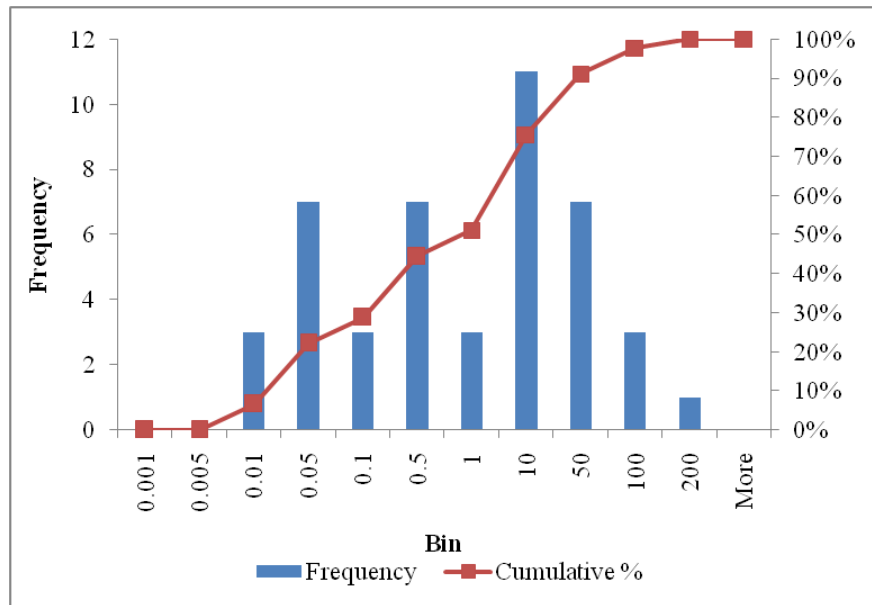


Figure B-9: Well 4 Ref#58 pore throat radius histogram, bin is microns.

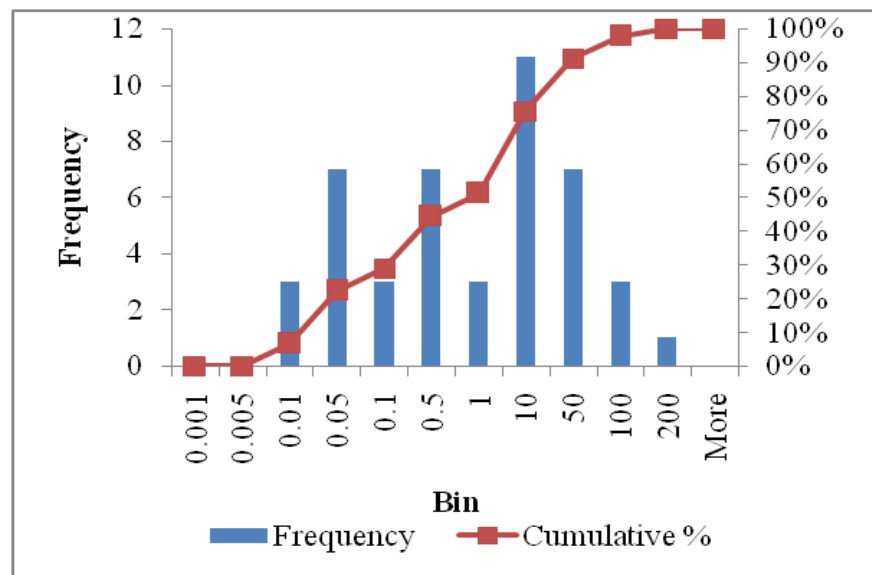


Figure B-10: Well 4 Ref#66 pore throat radius histogram, bin is microns.

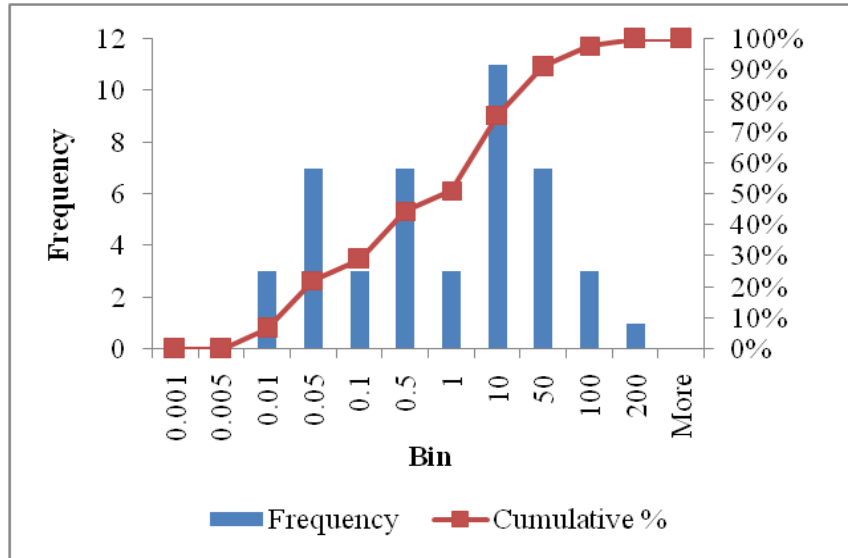


Figure B-11: Well 4 Ref#69 pore throat radius histogram, bin is microns.

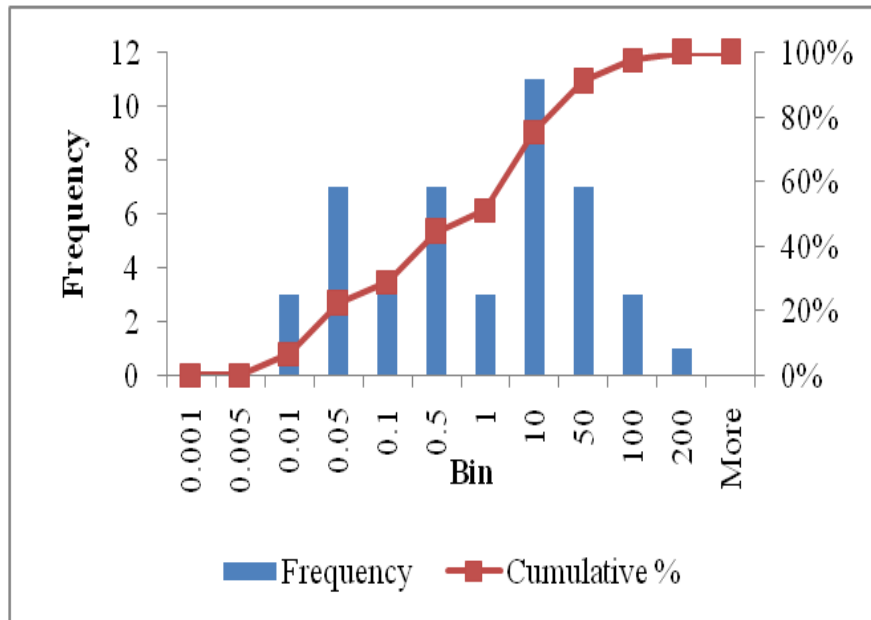


Figure B-12: Well 4ST Ref#74 pore throat radius histogram, bin is microns.

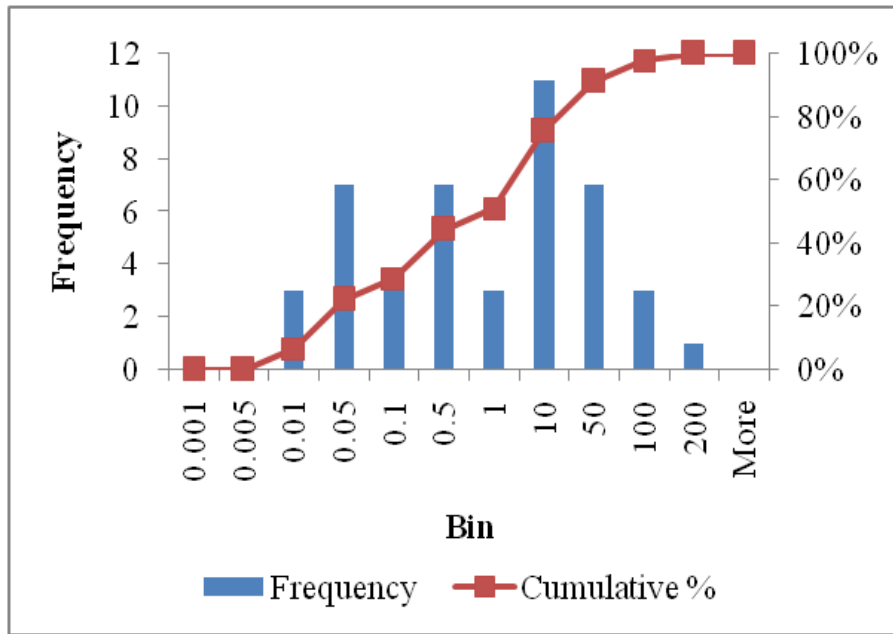


Figure B-13: Well 4ST Ref#82 pore throat radius histogram, bin is microns.

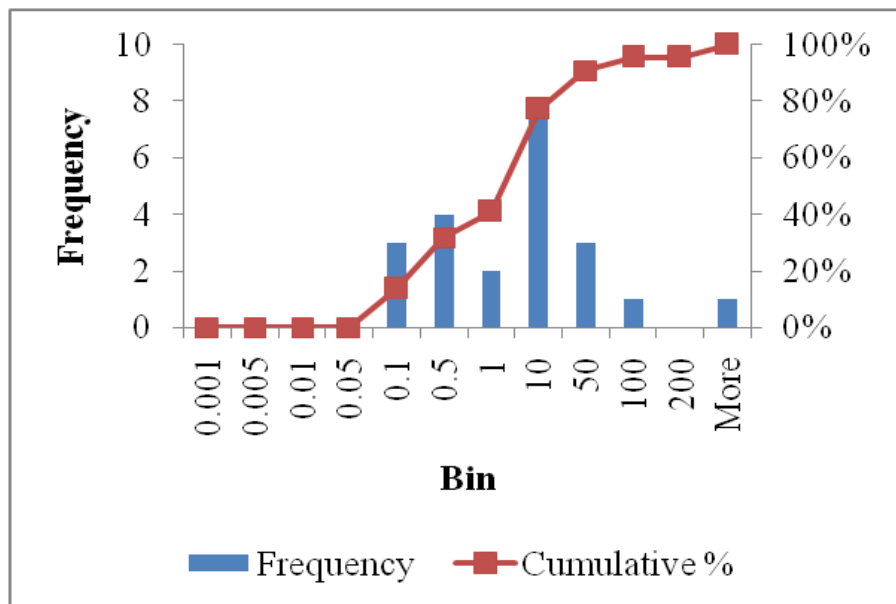


Figure B-14: Well 5 Ref#87 pore throat radius histogram, bin is microns.

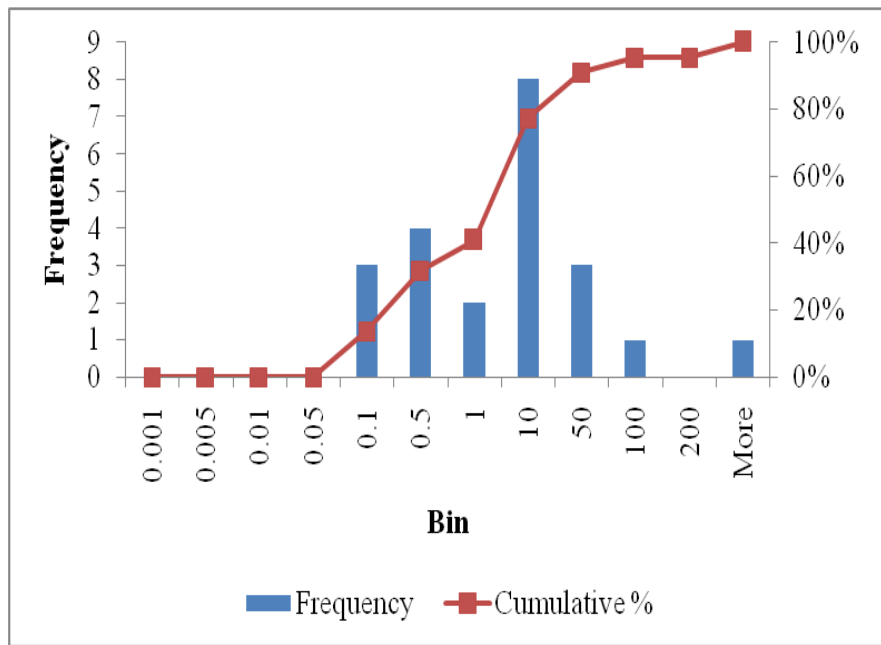


Figure B-15: Well 4 5 Ref#88 pore throat radius histogram, bin is microns.

APPENDIX C

RESULTS FROM PORE SCALE SIMULATION

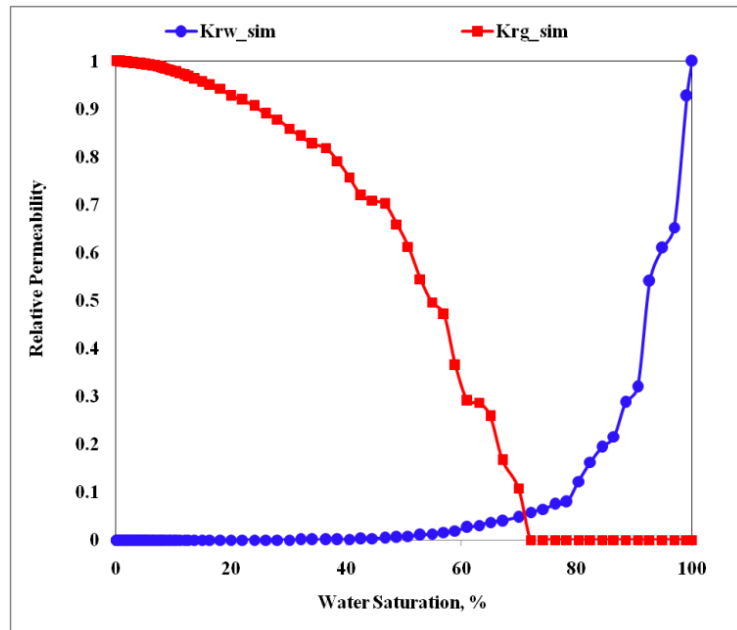


Figure C-1: Well 2 Sample Ref #16 simulated relative permeability curves from capillary pressure calibrated network.

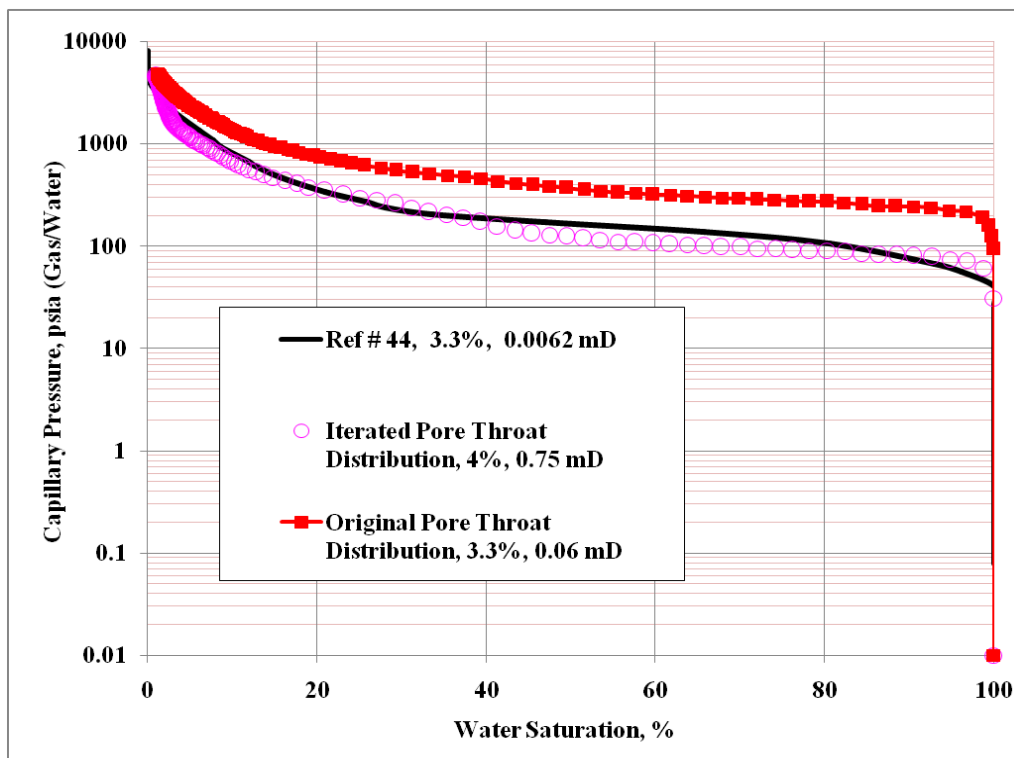


Figure C-2: Well 3 Sample Ref #44 results for capillary pressure curves match.

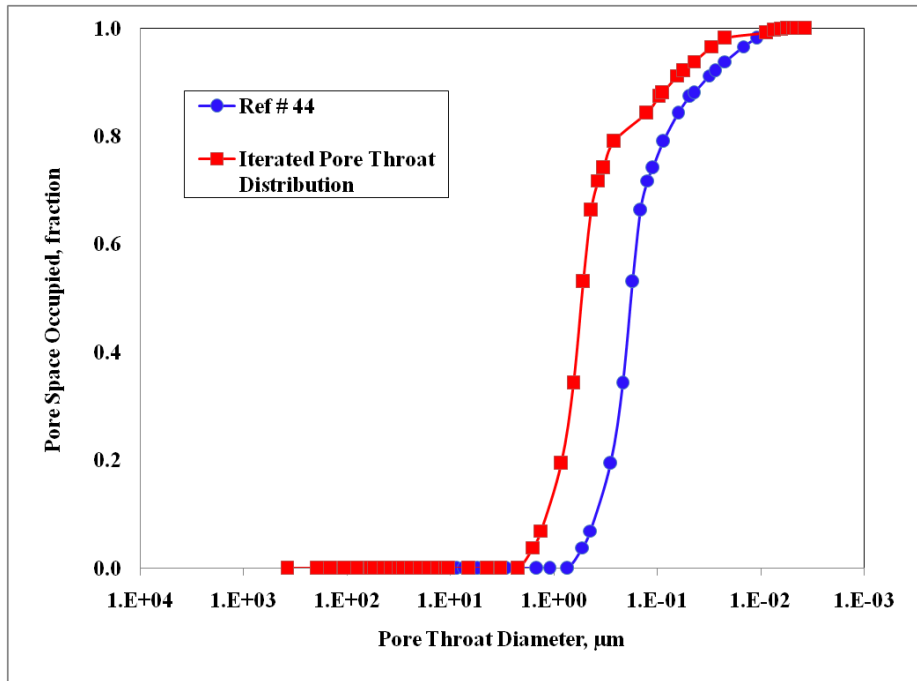


Figure C-3: Well 3 Sample Ref #44 comparison between original and iterated pore throat size distribution.

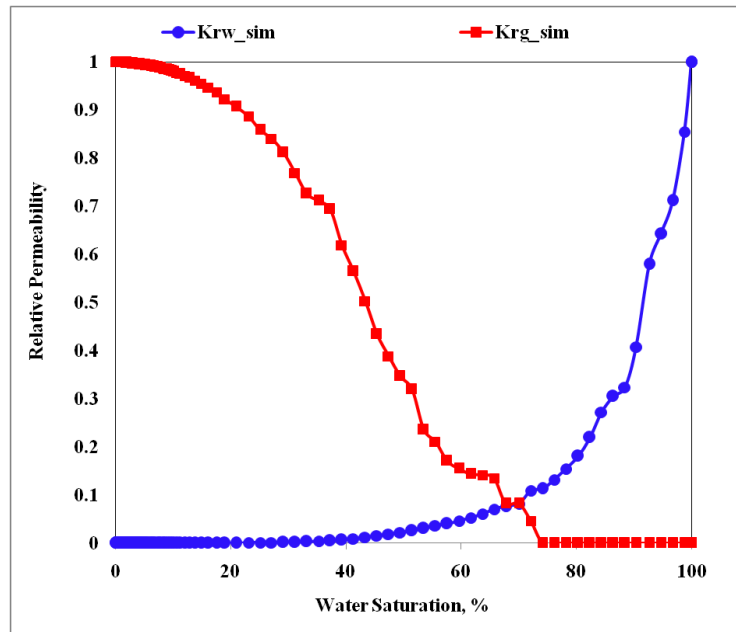


Figure C-4: Well 3 Sample Ref #44 simulated relative permeability curves from capillary pressure calibrated network.

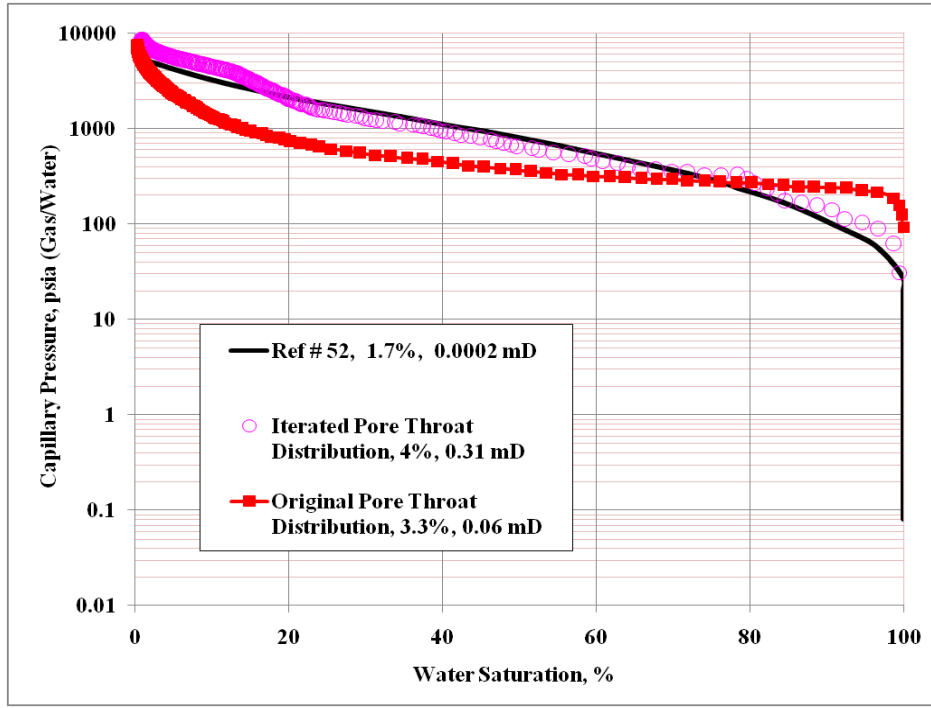


Figure C-5: Well 3 Sample Ref #52 results for capillary pressure curves match.

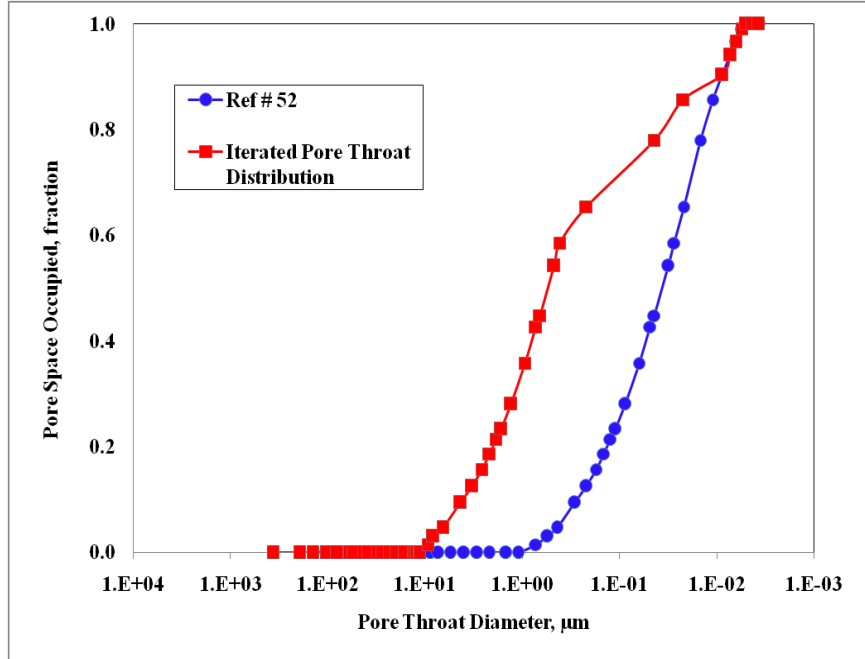


Figure C-6: Well 3 Sample Ref #52 comparison between original and iterated pore throat size distribution.

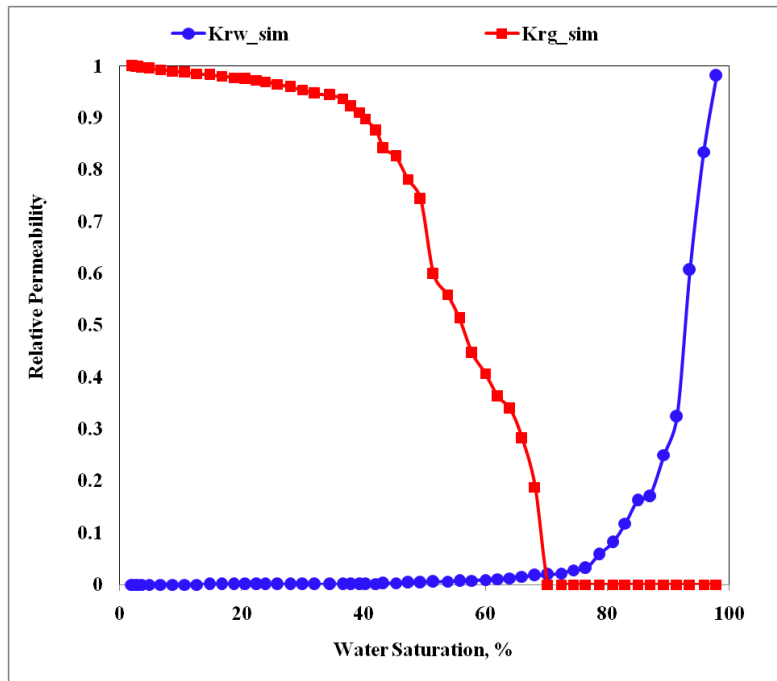


Figure C-7: Well 3 Sample Ref #52 simulated relative permeability curves from capillary pressure calibrated network.

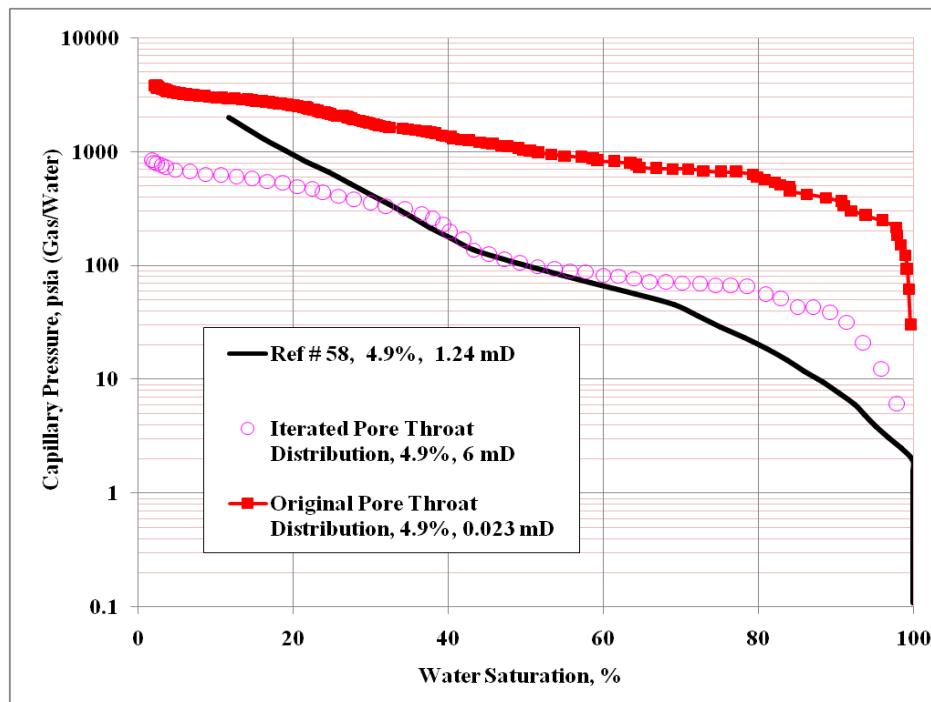


Figure C-8: Well 4 Sample Ref #58 results for capillary pressure curves match.

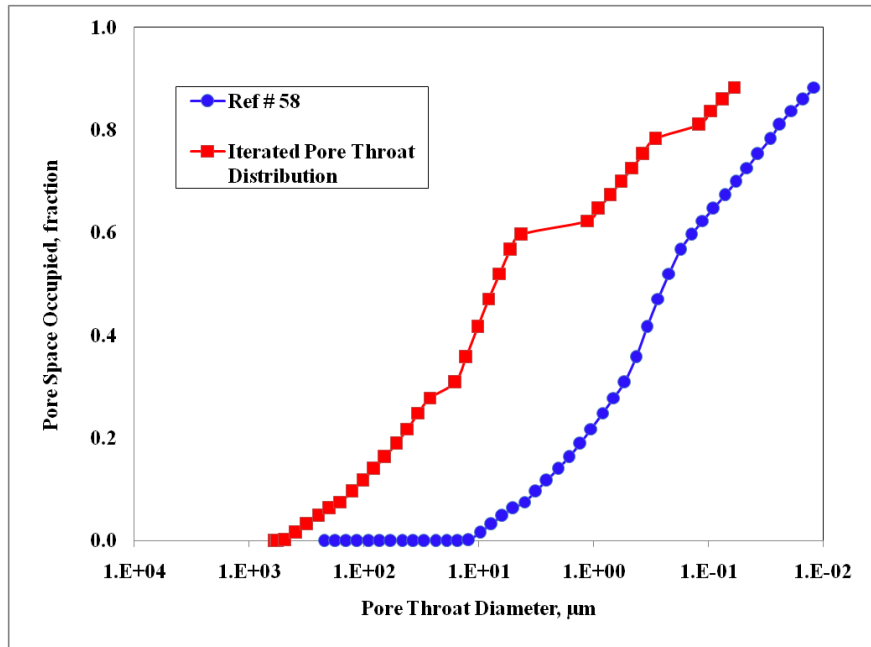


Figure C-9: Well 4 Sample Ref #58 comparison between original and iterated pore throat size distribution.

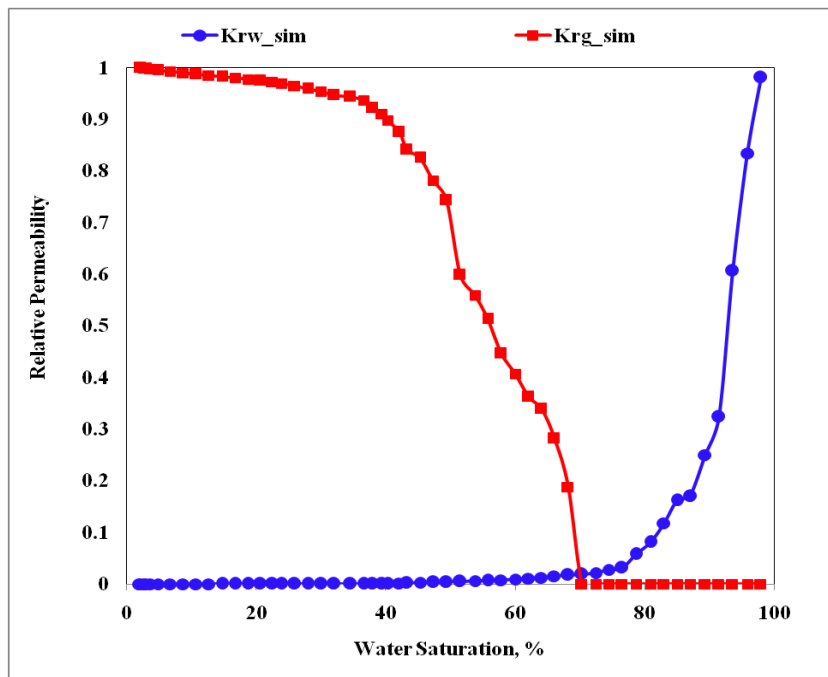


Figure C-10: Well 4 Sample Ref #58 simulated relative permeability curves from capillary pressure calibrated network.

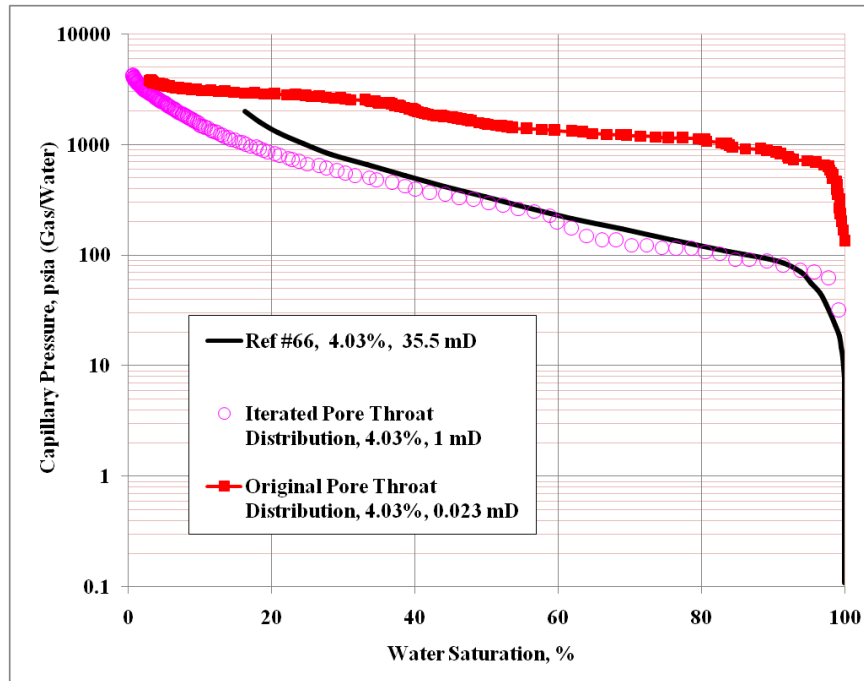


Figure C-11: Well 4 Sample Ref #66 results for capillary pressure curves match.

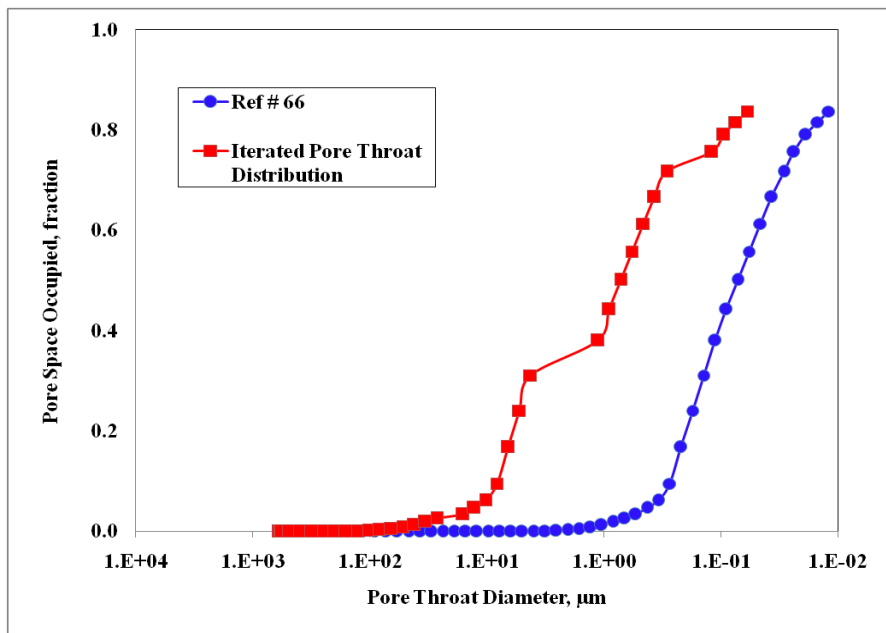


Figure C-12: Well 4 Sample Ref #66 comparison between original and iterated pore throat size distribution.

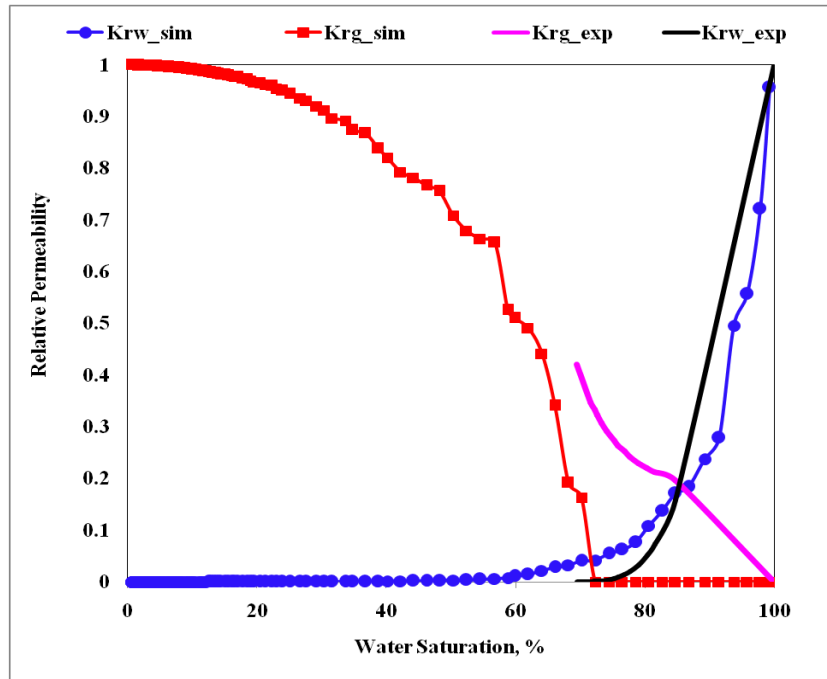


Figure C-13: Well 4 Sample Ref #66 simulated relative permeability curves from capillary pressure calibrated network.

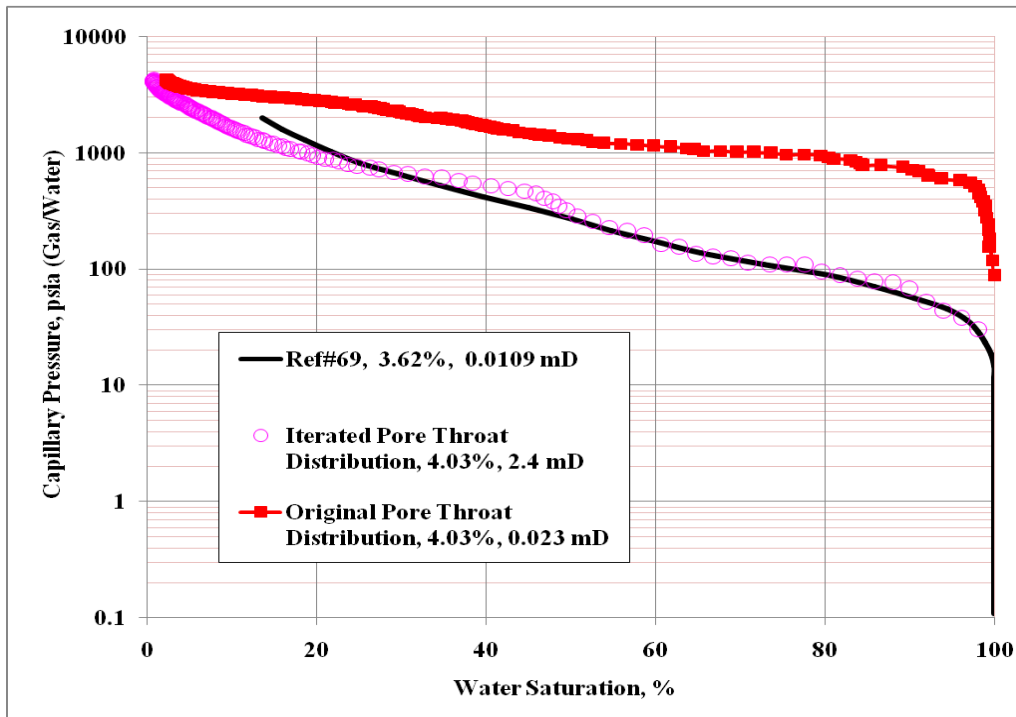


Figure C-14: Well 4ST Sample Ref #69 results for capillary pressure curves match.

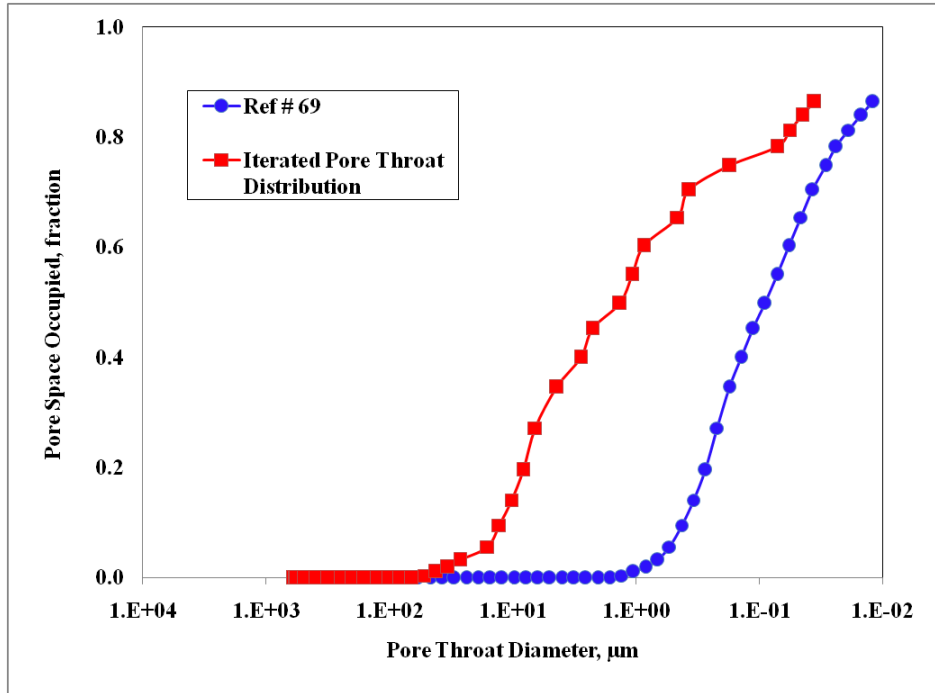


Figure C-15: Well 4ST Sample Ref #69 comparison between original and iterated pore throat size distribution.

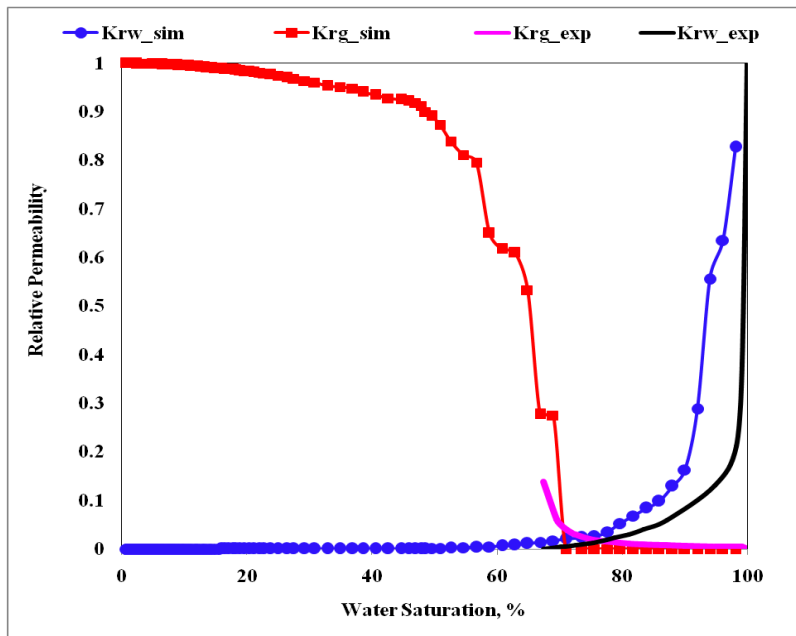


Figure C-16: Well 4ST Sample Ref #69 simulated relative permeability curves from capillary pressure calibrated network.

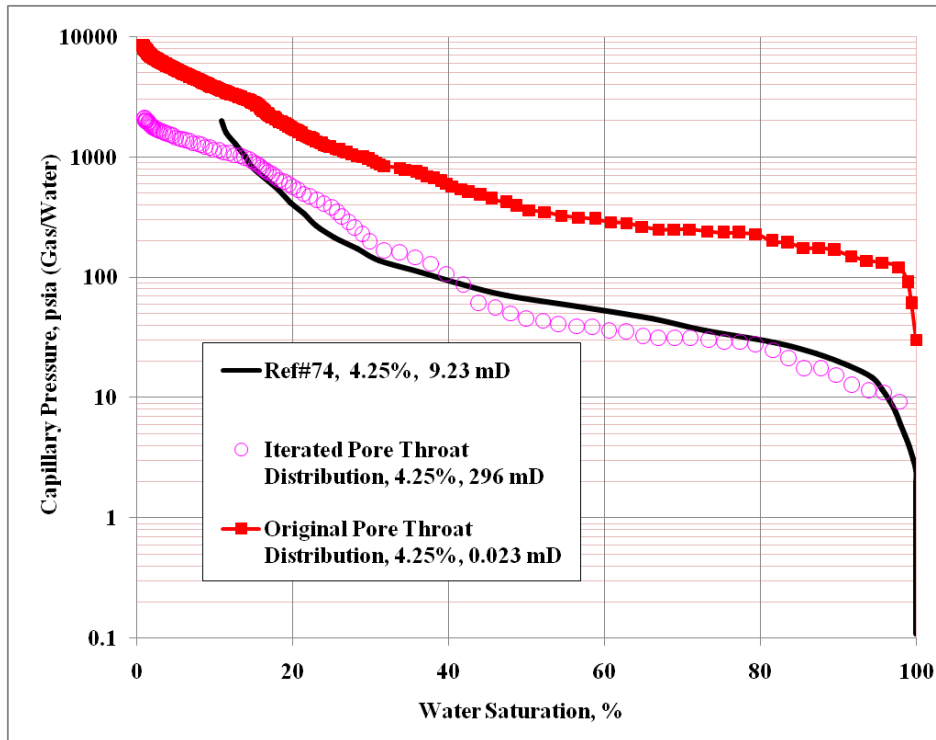


Figure C-17: Well 4ST Sample Ref #74 results for capillary pressure curves match.

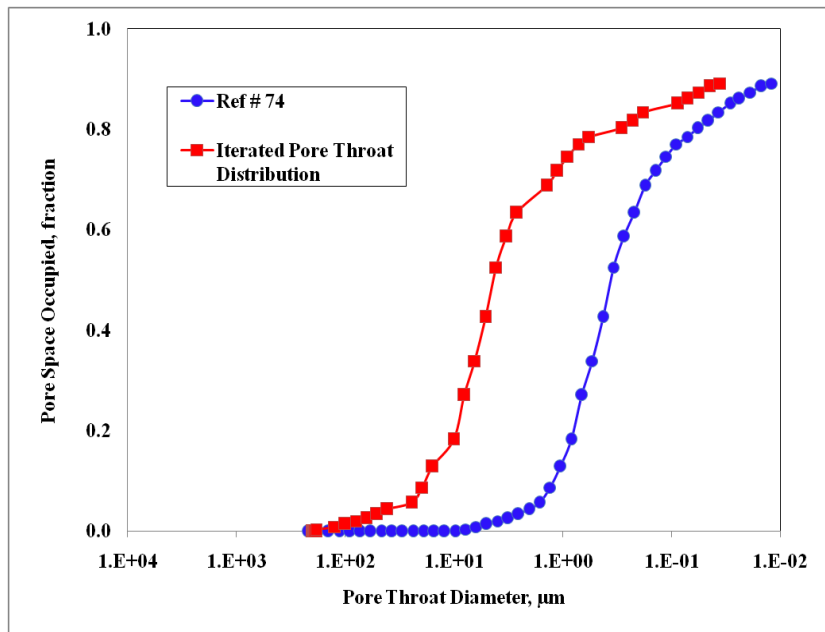


Figure C-18: Well 4ST Sample Ref #74 comparison between original and iterated pore throat size distribution.

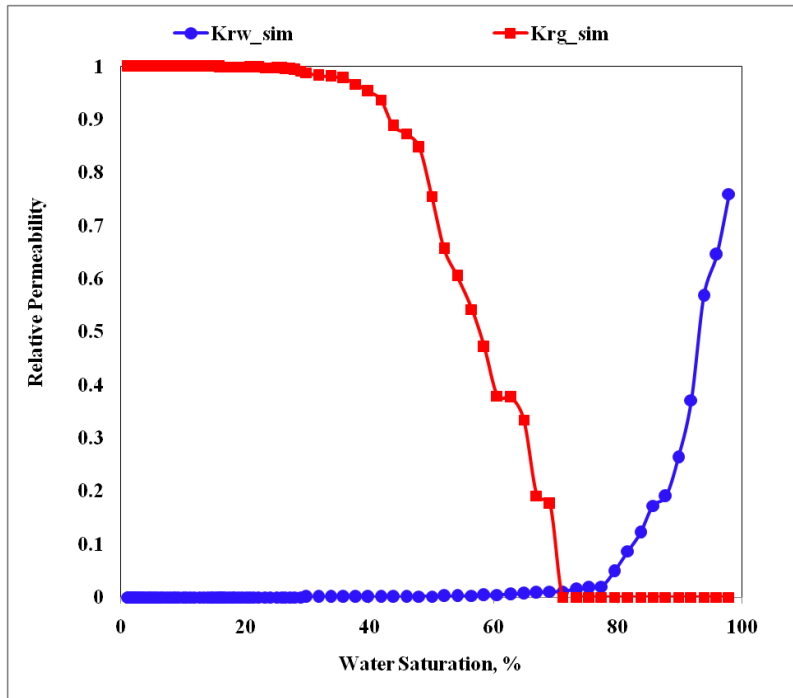


Figure C-19: Well 4ST Sample Ref #74 simulated relative permeability curves from capillary pressure calibrated network.

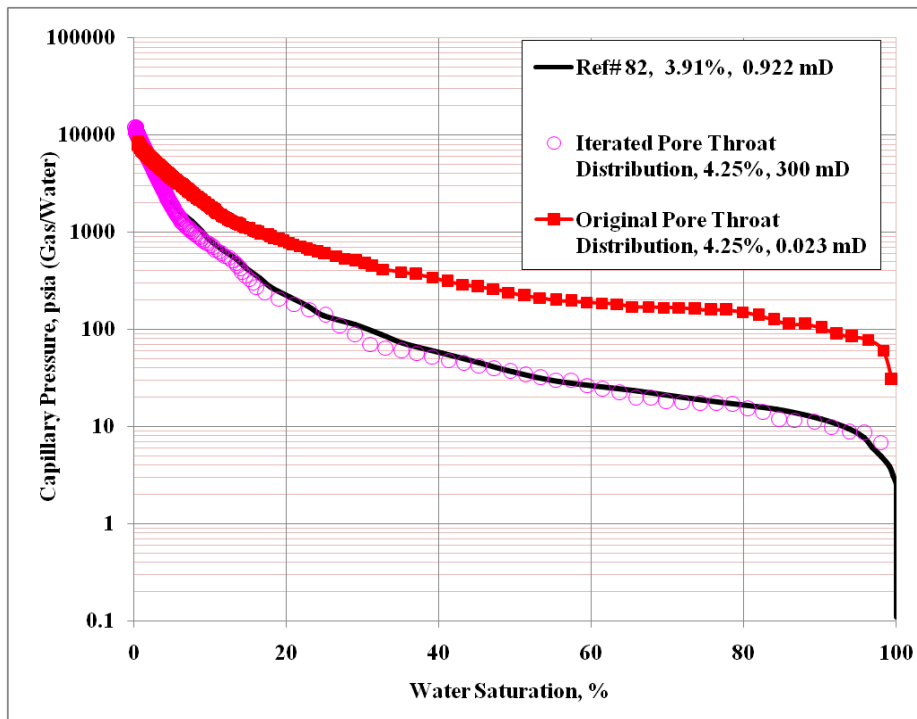


Figure C-20: Well 4ST Sample Ref #82 results for capillary pressure curves match.

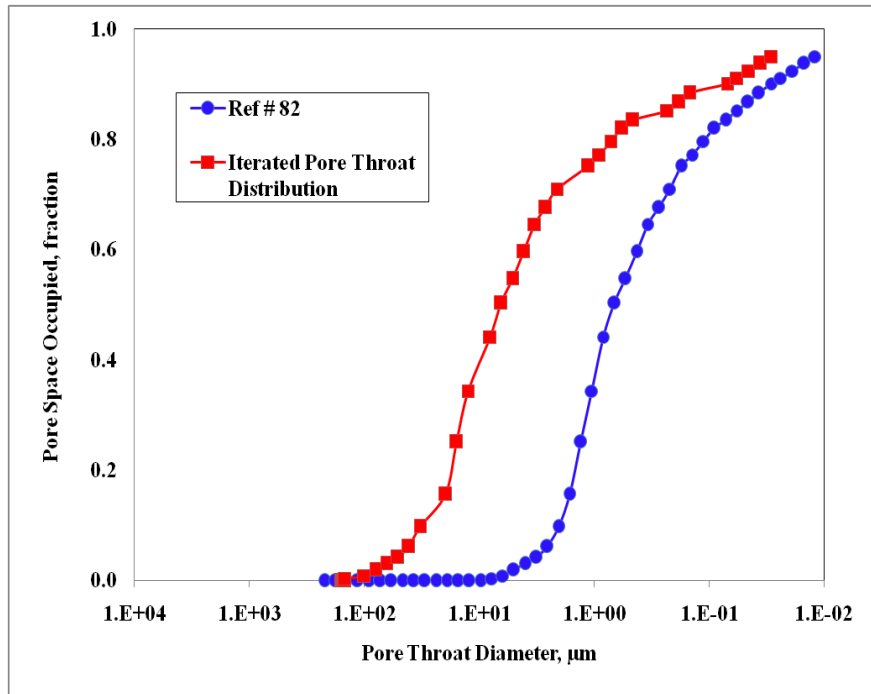


Figure C-21: Well 4ST Sample Ref #82 comparison between original and iterated pore throat size distribution.

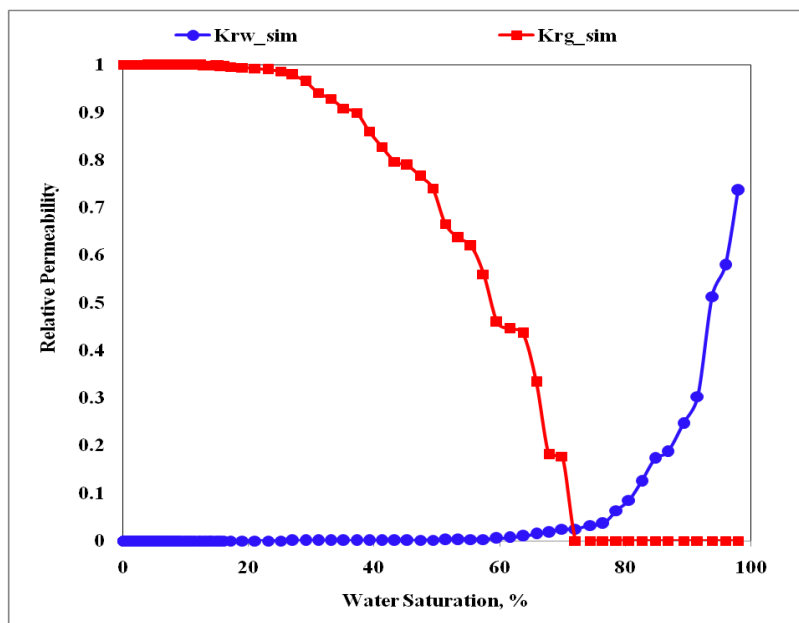


Figure C-22: Well 4ST Sample Ref #82 simulated relative permeability curves from capillary pressure calibrated network.

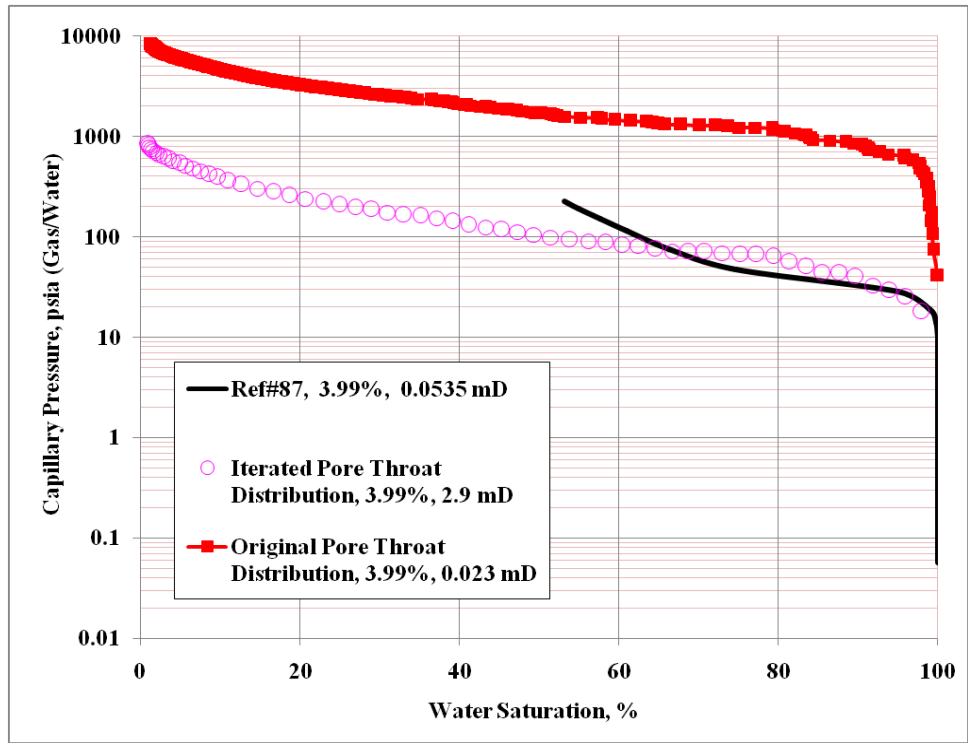


Figure C-23: Well 5 Sample Ref #87 results for capillary pressure curves match.

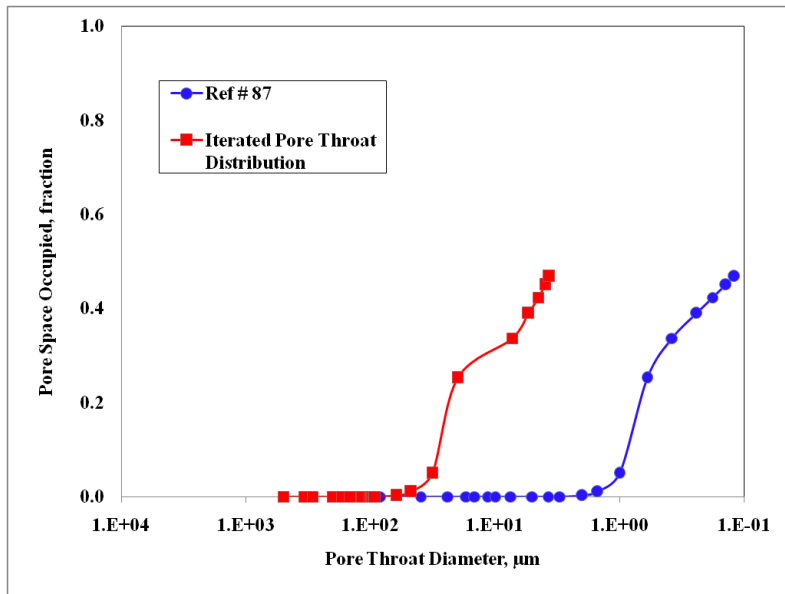


Figure C-24: Well 5 Sample Ref #87 comparison between original and iterated pore throat size distribution.

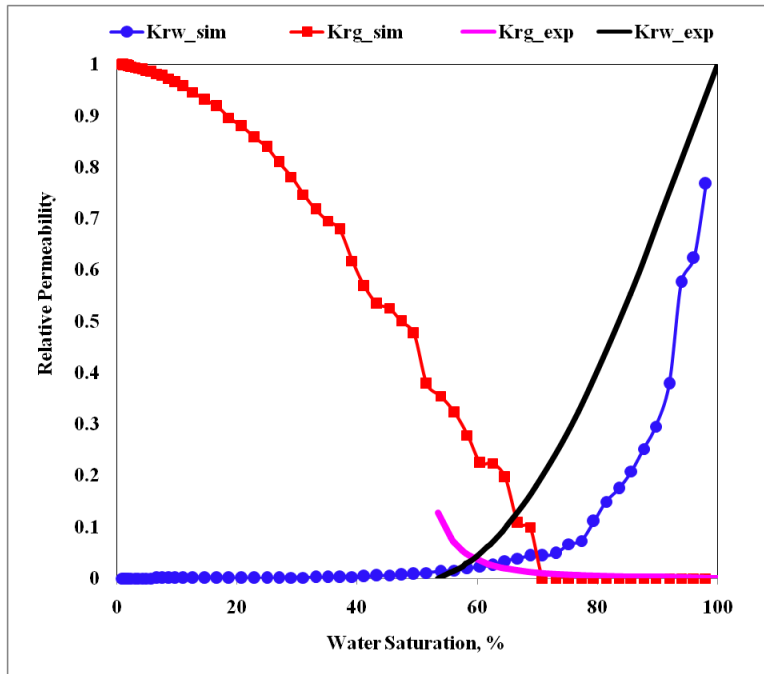


Figure C-25: Well 5 Sample Ref #87 simulated relative permeability curves from capillary pressure calibrated network.

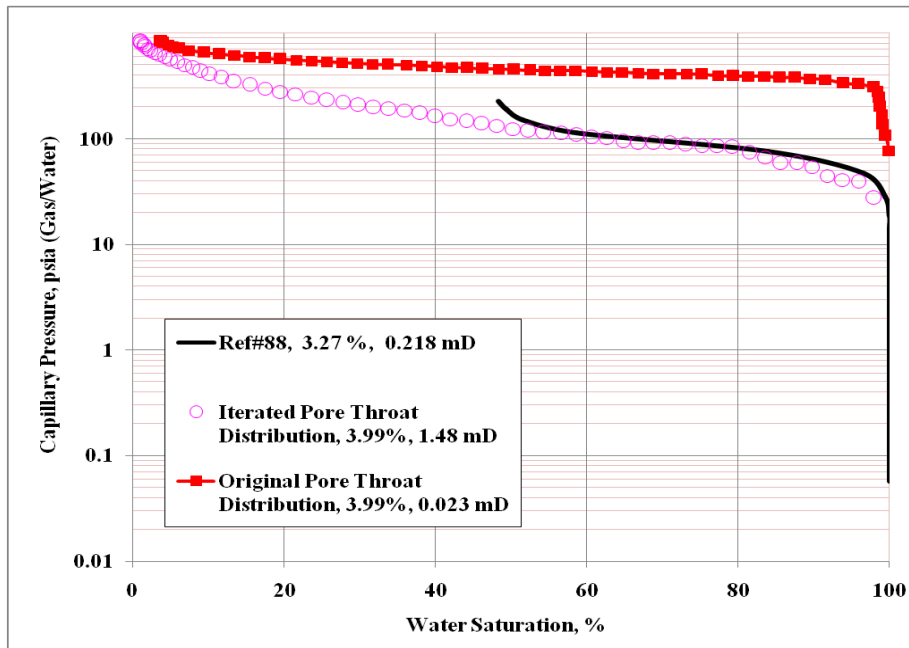


Figure C-26: Well 5 Sample Ref #88 results for capillary pressure curves match.

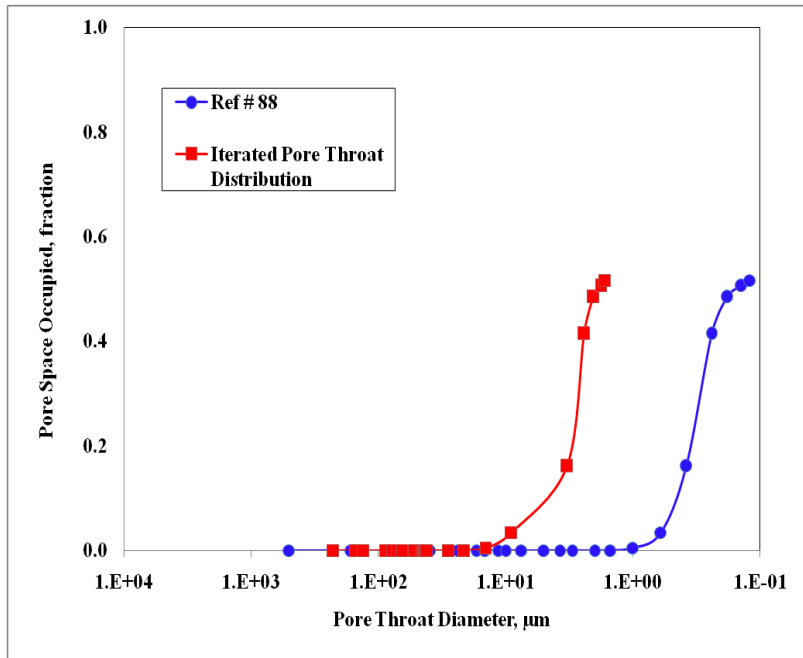


Figure C-27: Well 5 Sample Ref #88 comparison between original and iterated pore throat size distribution.

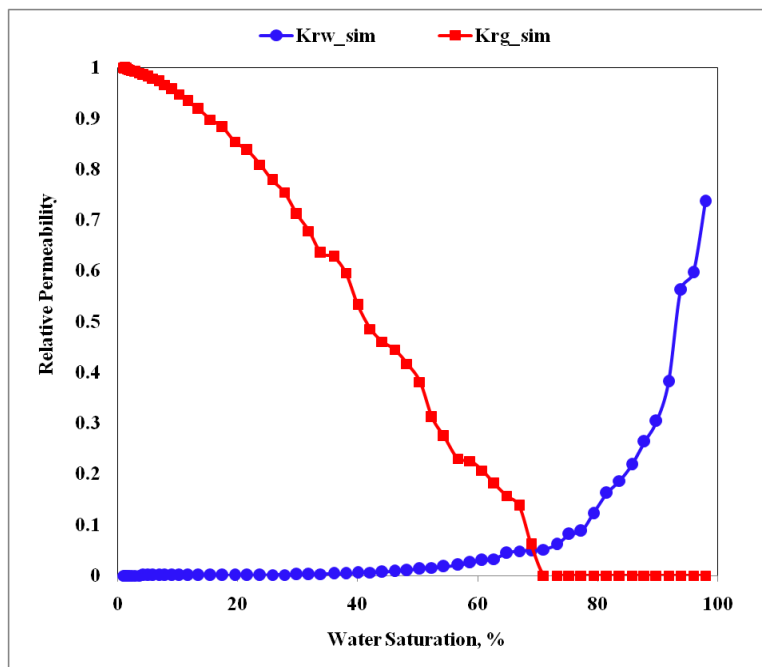


Figure C-28: Well 5 Sample Ref #88 simulated relative permeability curves from capillary pressure calibrated network.

APPENDIX D

LOG ANALYSIS RESULTS

Table D-1: XRD Data Summary (Repsol, 2008)

| Core No | Well No | Sample Name | Grain Density | Quartz | Clay | Others* |
|---------|---------|-------------|--------------------|--------|------|---------|
| | | | gr/cm ³ | % | % | % |
| 1 | Well 1 | 3 | | 89.9 | 3.6 | 6.5 |
| 2 | Well 1 | 2 | 2.64 | 91.7 | 1.8 | 6.5 |
| 3 | Well 1 | 4 | 2.66 | 78.3 | 5.7 | 16 |
| 4 | Well 1 | 11 | 2.70 | 69.3 | 15.9 | 14.8 |
| 5 | Well 1 | 5 | | 79.4 | 7.8 | 12.8 |
| 6 | Well 1 | 6 | 2.70 | 64.1 | 18.5 | 17.4 |
| 7 | Well 1 | 7 | | 46.1 | 5.6 | 48.3 |
| 8 | Well 1 | 8 | | 89.11 | 3.1 | 7.79 |
| 9 | Well 1 | 9 | 2.66 | 79.4 | 6.1 | 14.5 |
| 10 | Well 1 | 10 | 2.71 | 57 | 28 | 15 |
| 11 | Well 2 | 1 | 2.65 | | | |
| 12 | Well 2 | 2 | 2.73 | 67.4 | 6.7 | 25.9 |
| 13 | Well 2 | 11 | 2.65 | 0 | 0 | 0 |
| 14 | Well 2 | 3f | 2.66 | 81.6 | 6.1 | 12.3 |
| 15 | Well 2 | 12f | 2.66 | 0 | 0 | 0 |
| 16 | Well 2 | 4 | 2.67 | 73.6 | 13.6 | 12.8 |
| 17 | Well 2 | 5 | 2.68 | 70.1 | 16.2 | 13.7 |
| 18 | Well 2 | 13 | 2.67 | 0 | 0 | 0 |
| 19 | Well 2 | 7 | 2.66 | 81.1 | 6.3 | 12.6 |
| 20 | Well 2 | 8 | 2.67 | 0 | 0 | 0 |
| 21 | Well 2 | 9 | 2.66 | 0 | 0 | 0 |
| 22 | Well 2 | 14 | 2.66 | 0 | 0 | 0 |
| 23 | Well 2 | 15 | 2.66 | 83.8 | 6.8 | 9.4 |
| 24 | Well 2 | 10 | 2.66 | 82.3 | 4.7 | 13 |
| 25 | Well 3 | 1* | 2.65 | 86.4 | 4.3 | 9.3 |
| 26 | Well 3 | 2 | 2.66 | 90.9 | 3.1 | 6 |
| 27 | Well 3 | 2A | 2.66 | 0 | 0 | 0 |
| 28 | Well 3 | 3 | 2.64 | 90.9 | 3 | 6.1 |
| 29 | Well 3 | 4 | 2.66 | | | |
| 30 | Well 3 | 5* | 2.65 | | | |
| 31 | Well 3 | 6* | 2.64 | | | |
| 32 | Well 3 | 7 | 2.64 | | | |
| 33 | Well 3 | 8+ | 2.65 | 92.2 | 2.5 | 5.3 |
| 34 | Well 3 | 9 | 2.67 | 90.1 | 2.5 | 7.4 |
| 35 | Well 3 | 1* | 2.64 | 90.5 | 3.9 | 5.6 |
| 36 | Well 3 | 2** | - | 45.3 | 41.8 | 12.9 |
| 37 | Well 3 | 1 | 2.64 | | | |
| 38 | Well 3 | 1 | 2.65 | | | |
| 39 | Well 3 | 2 | 2.66 | 89.8 | 2.8 | 7.4 |
| 40 | Well 3 | 3 | 2.65 | | | |
| 41 | Well 3 | 4* | 2.67 | 86.4 | 1.8 | 11.8 |
| 42 | Well 3 | 5 | 2.65 | | | |
| 43 | Well 3 | 6* | 2.65 | 90.1 | 2.4 | 7.5 |
| 44 | Well 3 | 7 | 2.65 | 87.1 | 3.4 | 9.5 |
| 45 | Well 3 | 8 | 2.66 | | | |
| 46 | Well 3 | 9 | 2.67 | 85.3 | 2 | 12.7 |
| 47 | Well 3 | 10 | 2.67 | | | |
| 48 | Well 3 | 11 | 2.69 | 74.2 | 2.6 | 23.2 |
| 49 | Well 3 | 12 | 2.74 | 53.3 | 28.3 | 18.4 |
| 50 | Well 3 | 13 | 2.75 | | | |
| 51 | Well 3 | 14 | 2.73 | 52.7 | 29.3 | 18 |
| 52 | Well 3 | 15 | 2.73 | | | |
| 53 | Well 3 | 16 | 2.70 | 57.5 | 27.4 | 15.1 |
| 54 | Well 3 | 17 | 2.73 | 58.1 | 25.9 | 16 |
| 55 | Well 3 | 18 | 2.72 | | | |
| 56 | Well 4 | 4-1-3-1 F | 2.69 | | | |
| 57 | Well 4 | 4-1-3-2 F | 2.70 | 79 | 6 | 15 |
| 58 | Well 4 | 4-1-3-3 F | 2.71 | | | |
| 59 | Well 4 | 4-1-3-4 F | 2.68 | 79 | 6 | 15 |
| 60 | Well 4 | 4-1-3-5 M | 2.68 | | | |

Table D-1: XRD Data Summary (Repsol, 2008), Continued

| Core No | Well No | Sample Name | Grain Density | Quartz | Clay | Others* |
|---------|----------|---------------|--------------------|--------|------|---------|
| | | | gr/cm ³ | % | % | % |
| 61 | Well 4 | 4-1-3-6 M | 2.68 | | | |
| 62 | Well 4 | 4-1-2-7 F | 2.71 | | | |
| 63 | Well 4 | 4-1-2-8 M | 2.72 | 66 | 15 | 19 |
| 64 | Well 4 | 4-1-2-9 M | 2.69 | | | |
| 65 | Well 4 | 4-1-2-10 M | 2.69 | 74 | 12 | 14 |
| 66 | Well 4 | 4-1-2-11 F | 2.70 | | | |
| 67 | Well 4 | 4-1-2-12 F | 2.70 | | | |
| 68 | Well 4 | 4-1-1-13 F | 2.70 | | | |
| 69 | Well 4 | 4-1-1-14 M | 2.68 | 78 | 7 | 15 |
| 70 | Well 4 | 4-1-1-16 M | 2.67 | | | |
| 71 | Well 4 | 4-1-1-17 F | 2.69 | | | |
| 72 | Well 4 | 4-1-1-18 F | 2.70 | | | |
| 73 | Well 4ST | 4 ST 1-4-1 F | 2.67 | | | |
| 74 | Well 4ST | 4 ST 1-4-2 F | 2.64 | 89 | 2 | 9 |
| 75 | Well 4ST | 4 ST 1-4-3 M | 2.63 | | | |
| 76 | Well 4ST | 4 ST 1-3-4M | 2.63 | | | |
| 77 | Well 4ST | 4 ST 1-3-5M | 2.63 | 87 | 2 | 11 |
| 78 | Well 4ST | 4 ST 1-2-6 F | 2.63 | | | |
| 79 | Well 4ST | 4 ST 1-2-7 F | 2.64 | 88 | 2 | 10 |
| 80 | Well 4ST | 4 ST 1-2-8 F | 2.66 | | | |
| 81 | Well 4ST | 4 ST 1-2-9 F | 2.64 | 86 | 2 | 12 |
| 82 | Well 4ST | 4 ST 1-1-10 M | 2.65 | 87 | 2 | 11 |
| 83 | Well 4ST | 4 ST 1-1-11 F | 2.67 | | | |
| 84 | Well 5 | 1-2-1F | 2.65 | 80 | 5 | 15 |
| 85 | Well 5 | 1-2-2 | 2.67 | | | |
| 86 | Well 5 | 1-2-3 | 2.66 | | | |
| 87 | Well 5 | 1-2-4F | 2.66 | 84 | 2 | 12 |
| 88 | Well 5 | 1-2-5 | 2.65 | | | |
| 90 | Well 5 | 1-1-7 | 2.67 | 0.86 | 0.02 | 0.12 |

Notes.- * other minerals include: Feldspar, Calcite, Siderite, Mica and Pyrite . Pyrite traces are seen ranging from 0.1 to 0.4 %. Percentages are given in weight percent. In industry the grain density is known as real density and the density of fluids and grain is known as apparent density (bulk density). Well 1 to Well 3 core reports provide grain density values and Wells 4, 4ST and 5 recorded real and apparent density . It is expected that the apparent density > real density. In this study the real density values for Well 4, 4ST and 5 are considered grain density.

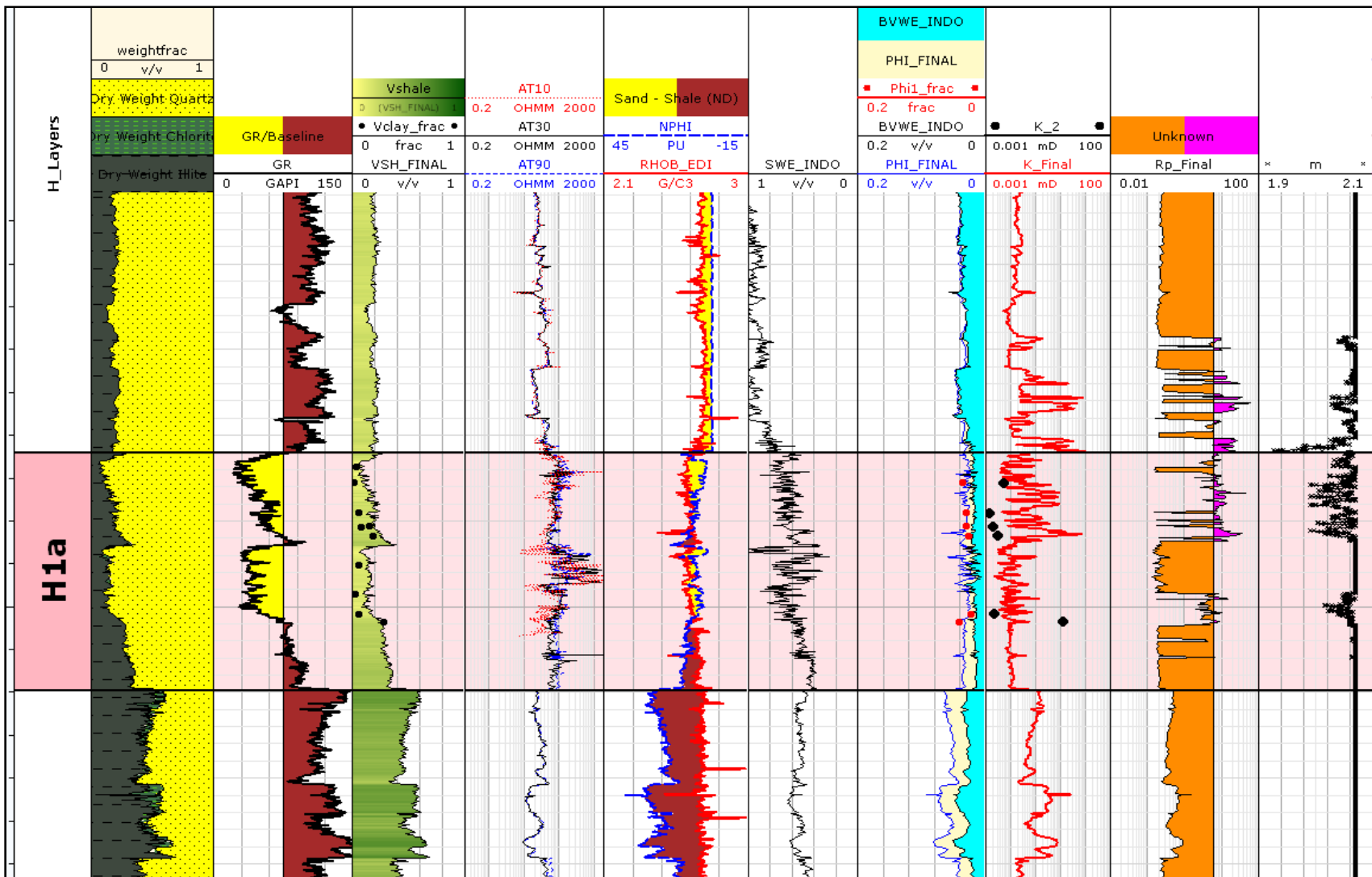


Figure D-1: Well1 Log plot to summarize log derived petrophysical properties. Track 1: Lithology Track 2: Gamma ray, API Track 3: Volume of shale, fraction Track 4: Resistivity, Ohmm Track 5: Neutron-density Track 6: Water saturation, fraction Track 7: Porosity-water saturation Track 8: Permeability, mD Track 9: Pore throat radius, microns Track 10: Cementation exponent, unitless. Dots show available core data in the porosity and permeability tracks.

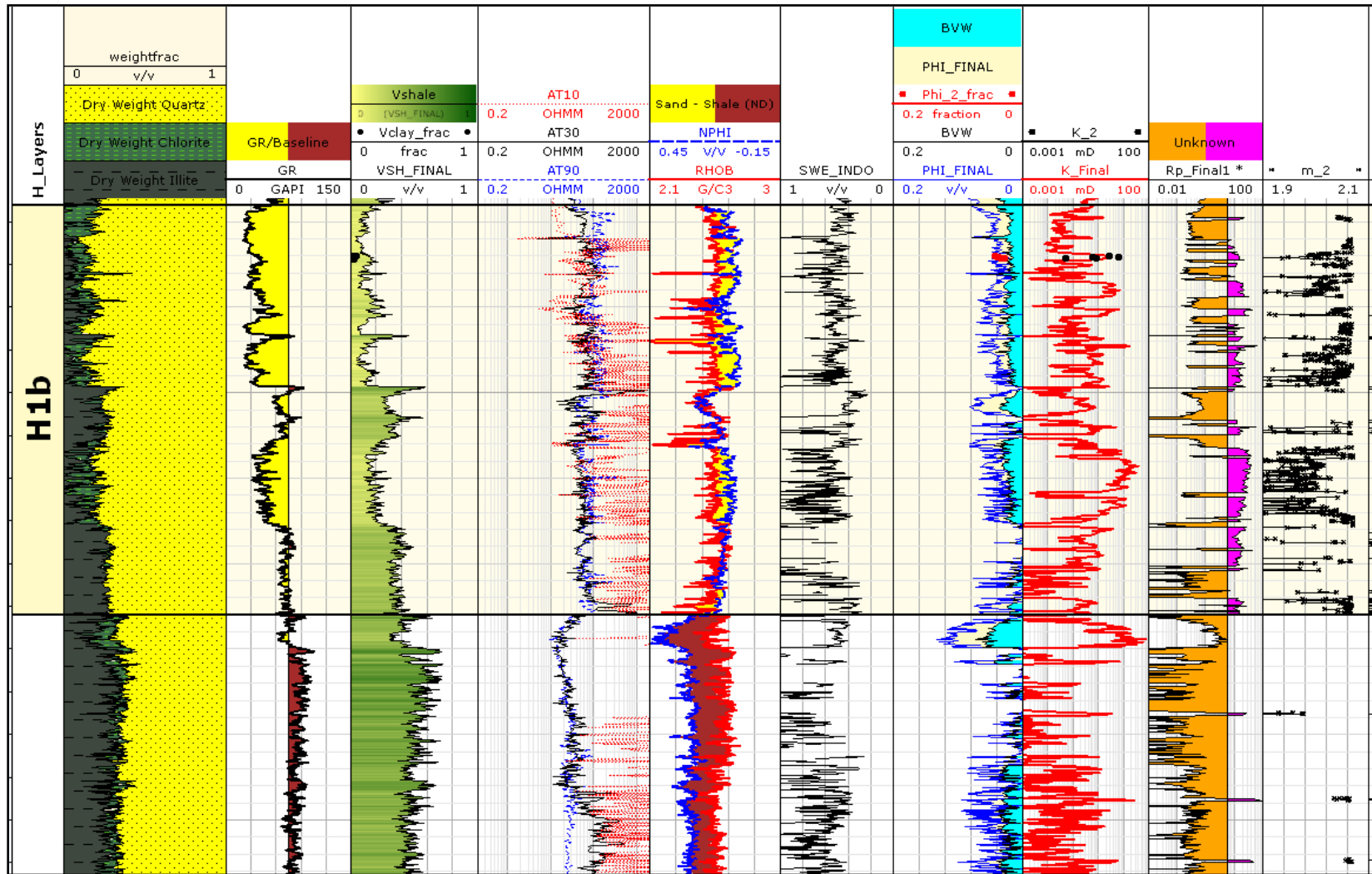


Figure D-2: Well 3 Log plot to summarize log derived petrophysical properties. Track 1: Lithology Track 2: Gamma ray, API Track 3: Volume of shale, fraction Track 4: Resistivity, Ohmm Track 5: Neutron-density Track 6: Water saturation, fraction Track 7: Porosity-water saturation Track 8: Permeability, mD Track 9: Pore throat radius, microns Track 10: Cementation exponent, unitless. Dots show available core data in the porosity and permeability tracks.

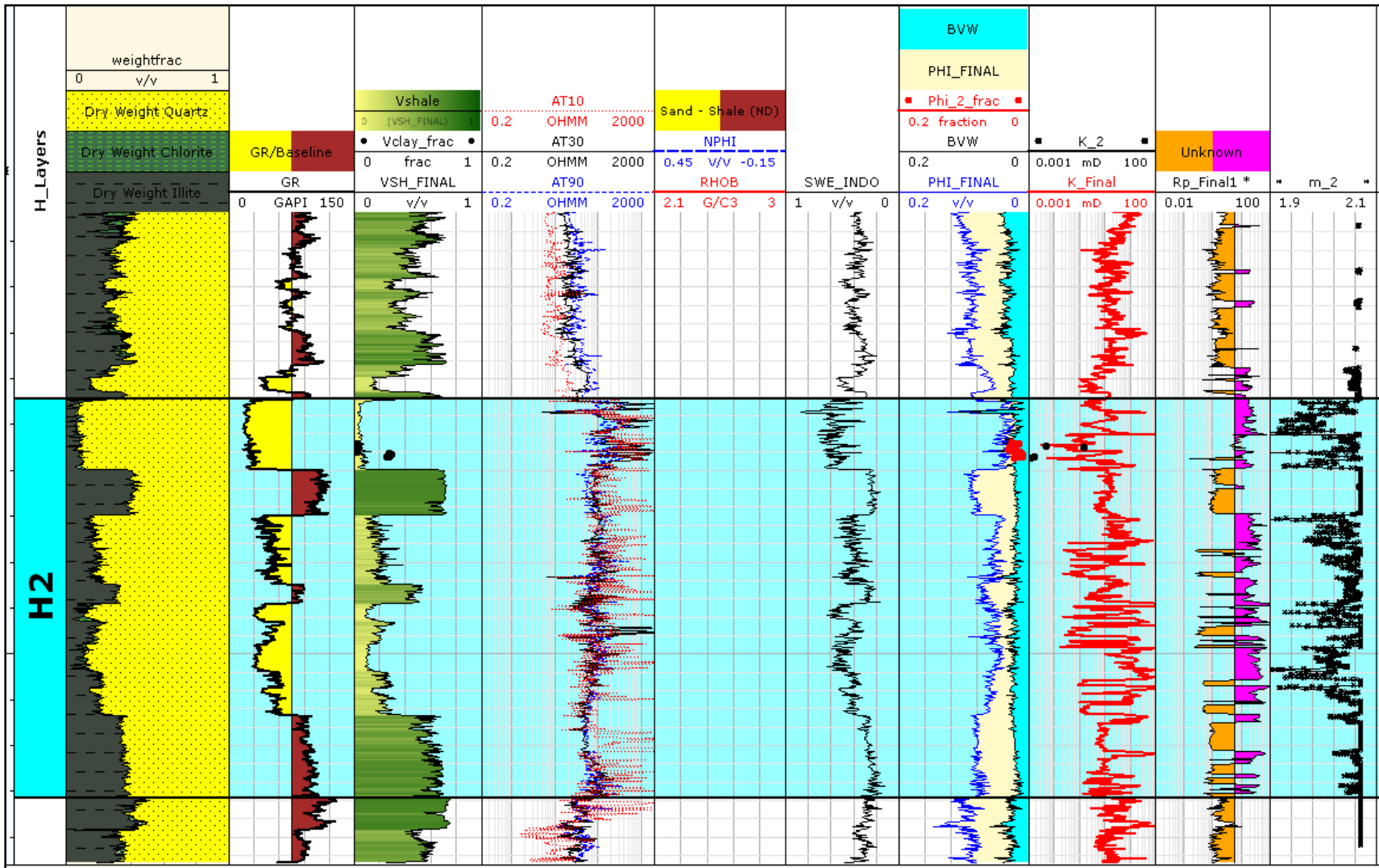


Figure D-3: Well 3 Log plot to summarize log derived petrophysical properties. Track 1: Lithology Track 2: Gamma ray, API Track 3: Volume of shale, fraction Track 4: Resistivity, Ohmm Track 5: Neutron-density Track 6: Water saturation, fraction Track 7: Porosity-water saturation Track 8: Permeability, mD Track 9: Pore throat radius, microns Track 10: Cementation exponent, unitless. Dots show available core data in the porosity and permeability tracks.

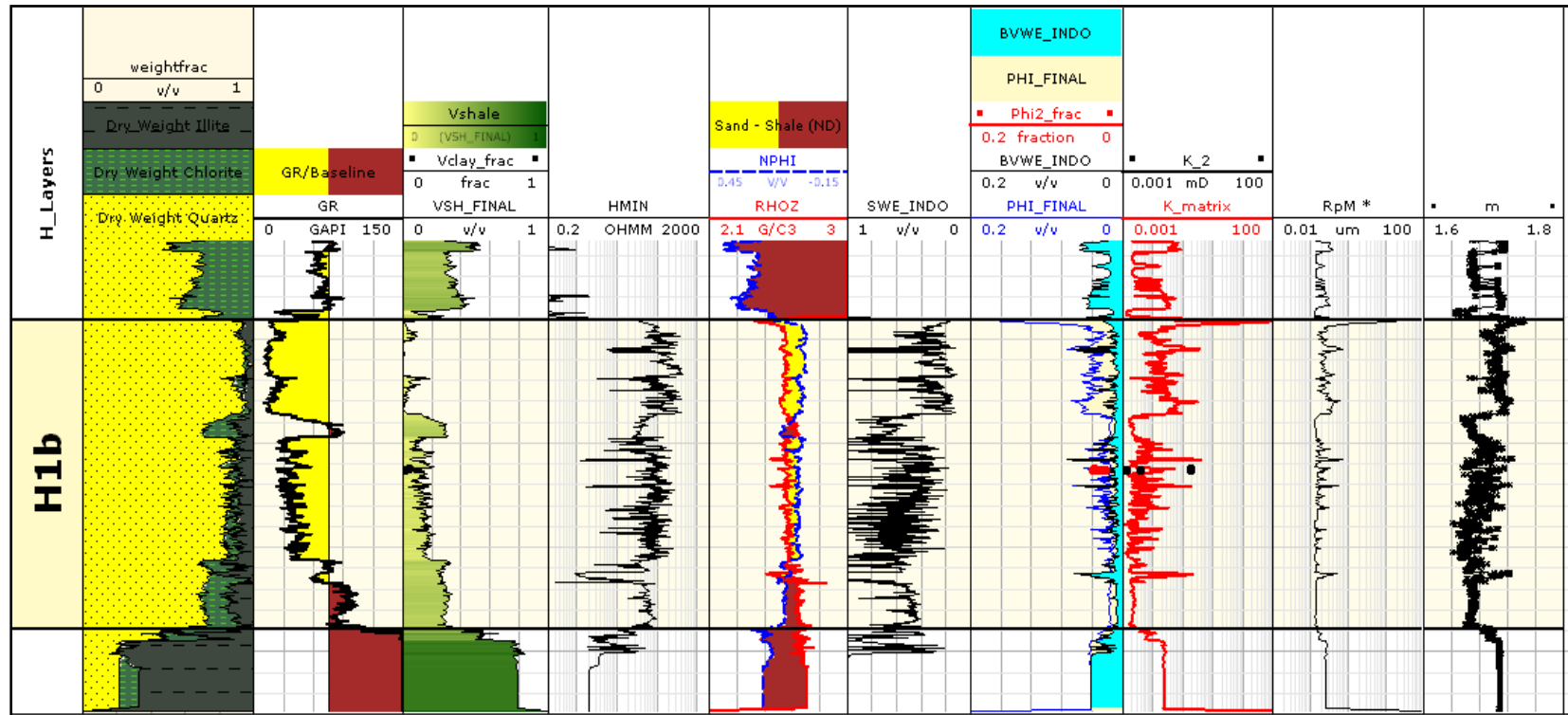


Figure D-4: Well 4ST Log plot to summarize log derived petrophysical properties. Track 1: Lithology Track 2: Gamma ray, API Track 3: Volume of shale, fraction Track 4: Resistivity, Ohmm Track 5: Neutron-density Track 6: Water saturation, fraction Track 7: Porosity-water saturation Track 8: Permeability, mD Track 9: Pore throat radius, microns Track 10: Cementation exponent, unitless. Dots show available core data in the porosity and permeability tracks.

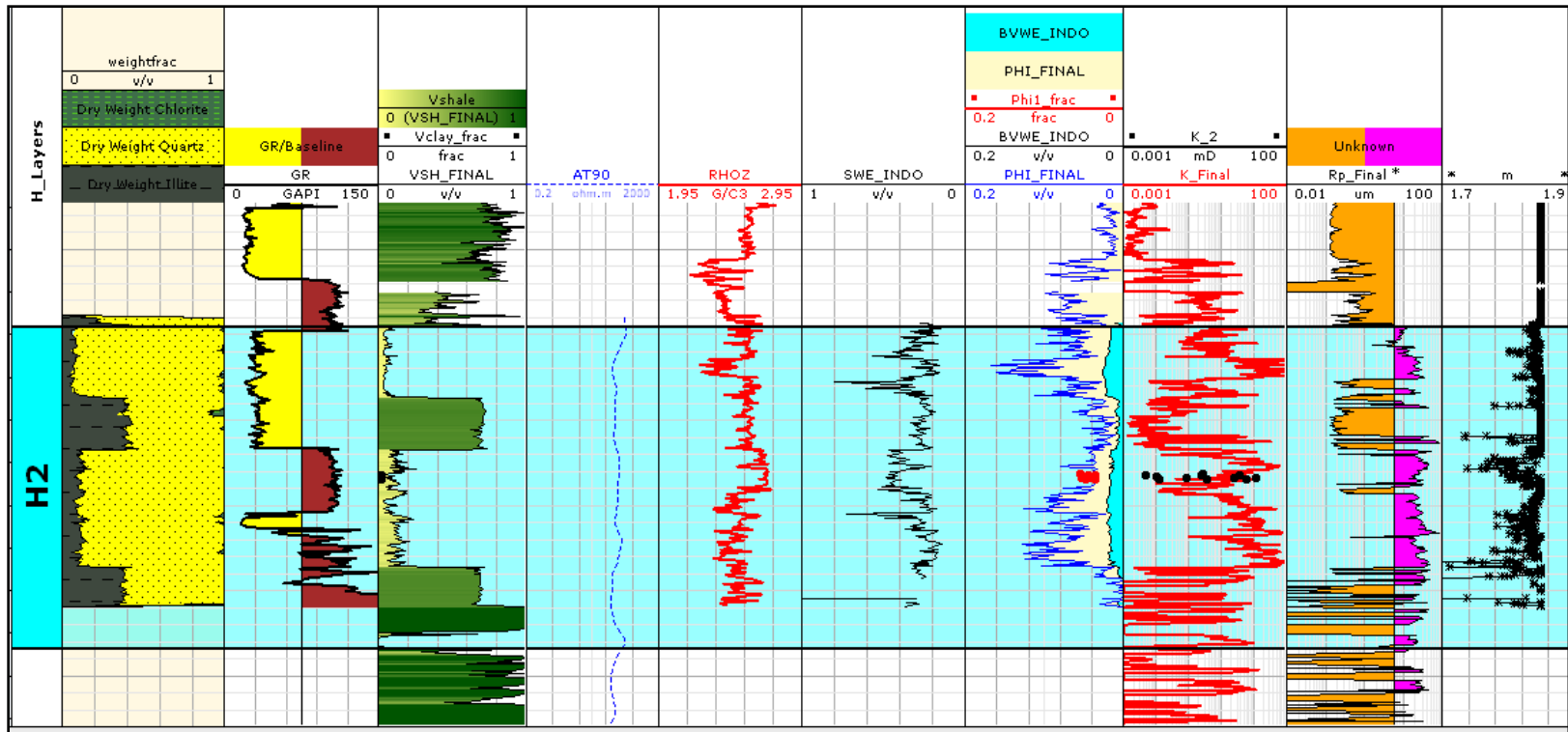


Figure D-5: Well 5 Log plot to summarize log derived petrophysical properties. Track 1: Lithology Track 2: Gamma ray, API Track 3: Volume of shale, fraction Track 4: Resistivity, Ohmm Track 5: Neutron-density Track 6: Water saturation, fraction Track 7: Porosity-water saturation Track 8: Permeability, mD Track 9: Pore throat radius, microns Track 10: Cementation exponent, unitless. Dots show available core data in the porosity and permeability tracks.

APPENDIX E

PORE SCALE SIMULATION WORKFLOW

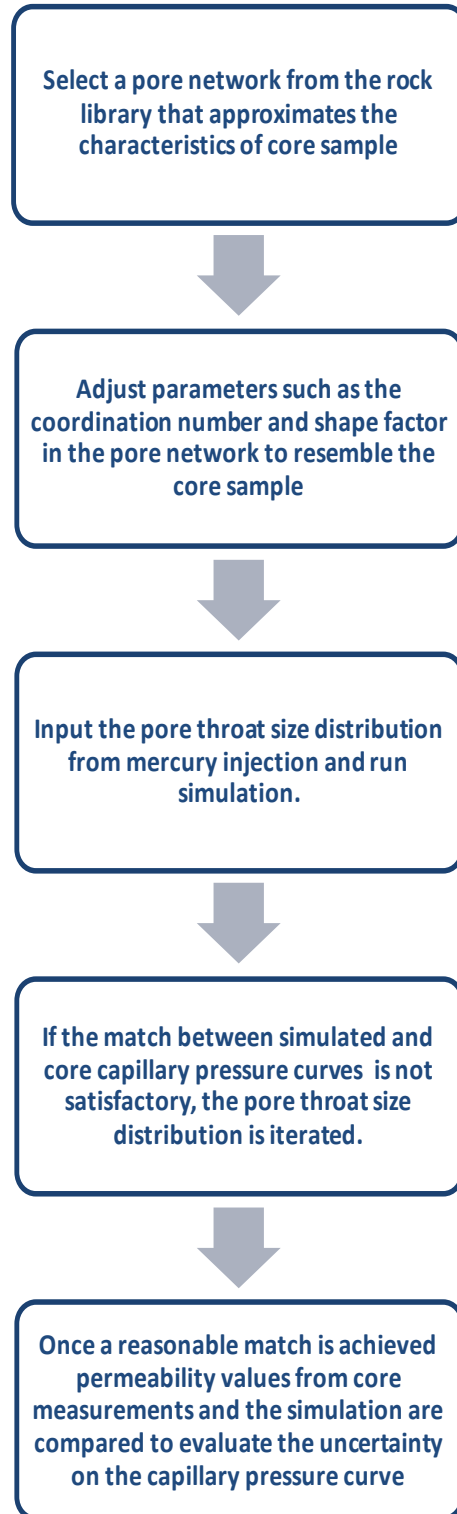


Figure E-1: Pore scale simulation workflow summarizing the steps taken in the evaluation

APPENDIX F

SATURATION HEIGHT FUNCTION WORKFLOW

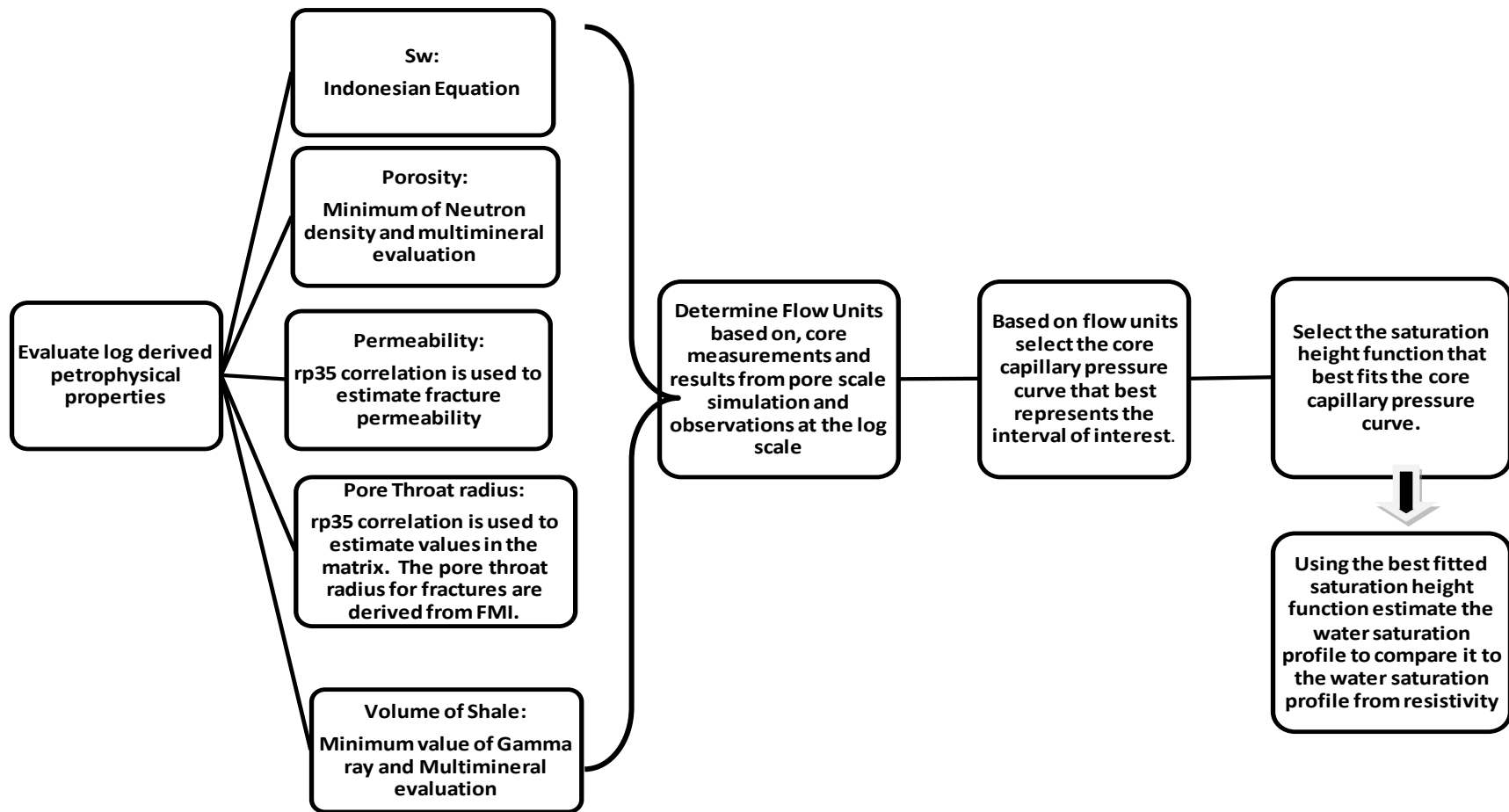


Figure F-1: Saturation height function workflow summarizing the steps taken in the evaluation.